

ABSTRACT

Title of dissertation: NONLINEAR WAVE CHAOS AND
 THE RANDOM COUPLING MODEL

Min Zhou

Dissertation directed by: Professor Steven M. Anlage
 Department of Electrical and Computer Engineering

Concepts from the field of wave chaos have been shown to successfully predict the statistical properties of linear electromagnetic fields in electrically large enclosures. The Random Coupling Model (RCM) describes these properties by incorporating both universal features described by Random Matrix Theory and the system-specific features of particular system realizations. This Ph.D. thesis studies various approaches to extend the RCM to the nonlinear domain. Nonlinearity has been introduced to study the statistics of generated harmonics and amplitude dependent responses of complex electromagnetic structures. The sources of nonlinearity that have been studied include circuit elements such as diodes, nonlinear dielectrics, and superconducting materials. Nonlinear systems in different scenarios are studied and the RCM is applied and extended to explain the statistical results. This is an important step in the ongoing effort to create the science of nonlinear wave chaos.

NONLINEAR WAVE CHAOS
AND THE RANDOM COUPLING MODEL

by

Min Zhou

Dissertation submitted to the Faculty of the Graduate School of the
University of Maryland, College Park in partial fulfillment
of the requirements for the degree of
Doctor of Philosophy
2019

Advisory Committee:

Professor Steven M. Anlage, Chair/Advisor

Professor Thomas M. Antonsen, Jr, Dean's Representative

Professor Thomas E. Murphy

Professor Phillip Sprangle

Professor Christopher Davis

© Copyright by
Min Zhou
2019

Acknowledgments

To finish the Ph.D. study is a big challenge to me. I get the sense of achievement when I am finally able to accomplish it. I get reshaped by many good people I met during my Ph.D. life. Along the way, my advisor Prof. Steven Anlage is the person I would thank the most. I feel very lucky to be able to join his group and receive his close guidance. He is always full of good ideas, hard-working, optimistic and cheering people up. To express my appreciation in words is out of my language skills. I believe in the future I can tell, I will always recall what I have learned here to approach problems and collaborate with people.

I would also express my deeply appreciation to my co-advisors Prof. Thomas M. Antonsen, Jr. and Prof. Edward Ott who are always caring about my progress and giving me advice. Prof. Thomas M. Antonsen is so smart that he can quickly point out the right direction when I am in the bottleneck of my problem, while it may take me several months to prove he is right. I remember Prof. Antonsen is always open for discussions, humorous and also sometimes good at being serious to give students some pressure.

I also thank to other faculty members in my advisory committee, Professor Thomas E. Murphy, Professor Phillip Sprangle and Professor Christopher Davis, who are very busy but still spend time reading my thesis and give me helpful advice.

The helpful and entertaining environment in the group makes our research efficient and fun. I thank to the people who create this atmosphere, including Jen-Hao Yeh, Daimeng Zhang, Ziyuan Fu, Bo Xiao, Bakhrom Oripov, Seokjin Bae, Shukai

Ma, Cougar Garcia, Jingnan Cai, Lei Chen. And people in the wave chaos group including Trystan Koch, Bisrat Addissie, Ke Ma, Farasatul Adnan, Ben Frazier, Tornike Ghutishvili, Mohammad Rahaman.

There are many other people kindly offered help to my work. Shaomao Xu, Yubing Zhou from Prof. Liangbing Hu's group in MSE collaborate with us on the Corbino experiment. Kuang Qin and Prof. Jarek Wosik from University of Houston collaborate with us on the water heating experiment. Many people from our neighbor Prof. Johnpierre Paglione's group and CNAM, Sheng Ran, I-Lin Liu, Chris Eckberg, Halyna Hodovanets, to name a few, and many of my friends in Physics and ECE departments are not named here. I should remember their help, too.

In addition, my parents and other family members always support me. Though they won't read and understand my work here, I thank to them to be always there no matter what I am.

Lastly, I thank to our funding sources to provide the financial support to my research. The AFOSR under COE Grant No. FA9550-15-1-0171, the ONR under Grant No. N000141512134, the COST Action IC1407 ACCREDIT supported by COST (the European Cooperation in Science and Technology), and the Maryland Center for Nanophysics and Advanced Materials (CNAM).

Table of Contents

Acknowledgements	ii
List of Tables	vii
List of Figures	viii
1 Introduction to Wave Chaos	1
1.1 From Classical Chaos to Wave Chaos	1
1.2 Statistical Approaches	4
1.3 The Random Coupling Model in Linear Systems	7
1.4 Extending to Nonlinear Systems and Outline of the Thesis	10
2 Statistics of Second Harmonic Fields	15
2.1 Experimental Setup	15
2.2 Model	18
2.3 Results	20
2.4 Comparison with other models	24
2.4.1 Rayleigh distribution of electric fields	25
2.4.2 Combined Rayleigh distribution of second harmonic fields	27
2.4.3 Double Weibull distribution of second harmonic fields	28
2.5 Conclusions	30
3 Diode Loaded Bowtie Microwave Billiard	32
3.1 Bowtie with a Nonlinear Port	33
3.2 Results	37
3.2.1 Diode-Loaded Port Radiation Impedance	37
3.2.2 Short Orbits	38
3.2.3 Ensemble Realizations	41
3.2.4 Radiation Efficiency of the Nonlinear Port (High Loss System)	42
3.2.5 Simulation in CST	46
3.3 Discussion and Future Work	50
3.3.1 Nonlinear Port with a Diode	50
3.3.2 Diode Located in the Billiard	52

3.4	Conclusions	56
4	Superconducting Cut-Circle Microwave Billiards	57
4.1	Nonlinear Impedance of the Lead Coated Superconducting Cut-Circle Microwave Billiard	57
4.1.1	Experimental Setup	58
4.1.2	Noise Effects and Low Loss Limit	65
4.1.3	Further Discussion	72
4.1.4	Conclusion	75
4.2	TiN on Si Wafer Cut-Circle Microwave Billiard	77
4.2.1	Simulations of the TiN Cut-circle Billiard In CST	78
4.2.1.1	Eigen Modes of the TiN Cut-circle Billiard	79
4.2.1.2	Perturbation	82
4.2.2	Preliminary Results on the TiN Cut-circle Billiard	89
4.2.3	Future Work	93
5	Corbino Reflection Technique to Measure Material Microwave Properties	96
5.1	Experiment Setup	96
5.2	Derivation of R_F , T_F , A_F	98
5.3	Results	104
5.3.1	Ideal measurements for good metal	106
5.3.2	Measured Al foil	108
5.4	Future work	111
6	Conclusions and Future Work	113
6.1	Conclusions	113
6.2	Future Work	115
A	Procedure for RCM Data Analysis	117
A.1	Gather ensemble data for the cavity scattering parameter \bar{S}_{cav}	117
A.2	Calculate the ensemble-averaged impedance \bar{Z}_{avg}	119
A.3	Extract the fluctuating normalized impedance $\bar{\xi}$ from the data	121
A.4	Lowest Usable Frequency (LUF) of the RCM	123
A.5	Determine the Loss Parameter α by fitting the statistics of $\bar{\xi}$	124
A.6	Some reasons why RCM statistics may NOT be seen in experimental data	127
A.7	Weyl's formula	128
A.8	Short Orbit Correction	128
A.9	Determine Z_{rad} using the Time Gating Method (TGM)	130
A.10	RCM for ports with highly localized loss	131
B	Nonlinear Simulation	132
B.1	Nonlinear Materials in CST	132
B.2	Diode Simulation in CST	138
B.3	Incorporating a SPICE model in CST	139

B.4	X-parameters	142
C	VNA High Power Option	149
C.1	Overview	149
C.2	Configuration	151
C.3	Making High Power Measurements	153
C.4	Noise Analysis	156
	Bibliography	158

List of Tables

5.1	Preliminary Examination on Wentao's Samples	104
5.2	Preliminary Examination on Geng's Samples	105
5.3	Preliminary Examination on Yubing's Samples	105
6.1	Summary of various kinds of nonlinearity studied	114
C.1	Operating power levels of different components of the PNA, operating for 12 dB high power attenuator and 16 dB RCVR attenuator. Typical power levels are shown for 3.2-20 GHz. All in dBm units.	153

List of Figures

1.1	(a) Sketch of the water drops from a faucet. (b) Sketch of the forced, damped, pendulum. [1]	2
1.2	(a) Regular ray trajectories in a rectangular billiard. (b) Chaotic ray trajectories in a bowtie billiard.	3
2.1	Experimental setup: 1/4-bowtie cavity with an active nonlinear circuit	16
2.2	(a) FOM measures the absolute power, $1f$ response is similar to the S-parameters; (b) FOM measurement of the 2nd harmonics, mainly in 6 – 12 GHz.	17
2.3	(a) Characterize the nonlinear circuit in FOM; (b) $P_{out,2f}$ vs. $P_{in,1f}$ at $f = 3.5, 4.0$ and 4.5 GHz, respectively. Linear fit to $P_{out,2f}$ vs. $P_{in,1f}$ at $f = 3.5$ GHz gives $slope = 2.00 \pm 0.01$	19
2.4	Model of the nonlinear billiard in terms of cascaded cavities	20
2.5	Measurement of second harmonic power statistics and test of the model of cascaded cavities	22
2.6	Best Rayleigh fit (red) by varying the scale parameter σ to the linear induced voltage in the load impedance between ports 1 and 3	26
2.7	RCM-based “simulation” prediction (red) and Combined Rayleigh (green) fit to the second harmonic electric field between port 1 and 2 in high loss and low loss cases	28
2.8	Double Weibull and RCM based simulation fit to the mean normalized induced 2nd harmonic voltage statistics between port 1 and 2 in low loss and high loss cases	30

3.1	Top view of the experiment setup of the 1/4-bowtie quasi-2D microwave billiard loaded with a diode attached to the single port. The diode (Infineon BAS7004) is connected between the center pin of the port and the top plate. The antenna pin is 7.6 mm long, 1.27 mm in diameter. The diode package has dimension $1.3 \times 2.9 \times 1$ mm ³ . The Vector Network Analyzer (Keysight N5242A PNA-X) measures the scattering parameter at excitation levels up to +43 dBm with microwave wavelengths from 3 to 7.5 cm. The two blue solid circles are metallic perturbers that can be moved around to create ensemble realizations. The inset shows a side-view cross section through the diode-loaded antenna.	36
3.2	(a) Schematic illustration of the perimeter of bowtie covered with microwave absorbers to facilitate measurements of the radiation impedance with walls A, B, C and D labeled. (b) Measured $ S_{rad} $ in the radiation case at different input powers, compared to the case of the antenna with no diode.	38
3.3	(a) S_A measurement results as a function of frequency due to one short orbit between the port and wall "A" shown in the inset. The short orbit creates systematic variations in the S-parameters. The periodicity is related to the distance between the port and the exposed wall. The inset shows the experimental configuration for measuring the short orbit. The microwave absorbers are removed from wall A only, creating a single short orbit between the port and wall A. (b) Comparing short orbit corrections to impedance, $Re(z_{cor,A})$ from the experimental results for low power (+5 dBm, blue) and high power (+30 dBm, green) cases, with theoretical calculation (red), which assumes a linear response.	40
3.4	(a) Comparing the reflection S-parameter $ S $ of a typical single realization of the 1/4-bow-tie cavity with diode-loaded port for low power (blue, -5 dBm) and high power (green +30 dBm). (b) Histogram of normalized $Re(\xi)$ obtained from ensemble data using traditional linear RCM for a 1 GHz window centered at 7 GHz. The resulting fitted loss parameter α increases with power as shown in the inset. R^2 values in the legend indicate the goodness of fit [2].	41
3.5	(a) Fitted radiation efficiency η (from $Im(\xi)$ statistics) vs. frequency and power. Each fit was done with data from 120 realizations and a window of 1 GHz. (b) Plot of diode admittance magnitude vs. frequency at various rf powers, as well as the radiation admittance of the linear port $ Y_{no\ diode}^{rad} $	44
3.6	(a) Model in CST to simulate the radiation S-parameters of the non-linear port. The physical dimension and dielectric properties of the diode package are included in the CST model. Note that the parallel plate waveguide is terminated with radiating boundary conditions on all sides. (b) The complete SPICE model of the diode and the package, indicated as 'pack2d_v5' in (a).	47

3.7	(a) Experimental results of the radiation S-parameters at different input powers. (b) Simulation in CST by importing the SPICE model of the diode and package, and adding a dielectric block representing the physical dimension of the package. $ S_{Rad} $ for different amplitudes with diode and no diode case.	48
3.8	Model in CST to simulate the radiation efficiency with the nonlinear port. Four faces are defined along the perimeter of the parallel plate structure, and the port is labelled ‘2’. The total power radiated through the boundary can be calculated by integrating the power density along each face, and summing them up along these 4 faces.	49
3.9	(a) Experimental radiation efficiency obtained by fitting the statistics of ξ . (b) Radiation efficiency simulated in CST, by directly calculating the ratio of $P_{rad}/(P_{tot} - P_{ref})$	50
3.10	Model of the bowtie billiard (a) and diode (b) in CST	53
3.11	Simulated S_{21} for different input amplitudes of the diode-loaded 1/4-bowtie (a) 2-16 GHz range; (b) Zoomed-in view of several modes near 7.9 GHz shows that nonlinearity starts to appear for $\text{amp} > 0.1$	53
3.12	Plots of S-parameters vs. frequency in the diode loaded 1/4-bowtie. (a) $S_{12} \neq S_{21}$ for high amplitude, $\text{amp} = 12$; (b) S_{avg} over 90 realizations for $\text{amp} = 0.1$ and $\text{amp}=12$	54
3.13	(a) Fitted loss parameter α from $Re(\xi_{11})$, using a 1 GHz window for different input amplitudes, the higher amplitude excitation signal results in larger fitted loss parameter; (b) The histograms of normalized impedance $Re(\xi_{11})$ at $f_c = 7$ GHz shows clear differences between the $\text{amp} = 0.1$ and $\text{amp} = 12$ cases, resulting in different fitted loss parameter.	55
4.1	(a) From [3], dimension of Pb coated cut-circle cavity with a Teflon perturber. The height of the cavity is $h = 0.8$ cm. Area $A = 0.0409$ m ² . (b) $ S_{21} $ of the Pb cut-circle cavity at T=5.7 K for different input powers.	59
4.2	Picture of the Pb cut-circle hung on the mixing chamber plate in the BlueFors XLD400 dilution refrigerator.	60
4.3	Temperature vs. time, blue line (left axis) is the temperature change on the 4 K plate, the spikes indicate when the motor is powered to rotate the perturber in the cavity; the black line is the temperature on the Pb cavity (right axis), a typical measurement sweeps from high power (35 dBm) to low power (-5 dBm) and takes around 15 minutes.	62
4.4	(a) Comparing $ S_{21} $ for different output power levels (-5, 5, 15, 25, 35) dBm, measured with high power network analyzer configuration with the superconducting Pb cavity at 800 mK. The signal-to-noise (SNR) for low power measurement is clearly reduced. (b) $ S_{21} $ for different input powers (-10, 0, 10) dBm, measured with a network analyzer in the standard configuration.	63

4.5	(a) Correlation coefficient $\rho(S_{12}^{(1)}, S_{12}^{(k)})$ for realizations of the superconducting Pb cavity at 800 mK measured with low power network analyzer (-10, 0 10) dBm, where k is the number of realizations; (b) Averaged quality factor Q at $T=800$ mK decreases with increasing input power.	64
4.6	$Re(\xi_{12})$ statistics of the superconducting Pb cavity at 800 mK in the 12~13 GHz range for different input powers, including both high power and standard configurations. The fitted α and goodness of fit R^2 are also given in the legend. The inset shows the fitted loss parameter α vs. the input power, for the high power and low power configurations, respectively.	66
4.7	(a) Adding white Gaussian noise to measured S_{21} vs. frequency data with different snr . The snr values are 40 dB and 30 dB. (b) Statistics of $Re(\xi_{12})$ in 12~13 GHz and fitted loss parameter α as a result of adding noise.	68
4.8	$Im(\xi_{22})$ statistics for the 12~13 GHz range of the superconducting Pb cavity at 800 mK for different input powers, including both high power and standard configurations. α is the fitted loss parameter and R^2 is the goodness of fit. The inset shows the fitted loss parameter α vs. the input power, for the high power and low power configurations, respectively.	69
4.9	RCM predicted $Im(\xi_{11})$ statistics for low loss parameters $\alpha \leq 0.1$. Distributions are plotted in linear scale (a) and log scale (b), and compared with the Lorentzian analytical expression which is expected in the $\alpha = 0$ limit.	70
4.10	(a) Experimental statistics of $Im(\xi_{11})$ of the superconducting Pb cavity at 800 mK for the 14~15 GHz range for different input powers, plotted in log scale. (b) A best fit to the tail of $Im(\xi_{11})$ at $P_{in} = 35$ dBm showing the loss parameter α is on the order of 10^{-3}	71
4.11	A simulation of 120 realizations starting with S_{avg} and different loss parameters. Then RCM is applied to get: (a) Statistics of $Re(\xi_{11})$. (b) Statistics of $Im(\xi_{11})$	73
4.12	(a) A CST model of the cut-circle billiard. The loss parameter of the billiard can be tuned by changing the conductivity of the metal walls. (b) The fitted loss parameter from $Re(\xi_{12})$ statistics compared with that from $Im(\xi_{12})$ statistics.	74
4.13	Dimensions of the proposed billiard. (a) Top view: the Si wafer has a diameter of $D=200$ mm. A straight cut of 50 mm wide is made from the edge. (b) Cross-sectional view (not to scale): TiN is coated on both top and bottom of the Si wafer. The thickness of the Si wafer is $h=0.725$ mm. The thickness of the TiN has not been decided yet and needs further discussion.	78

4.14	(a) 3D model of the TiN on Si cut-circle billiard with two antenna ports to couple signals in/out of the resonator. (b) A detailed view of how the antenna couples to the billiard. (c) Simulated S-parameters of the configuration with antenna to cut-circle edge distance $d = 1$ mm and antenna center pin length $h = 7$ mm.	80
4.15	(a) A detailed view of the S-parameters near 5.9 GHz, search S_{21} peaks as the eigen frequencies, excluding wiggles caused by finite time truncation of the signal. (b) Field distribution for the 495 th eigen mode at frequency 7.026 GHz	80
4.16	(a) The mode frequencies found from S_{21} peaks, compared with the first 500 eigenmodes solved for the closed Si wafer cut-circle. (b) Eigen mode frequencies fit to Weyl formula.	81
4.17	(a) Schematic illustration of a laser perturbation on the PEC film with a spot radius of 2 mm. The effect of the laser heating is modeled as changing the reactance of the spot region. (b) Simulated S-parameters as the result of the reactance change. An Ohmic sheet impedance of $Z = R + i * X$ (Ω/sq) is assumed for the spot. The X values are listed in the legend.	85
4.18	Mechanical perturbation (a) cross-section view of the displacement created by a pressure of 0.2 MPa on a circular area of diameter $D = 1$ cm, at the (1,1) inch position from the circular center. The displacement view has been magnified by a factor of 10 to see the deformation. The legend shows the actual displacement. (b) Displacement overview of the deformed wafer.	86
4.19	(a) Top view of the experiment setup, the Cu plate is made to support different sizes of Si wafer. (b) Back view, a screw made of Teflon or other plastic material is used for mechanical perturbation. (c) Detailed view of the setup, the quartz block is used for mechanical support and thermal conduction. The Teflon block in the SMA connector is used to provide electrical isolation between the wafer and the connector as well as mechanical support to the wafer.	89
4.20	Experimental setup in pulsed tube fridge. A test sample of Nb on 3-in Si wafer is used.	90
4.21	(a) Microwave absorbers are covered over the SMA launch connectors. Microwave absorbers are also attached to the copper plate below the wafer. (b) Interior of the can is also covered with microwave absorbers. (c) S_{12} measured at room temperature with microwave absorbers used in (a) and (b).	91
4.22	Plots of transmission amplitude $ S_{12} $ vs. frequency. (a) $ S_{12} $ at different temperatures shows Nb is superconducting at $T = 6.1$ K. (b) $ S_{12} $ of the Nb two-side coated Si wafer for different input powers at $T = 6.1$ K mainly shows nonlinear resistivity of the Nb.	92
5.1	Schematic sketch of the Cobino measurement setup. The coaxial cable inner radius is $a = 0.254$ mm; the outer radius $b = 0.84$ mm.	97

5.2	Table 2.1 from ref. [4], note that we have used κ instead of k for the extinction coefficient.	102
5.3	Table G.1 from ref. [4].	103
5.4	Expected measured quantities for a copper film with thickness $t=0.45$ mm $\gg \delta$. (a) S-parameter; (b) Effective impedance Z_S^{eff} ; (c) Complex conductivity σ ; (d) Complex dielectric constant ε ; (e) Complex refractive index $N = n + i\kappa$; (f) α, β, ϕ_r	107
5.5	Expected measured quantities for a copper film with thickness $t=0.45$ mm $\gg \delta$. (g) R_F, T_F, A_F ; (h) skin depth δ , bulk reflectivity R ; (i) compare shielding effectiveness $SE = \log(T)$ with Simon's formula Eq. 5.20; (j) $ kt_0 \gg 1$, the substrate effect can be neglected.	108
5.6	Measured quantities for a Al foil with thickness $t=0.015$ mm $< \delta$. (a) S-parameter; (b) Effective impedance Z_S^{eff} ; (c) Complex conductivity σ ; (d) Complex dielectric constant ε ; (e) Complex refractive index $N = n + i\kappa$; (f) α, β, ϕ_r	110
5.7	Measured quantities for a Al foil with thickness $t=0.015$ mm $< \delta$. (g) R_F, T_F, A_F ; (h) skin depth δ , bulk reflectivity R ; (i) compare shielding effectiveness $SE = \log(T)$ with Simon's formula Eq. 5.20; (j) Compare $ kt_0 $ vs. 1, $ kt_0 \ll 1$, so the substrate effect needs to be considered.	111
A.1	(a) One-port measurements of 1/4-bowtie billiard with two cylindrical perturbers (the two blue solid circles). (b) Typical results for S_{cav} Single realization of the bowtie billiard with perturbers (blue). S_{avg} Average over 120 realizations (red). S_{rad} Radiation S-parameters where the billiard boundaries are covered with microwave absorbers, and no perturbers are present (yellow).	118
A.2	For a two port bowtie experiment, with 91 realizations. (a) Correlation coefficient $\rho(S_{11}^{(1)}, S_{11}^{(k)})$ and $\rho(S_{11}^{(k)}, S_{11}^{(k+1)})$. (b) Correlation coefficient $\rho(S_{12}^{(1)}, S_{12}^{(k)})$ and $\rho(S_{12}^{(k)}, S_{12}^{(k+1)})$. The correlation coefficient of S_{12} is much smaller compared with that of S_{11}	119
A.3	Results shown in Fig. A.1(b) presented in the impedance domain. \bar{Z}_{cav} - Single realization of the bowtie billiard with perturbers (blue). \bar{Z}_{avg} - Average over 120 realizations (red). \bar{Z}_{rad} - Radiation impedance where the billiard boundaries are covered with microwave absorbers, and no perturbers are present (yellow).	121
A.4	Line fit $\log(abs(FFT(S_{11})))$ to estimate the average quality factor $Q = -\omega_0/(2*slope)$, where ω_0 if the center frequency of the frequency band utilized	122

A.5	(a) Experimentally obtained $Re(\xi_{11})$ statistics from one-port bowtie measurement, over 120 realizations in the frequency range 14.5 - 15 GHz. The best fit PDF ($R^2 = 0.9985$) gives $\alpha=2.1$. For the $Re(\xi_{11})$ statistics, one finds that $\langle Re(\xi_{11}) \rangle = 1$. (b) $Im(\xi_{11})$ statistics obtained in a similar way. The best fit PDF gives $\alpha=2.0$, which is almost the same as the fitting from the $Re(\xi_{11})$. Its PDF has a mean of $\langle Im(\xi_{11}) \rangle = 0$	125
A.6	Random Matrix Theory predictions for the PDF of normalized impedance for various loss parameters α in a time-reversal symmetric system, i.e. GOE (Gaussian Orthogonal Ensemble) statistics. (a) $Re(\xi_{11})$ statistics; (b) $Im(\xi_{11})$ statistics.	126
A.7	(a) The consistency of fitted α from $Re(\xi)_{11}$ and $Im(\xi)_{11}$ experimental PDFs. (b) The variance of $Re(\xi)_{11}$ and $Im(\xi)_{11}$ PDFs are predicted to be $a/\pi\alpha$ for $\alpha \gg 1$	126
B.1	The CST model where the bowtie billiard is filled with a 3^{rd} nonlinear dielectric material $\vec{D}(\vec{r}, t) = \epsilon_0\epsilon_L\vec{E}(\vec{r}, t) + \epsilon_0\chi^{(3)}\vec{E}(\vec{r}, t)^3$. The two yellow circles are perturbers.	135
B.2	For the filled material with a nonlinear Kerr model, where $\chi_\infty^{(3)} = 10^{-9}$ [m/V] ² , $\chi_S^{(3)} = 10^{-8}$ [m/V] ² , and $\tau = 10^{-9}$. (a) Input Gaussian signal in the frequency range 4-7 GHz at port 1 in the time domain; inset shows the Fourier Transform of the signal in the frequency domain. (b) Fourier Transform of the output signal at port 1 shows there is 3^{rd} harmonic response.	135
B.3	For the filled material with a nonlinear 3^{rd} order model, where $\chi^{(3)}(\vec{B}) = 0.001$ [m/A] ² . (a) $ S_{11} $ for different $\chi^{(3)}(\vec{E})$ in the frequency range of 2-16 GHz. (b) Detailed view of the nonlinear response at several resonances.	136
B.4	For the filled material with a nonlinear 3^{rd} order model, where $\chi^{(3)}(\vec{B}) = 0.001$ [m/A] ² , $\chi^{(3)}(\vec{E}) = 0$ [m/V] ² . (a) $ S_{11} $ for different input amplitudes in the frequency range of 2-16 GHz. (b) Detail view of the nonlinear response at several resonances.	137
B.5	Built-in diode model in CST lumped network element.	139
B.6	Procedures to add a SPICE circuit with a 3D model. 1. Add a discrete port in 3D window; 2. Set the ports to be differential ports; 3. Set external port and connect with the imported SPICE circuit.	140
B.7	Set up a transient task with different amplitude excitation signals.	141
B.8	Spectral analysis of nonlinear components, from [5].	144
B.9	Procedures to measure the X-parameters, from [5].	144
B.10	Experimental setup at UNM for measuring the X-parameters of the 2^{nd} harmonics circuit.	145
B.11	Simulation circuit in ADS. The "XNP1" is the measured X-parameters file of the 2^{rd} harmonics circuit.	146

B.12	ADS simulation with measured circuit X-parameters. (a) Power sweep at 4 GHz, spectral analysis from the 1 st to the 4 th order harmonics. Upper: Power magnitude of the harmonics, the green line is a straight line with slope of 2; Lower: Phases of the harmonics. (b) Frequency sweep for input power -10 dBm. Spectral analysis from the 1 st to the 4 th order harmonics. Upper: Power magnitude; Lower: Phases.	147
C.1	2-port two way high power configuration, Fig. 7 in ref. [6]. Damage power levels and external components are labelled.	150
C.2	Experimental setup of the high power 2-port two-way measurement	155
C.3	Comparing $ S_{21} $ for different output power levels, the signal-to-noise (SNR) for low power measurement is small. The DUT is a Pb-coated cut-circle microwave cavity in a dilution refrigerator at T=740 mK where there is around 20 dB around-trip attenuation along the transmission lines.	156

Chapter 1: Introduction to Wave Chaos

1.1 From Classical Chaos to Wave Chaos

In classical chaos, a system is defined to be chaotic when its motion is settled neither into steady nor periodic nor quasi-periodic motion. For example, the experiment of Shaw (1984) where time intervals between water drops from a faucet are recorded (see Fig .1.1(a)). When the water inflow rate of the faucet is sufficiently small, the time intervals between successive drops $\Delta t_n = t_{n+1} - t_n$ are all equal. As the inflow rate is increased, Δt_n will be periodic. And as the inflow rate is further increased, the period of Δt_n will be increase. At sufficiently large inflow rate, Δt_n losses regularity and it is argued to be chaotic. Another example of chaotic dynamics occurs for the forced damped pendulum in a gravitational field (see Fig. 1.1(b)). The motion of the angle θ is described by the equation:

$$\frac{d^2\theta}{dt^2} + v\frac{d\theta}{dt} + \sin\theta = T\sin(2\pi ft) \quad (1.1)$$

where v represents the friction coefficient at the pivot, T and f represents the magnitude and frequency of the applied torque. It has been shown that for some choices of those system parameters v , T and f , chaotic behavior can be displayed in this system.

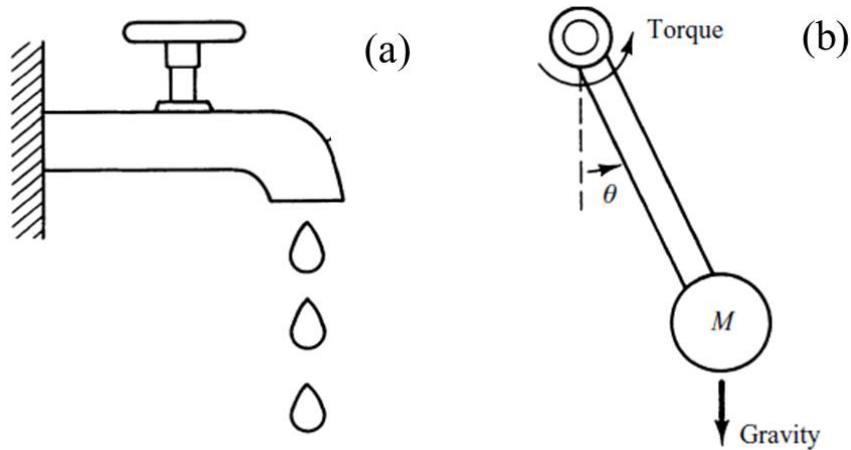


Figure 1.1: (a) Sketch of the water drops from a faucet. (b) Sketch of the forced, damped, pendulum. [1]

In general, we can not use standard analytical functions to describe the chaotic orbits. They appear to be very complex, irregular and difficult to predict. Chaotic systems are very sensitive to the initial conditions and details of the system, as well as noise. A typical feature of chaotic orbits is that a slight difference in the initial distance Δ_0 will grow exponentially with time $\Delta_t \sim \Delta_0 \exp(ht)$ [1], where $h > 0$ is called the Lyapunov exponent. To illustrate this concept, we can consider a particle moving in a 2D billiard having elastic scattering with the walls, with a slight difference in initial conditions. If the billiard has a regular shape as shown in Fig. 1.2(a), then after a certain amount of time, the ray trajectories will diverge slowly, maybe linearly or polynomially with time. While if the billiard has a chaotic shape such as a 1/4 bowtie billiard shown in Fig. 1.2(b), then the difference between the ray trajectories will exponentially grow with time.

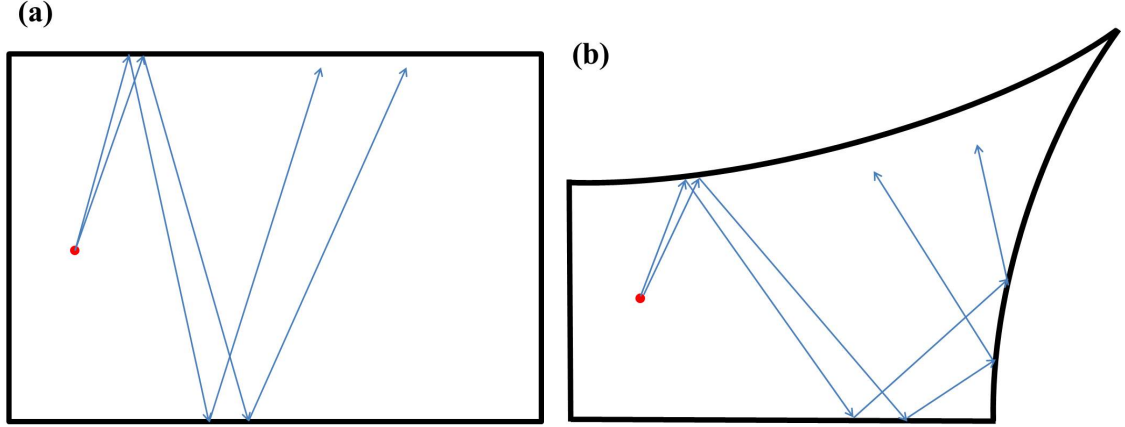


Figure 1.2: (a) Regular ray trajectories in a rectangular billiard. (b) Chaotic ray trajectories in a bowtie billiard.

In Hamiltonian mechanics, a particle with position \vec{r} and momentum \vec{p} is subject to Hamilton's equations of motion with the Hamiltonian:

$$H = \frac{\vec{p} \cdot \vec{p}}{2m} + V(\vec{r}) \quad (1.2)$$

where m is the mass of the particle and V represents the potential. The motion is constrained by the boundary conditions, which can be regular (Fig. 1.2(a)), chaotic (Fig. 1.2(b)) or a mix of these two.

For electromagnetic waves $\vec{E} = E_0 e^{-i(\vec{k} \cdot \vec{r} - \omega t)}$, they are subject to the wave equation:

$$\frac{1}{c^2} \frac{\partial^2}{\partial t^2} \vec{E} = \nabla^2 \vec{E}, \quad (1.3)$$

$$\left(\frac{\omega^2}{c^2} + k^2\right) \vec{E} = 0, \quad (1.4)$$

the equation is also constrained by the boundary conditions. In the case when the wavelength is much smaller than the characteristic length of the billiard, the wave properties will be very sensitive to the details of the system. A small change in the

system may result in a very different solution to the wave equation. Furthermore, it is computationally expensive to solve this wave equation in this situation. Instead, in the field of “wave chaos”, the small wavelength limit is called the “ray limit” or “semi-classical limit”. The waves in the billiards can be approximated as the ray trajectories of a classical object. Thus when we refer to a wave chaotic system, we mean a wave scattering system with a chaotic-shaped boundary.

1.2 Statistical Approaches

The scattering of short-wavelength waves in domains in which the corresponding rays are chaotic (known as wave chaos) has inspired research activities in many diverse contexts including quantum dots [7,8], atomic nuclei [9], optical cavities [10], microwave cavities [11–13], acoustic resonators [14,15], and others. In this case the response is extremely sensitive to the domain’s configuration, the driving frequency, and ambient conditions such as temperature and pressure [16]. Numerical solution of the detailed response of a particular system is computationally intensive and does not necessarily provide much insight to other systems which are slightly different. This leads to the adoption of a statistical description.

It is hypothesized that the wave properties of classically chaotic billiard systems show universal statistical properties described by Random Matrix Theory (RMT) [17–19]. The statistics depend only on general symmetries, including the presence or absence of time-reversal invariance and spin-1/2 degree of freedom, and on the degree of loss. In the field of “wave chaos”, Random Matrix The-

ory (RMT) has been shown to successfully describe many statistical properties of bounded wave-chaotic systems (e.g., enclosures such as electromagnetic cavities), including their eigenvalue spectra, eigenfunctions, scattering matrices, delay times, etc. [19–26]. Wave systems also have system-specific features that modify the underlying universal fluctuations. The Random Coupling Model (RCM) accounts for those non-universal features such as the details of ports coupling waves into and out of the domain of the cavity, short orbits that exist between the ports, and specific persistent features of the enclosure in an ensemble of similar but different realizations of a system [27–29]. Experimentally, the system-specific features are captured by the impedance (reaction matrix) [30] averaged over an ensemble of realizations. By applying this technique to remove non-universal properties, RMT statistical properties have been uncovered in experimental data on ray chaotic 1D quantum graphs [31], 2D electromagnetic cavities (known as billiards) [32] and 3D cavities (e.g. reverberation chambers) [33].

The 1/4 bowtie 2D billiard shown in Fig. 1.2(b) is typical ray chaotic system that we have used for a long time to study the properties of chaotic systems. [20, 26, 34–36]. RCM has been verified in this system through a series of works examining the statistical properties of scattering systems [28, 29, 32, 37]. RCM is shown to have applications in studying statistics of induced voltages or electromagnetic fields inside complicated enclosures and subjected to high frequency radiation [33, 38], or the problems of EMI/EMC in reverberation chambers [39]. The RCM approach can also be applied in the wireless communication field [40], to study time dependent variation in transmitted signal strength through a complex environment [41–43]. In

other areas such as studying coupling between enclosures [44], properties of acoustic systems [45], etc, we can also find useful applications of RCM.

Based on the success of the RCM, it is of interest to explore directions extending its generality. Along this line, theories have been developed for “mixed” systems which include both regular and chaotic ray dynamics [46], for networks of coupled cavities in which waves propagate from one sub-system to another [44, 47], and for modifications of scattering statistics due to losses localized in the ports, rather than in the scattering system [48–50]. While such previous extensions have focused on linear systems, it is of great interest to see how nonlinearity would modify the RCM.

Nonlinearity in wave-chaotic systems has been studied in several aspects. For example, rogue waves can appear in linear wave chaotic scattering systems [51, 52]. However, such waves can also appear in a variety of physical contexts and are enhanced by nonlinear mechanisms [53, 54]. In acoustics, Time-Reversed Nonlinear Elastic Wave Spectroscopy (TR/NEWS) is based on the nonlinear time reversal properties of a wave chaotic system [55]. TR/NEWS is proposed as a tool to detect micro-scale damage features (e.g., delaminations, micro-cracks or weak adhesive bonds) via their nonlinear acoustic signatures [56, 57]. Applying this idea to electromagnetic waves [58], the nonlinear electromagnetic time-reversal mirror shows promise for novel applications such as exclusive communication and wireless power transfer [59–62]. Theoretical study of stationary scattering from quantum graphs has been generalized to the nonlinear domain, where the nonlinearity creates multistability and hysteresis [63]. A wave-chaotic microwave cavity with a nonlinear circuit feedback loop demonstrated sub-wavelength position sensing for a perturber

inside the cavity [64]. Nonlinearity is a key ingredient in various machine learning protocols, including neural networks [65, 66] and reservoir computing [67, 68]. Utilizing wave chaotic layers, along with nonlinearity, offers an attractive way to enable physical realizations of deep learning machines [69–71].

Linear wave chaotic systems have certain universal properties, while nonlinear systems lose the property of linear superposition. This Ph.D. research studies whether or not there are universal statistical properties in nonlinear wave chaotic systems. Applying the RCM analysis to various nonlinear wave chaotic systems, we ask the question: if and how can the RCM be modified for such systems? Note that our approach is to empirically investigate various nonlinear wave chaotic systems to establish benchmark experimental results and to challenge the theory to explain those results.

1.3 The Random Coupling Model in Linear Systems

In the case of a linear ray-chaotic cavity with N ports, the Random Coupling Model characterizes the fluctuations in the impedance $\overline{\overline{Z}}$ and scattering $\overline{\overline{S}}$ matrices. The scattering and impedance matrices are related by a simple bilinear transformation [37]:

$$\overline{\overline{S}} = \overline{\overline{Z}}_0^{-1/2} (\overline{\overline{Z}} + \overline{\overline{Z}}_0)^{-1} (\overline{\overline{Z}} - \overline{\overline{Z}}_0) \overline{\overline{Z}}_0^{-1/2} \quad (1.5)$$

where $\overline{\overline{Z}}_0$ is a real diagonal matrix whose elements are the characteristic impedances of the waveguide (or transmission line) input channels at the driving ports. The statistical properties of the cavity impedance $\overline{\overline{Z}}_{cav}$ are described by a universally

fluctuating impedance $\bar{\bar{\xi}}$ that is ‘dressed’ by system-specific properties captured by the ensemble average impedance $\bar{\bar{Z}}_{avg}$ as:

$$\bar{\bar{Z}}_{cav} = i \cdot \text{Im}(\bar{\bar{Z}}_{avg}) + [\text{Re}(\bar{\bar{Z}}_{avg})]^{\frac{1}{2}} \cdot \bar{\bar{\xi}} \cdot [\text{Re}(\bar{\bar{Z}}_{avg})]^{\frac{1}{2}} \quad (1.6)$$

where $\bar{\bar{Z}}_{avg}$ is an average of impedance over an ensemble of cavity realizations and (or) frequencies. $\bar{\bar{Z}}_{avg}$ contains the system specific features including the radiation impedance of the ports and short orbits that survive the ensemble averages [27–29]. The “radiation impedance” represents the impedance measured at the ports of the scattering enclosure in the case that the waves are allowed to enter the enclosure through the port but not return, as if they were absorbed in the enclosure or radiated to infinity. Experimentally, it can be measured with the empty bowtie billiard whose boundary is covered with perfect microwave absorbers. A “short orbit” is a ray trajectory that leaves a port and soon returns to it, or another port, instead of ergodically sampling the system. It is the result of the port-port interaction that introduces deterministic field components which can remain fixed throughout the ensemble [29]. $\bar{\bar{Z}}_{avg}$ can also be estimated if the radiation impedance of the ports and the cavity shape are known [27].

By inverting Eq. (1.6) and subtracting the non-universal features from $\bar{\bar{Z}}_{cav}$ in each realization, one can uncover a statistically fluctuating quantity that should correspond to $\bar{\bar{\xi}}$. It has been hypothesized that all sufficiently complex wave chaotic systems have universal impedance fluctuations described by Random Matrix Theory (RMT) [17–19]. According to the theory, for a two port system [72, 73],

$$\xi_{rmt,a,b} = \frac{-i}{\pi} \sum_{m=1}^M \frac{W_{am}W_{bm}}{\lambda_m^{rmt} - i\alpha} \quad (1.7)$$

The element $\xi_{rmt,a,b}$ is the impedance between port a and port b, and the sum is over the M eigenmodes of the closed wave scattering enclosure, W_{am} (or W_{bm}) represents the coupling between the port a (or the port b) and the m^{th} eigenmode. Based on the assumption of the random plane wave hypothesis (the Berry hypothesis), for a wave-chaotic cavity enclosure filled with reciprocal media (i.e. that has time-reversal invariance), W_{am} and W_{bm} are independent Gaussian random real variables of zero mean and unit variance. [72]. λ_m^{rmt} is the m^{th} eigenvalue of a large random matrix. The statistics of these eigenvalues are based on RMT, and they are found from a large random matrix selected from the GOE (Gaussian Orthogonal Ensemble) for the time-reversal-invariant case. The details of generating λ_m^{rmt} are discussed in Appendix A of Ref. [38].

The loss parameter α is the only parameter determining the statistics of the universal fluctuations. In the case of a two-dimensional billiard the loss parameter is given by $\alpha = k^2 A / (4\pi Q)$ and can be interpreted as the ratio of the typical 3-dB bandwidth of the resonant modes to the mean spacing in frequency between the modes. $k = 2\pi f / c$ is the wave number of frequency f , A represents the area of the billiard, and Q is the typical loaded quality factor of the enclosure under the assumption that losses are uniform. The loss mainly comes from the propagation losses in the upper and lower plates. Fig. A.6 shows the distribution of ξ_{rmt} of a one-port system for different α .

The algorithm for generating $\bar{\bar{\xi}}_{rmt}$ can be developed based on Eq. (1.7). By varying α , the universal statistics of $\bar{\bar{\xi}}$ for systems with varying losses can be numerically generated, and examples of these distributions are given in Ref. [38]. Starting

with a statistical ensemble data set and going the other way around, one can fit the experimentally extracted $\overline{\xi}$ to $\overline{\xi}_{rmt}(\alpha)$, and the best matching distributions will give an estimate of the loss parameter of the experimental system. Note that when examining data, for a two port system, $\overline{\xi}$ can produce 8 histograms, i.e. real and imaginary part for each element $\xi_{a,b}$. However due to the reciprocity of the system, $\xi_{12} = \xi_{21}$, and ξ_{11} has the same statistics as ξ_{22} according to Eq. (1.7). As a result there are 4 unique histograms that are simultaneously fit using a single loss parameter α . Experimental tests in various wave chaotic systems have systematically explored the effects of different loss parameters on the statistical properties of impedance, ranging from cryogenic superconducting cavities ($\alpha \sim 0.01$) [3, 74] to three-dimensional complex enclosures ($\alpha > 10$) [33].

To apply the RCM experimentally, one generally first generates an ensemble of realizations of the chaotic system, getting an ensemble of \overline{Z}_{cav} . Then $\overline{\xi}_{exp}$ can be extracted. By fitting the statistics of $\overline{\xi}_{exp}$ to RMT generated $\overline{\xi}_{rmt}$, the loss parameter α of the system can be estimated. An example together with other RCM analysis is given in Appendix A.

1.4 Extending to Nonlinear Systems and Outline of the Thesis

There are several approaches to create nonlinear wave chaotic systems and apply the RCM. For the nonlinear objects that can be introduced into the system in the microwave regime, one could utilize circuit elements like diodes or BJTs, or nonlinear dielectric or magnetic materials, or materials in the superconducting

state. While nonlinear effects from passive elements in the microwave frequencies are generally weak to observe, we have tried various approaches to enlarge the nonlinear effects. Nonlinear properties include harmonic generation, amplitude dependent responses, etc. Our approach is to empirically find interesting nonlinear effects and then go back to see if we could extend the RCM to explain the results. This thesis will present the efforts we have explored to create different nonlinear responses and use RCM approach to explain them.

The generated harmonics are a natural result of the nonlinear responses. To have measurable harmonic signals, an active 2^{nd} harmonic generation circuit is attached to the 1/4 bowtie billiard. The Vector Network Analyzer (VNA) in the Frequency Offset Mode (FOM) is able to measure the absolute amplitude of the 2^{nd} harmonic signals. By moving the perturbers around, an ensemble of realizations of this nonlinear system is generated, and the statistics of the 2^{nd} harmonic signals can be gathered. By carefully characterizing the nonlinear circuit, we are able to create a model of the resulting 2^{nd} harmonic statistics based on the Random Coupling Model. The predicted statistics of the second harmonic fields agree quite well with the experimental results [2]. Chapter 2 will present the details of the study on harmonic statistics.

Another direction is to introduce nonlinearity and see the nonlinear effects on the linear response properties such as the S-parameters. Considering our experiment is mainly conducted in 2D microwave billiards, we have tried to use diodes and superconducting billiards, both of which are passive nonlinear sources. To observe a strong nonlinear signal requires high amplitude signals to drive them into the

nonlinear domain. We therefore upgraded our VNA with a high power option. With the appropriate external components, it is able to measure the 2-port calibrated S-parameters with powers up to ~ 37 dBm.

Chapter 3 presents the results of introducing diodes into the 1/4 bowtie billiard. The initial proposal is to create a nonlinear environment where the diodes are randomly distributed in the billiard. Since the signal decays substantially as it propagates away from the excitation port, nonlinear responses were hardly observed even with more than 30 diodes in the billiard. Thus, in the experiment a diode is directly attached at the port to create a nonlinear port. This dramatically changes the radiation impedance as well as the statistics of the raw normalized impedance. The short orbits behavior also deviates from the RCM-based prediction. It turns out that the port behaves like a nonlinear and lossy port. The recently developed radiation efficiency model is adopted to describe the port. We also found that a simulation in CST reproduces the key features observed in experiment [75]. For the configuration where the diode is far away from the port in the billiard, some results of CST simulations indicate a trend of changes in the impedance statistics.

The study of superconducting microwave billiards are presented in Chapter 4. Superconducting materials show a nonlinear surface impedance $Z = R + iX$ below T_c . We start with a Pb coated copper microwave billiard that we have studied before. It has been measured in the superconducting state at temperature $T \sim 6$ K. Applying RCM to the data, the fit α was found on the order of 0.01 [3]. Using the VNA that is capable of measuring in a range of different powers, it is possible to observe the nonlinear responses of this superconducting billiard. However, as shown

in Chapter 4, the Pb billiard mainly shows nonlinear resistance R , i.e. the resonance peak decreases with increased input powers. As a result, the cavity quality factor Q changes with the input power. However since there is only a small change in Q , in the case where α is so small, it is predicted that the change in statistics will be hardly visible. In the experiment we find the changes in statistics are mainly due to the varying noise levels during the measurements.

Complimentary to the Pb billiard, we propose a superconducting billiard that will mainly show nonlinear reactance X [76]. It is expected that the resonance will shift in frequency as the input power changes. Titanium Nitride (TiN) is reported to have a high kinetic inductance and to be nonlinear in a reactive manner. We design an experiment for the TiN on Silicon wafer cut-circle billiard. Two perturbation methods are planned. The up-to-date progress for this experiment are also presented in Chapter 4.

Apart from the work on nonlinear wave chaos, other work during my PhD study is also documented in this dissertation. Chapter 5 documents the use of the Corbino reflection technique to measure thin film or bulk material microwave properties at room temperature. The Corbino technique is a one port measurement of a sample with a circular contact configuration. It was originally developed to characterize superconducting thin film properties [77, 78]. We collaborate with Prof. Liangbing Hu from the Department of Materials Science and Engineering. We want to determine the microwave absorptance, transmittance and reflectance of a range of different materials, from metal-like to dielectric-like. We find that this method is not applicable for dielectric-like materials. The results and future work are addressed.

The conclusion for this dissertation and future work are given in Chapter 6. The appendixes include some notes/manuals developed during my research. Various approaches for RCM analysis of experimental data are summarized in appendix A. Appendix B is a summary of results of nonlinear simulation. Appendix C is a manual for implementing the high power VNA to measure the calibrated S-parameters.

Chapter 2: Statistics of Second Harmonic Fields

Harmonic generation is a natural result of nonlinearity. As our first approach to study nonlinear wave chaotic systems, we tried to add a pure harmonic generator to the bowtie billiard. We analyzed the statistics of the fields in the system. This chapter presents our study of the statistics of the 2^{nd} harmonic fields.

2.1 Experimental Setup

In this experiment, an active nonlinear circuit is added to a ray-chaotic microwave billiard. The billiard, shown schematically in Fig. 2.1, has an area of $A = 0.115 \text{ m}^2$, with corresponding characteristic length of $A^{1/2} = 0.34 \text{ m}$. For the microwave wavelengths used here (3 – 9 cm), the billiard is assumed to be large compared to the wavelength (electrically large enclosure) and is considered to be in the semiclassical or short-wavelength limit. The cavity has a height of $d = 7.9 \text{ mm}$. Thus, below a frequency $f_{max} = c/(2d) = 18.9 \text{ GHz}$, it is a quasi-2D billiard in which the electric field is polarized in the short direction, and the magnetic field is in the 2D plane of the cavity. For frequencies $2f > 7 \text{ GHz}$, the mode number is above ~ 200 and it can be considered that the cavity is in the highly over-moded regime (where there are many cavity modes at and below the frequency of interest) [12].

The cavity has internal loss, giving rise to a finite quality factor (Q) for the resonant modes of the closed system. We shall assume that a single Q describes the losses in a given range of frequency [79]. The nonlinear circuit accepts input at a particular frequency and generates and amplifies second harmonic output which is fed back into the billiard. We study the statistics of the second harmonic fields in the cavity for a fixed power at the input fundamental frequency.

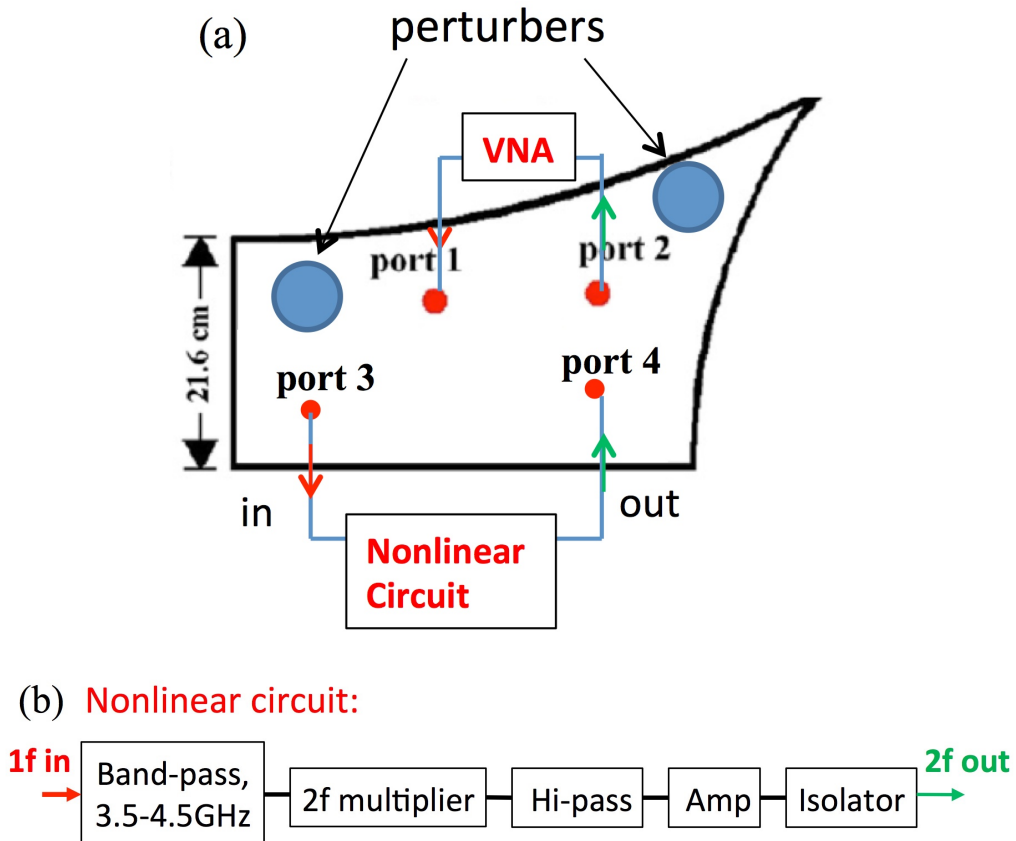


Figure 2.1: Experimental setup: 1/4-bowtie cavity with an active nonlinear circuit. (a) The vector network analyzer (Model: Keysight PNA N5242A or E8364C) measures the absolute power of harmonics at port 2 relative to the input fundamental tone at port 1. (b) The active nonlinear circuit consists of two cascaded 3.5 GHz - 4.5 GHz band pass filters (Mini-Circuit VBFZ-4000-S+), a frequency doubler (Mini-Circuit ZX9C-2-50-S+), two cascaded high pass filters (mini-circuit VHF-6010+), a wide band power amplifier (HP83020A) and an isolator (FairviewMicrowave SFI 0418).

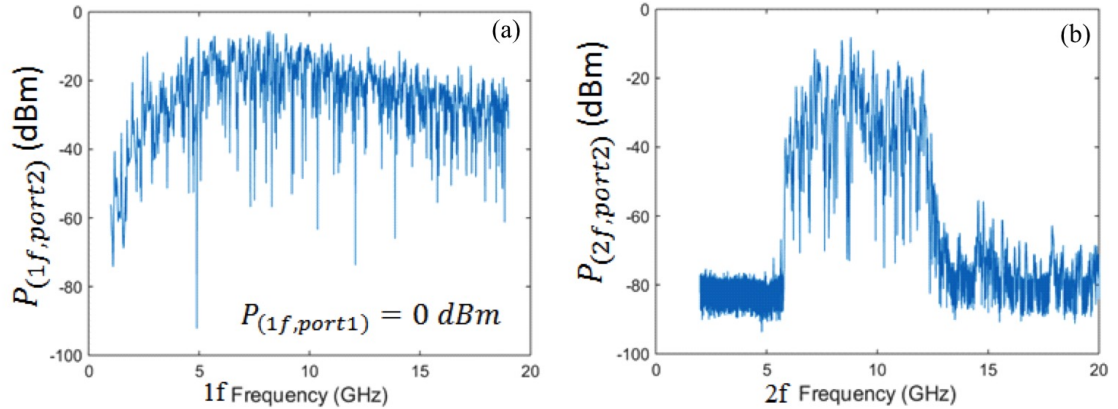


Figure 2.2: (a) FOM measures the absolute power, $1f$ response is similar to the S-parameters; (b) FOM measurement of the 2nd harmonics, mainly in 6 – 12 GHz.

Here a symmetry-reduced “1/4-bowtie” shape (Fig. 2.1) quasi-two-dimensional cavity at room temperature is used as the ray chaotic system [12]. To introduce non-linearity, an active nonlinear circuit is connected to two ports of the billiard as shown in Fig. 2.1. The active nonlinear circuit is designed to double the input frequency in the range from 3.5 GHz to 4.5 GHz; other harmonics, as well as the fundamental tone, are suppressed at the output. Measurements are taken between two additional ports of the cavity, and an ensemble of billiard realizations is created by moving two perturbers throughout the cavity. Thus the realizations maintain a fixed volume and mean mode spacing. A sinusoidal tone at fundamental frequency $1f$ with a certain power is created in the Vector Network Analyzer (VNA) and injected through port 1. Port 3 is the input of the active nonlinear circuit. Due to the ray-chaotic properties of the cavity, the $1f$ signal received by port 3 varies over several decades in power as a function of frequency and perturber locations. The output at port 4 will be at the 2nd harmonic frequency with a certain power. Port 4 serves as the

source of a $2f$ signal injected into the cavity. The VNA is set in Frequency Offset Mode (FOM), which provides the capability to have the VNA sources apply a tone at one frequency and the receivers measure the response at any other frequency. In our case, the VNA port 2 measures the absolute power of the 2nd harmonics of the stimulus from port 1. Fig. 2.2 gives typical results of VNA in FOM measuring $1f$ response (Fig. 2.2(a)) which is like the transmission S-parameters and the 2nd harmonic responses (Fig. 2.2(b)), for a single realization of the positions of the perturbers. The 2nd harmonic signals are mainly in the 6 – 12 GHz range due to the filters used.

2.2 Model

We separately characterize the nonlinear circuit under FOM. As shown in Fig. 2.3, for input powers in the range -45 dBm to -5 dBm, $P_{out,2f}$ vs. $P_{in,1f}$ for several frequencies are plotted in Fig. 2.3(b). A linear fit to $P_{out,2f}$ vs. $P_{in,1f}$ shows that they obey a simple empirical relation:

$$P_{out,2f} = slope \cdot P_{in,1f} + intercept \quad (\text{dBm}) \quad (2.1)$$

where $slope = 2.00 \pm 0.01$ and the amplifier contributes to the “intercept” term. Note that power P is in dBm and the “intercept” here refers to intercept in units of dBm, i.e. $P_{out,2f}$ when $P_{in,1f} = 0$ dBm. In terms of power measured in Watts, since $P_{dBm} = 10 \log(10^3 \times P_W)$, Eq. (2.1) is effectively $P_{out,2f} = P_{in,1f}^2 \cdot P_{norm}$, where $P_{norm} = 10^6 \times P_{intercept}$, and $P_{intercept}$ is *intercept* converted into units of Watts.

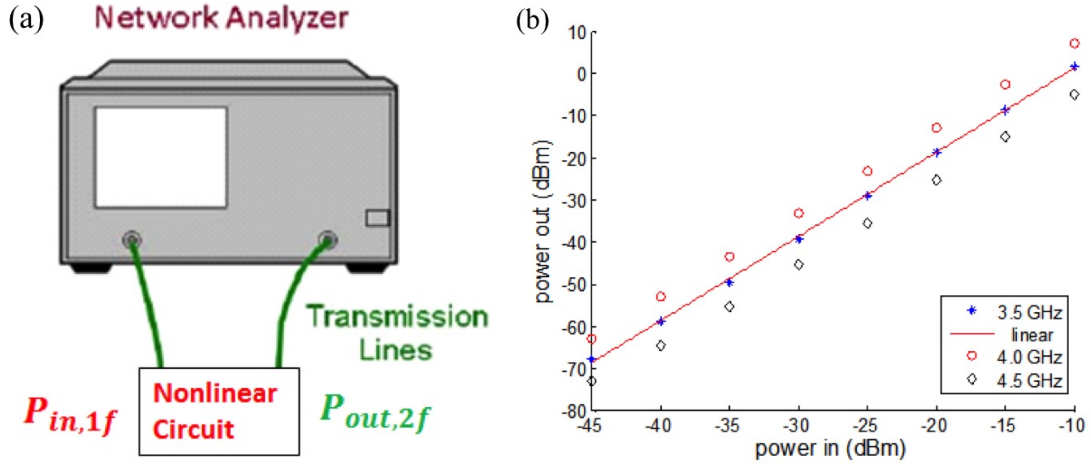


Figure 2.3: (a) Characterize the nonlinear circuit in FOM; (b) $P_{out,2f}$ vs. $P_{in,1f}$ at $f = 3.5, 4.0$ and 4.5 GHz, respectively. Linear fit to $P_{out,2f}$ vs. $P_{in,1f}$ at $f = 3.5$ GHz gives $slope = 2.00 \pm 0.01$.

To describe the statistical properties of the second harmonic signals measured at port 2, a model of two cascaded linear cavities connected through the nonlinear circuit is proposed (see Fig. 2.4). This choice was motivated by earlier work on the statistics of impedance and power fluctuations in chains of wave chaotic cavities connected by weak but linear coupling [44, 47, 79]. As shown in Fig. 2.4, the source signal enters the cavity from port 1. The signal reaching port 3, which is the input of the nonlinear circuit, is given by the linear transmission S-parameters between port 1 and 3, denoted by S_{13} . Its statistics are described by the linear Random Coupling Model at $1f$ with loss parameter α_1 . The output signals of the nonlinear circuit at port 4 are at the 2nd harmonic of the input at port 3. Their relation is characterized by the empirical law of the active nonlinear circuit, Eq. (2.1). Lastly, the 2nd harmonic signals received at port 2 are linearly related to the 2nd harmonic signals introduced at port 4, which is given by the statistical fluctuations of the

transmission S-parameters between port 2 and port 4 denoted by S_{24} . The statistics of S_{24} are described by the linear Random Coupling Model at frequency $2f$ with loss parameter α_2 . Since the vector network analyzer in FOM measures power, we have a simple relation for the power of 2nd harmonics received at port 2,

$$P_{out,2f} = (P_{in,1f} \cdot |S_{13}|^2)^2 \cdot P_{norm} \cdot |S_{24}|^2 \quad (\text{Watts}) \quad (2.2)$$

where $P_{in,1f}$, P_{norm} are deterministic, in units of Watts; and $|S_{13}|^2$, $|S_{24}|^2$ are fluctuating quantities.

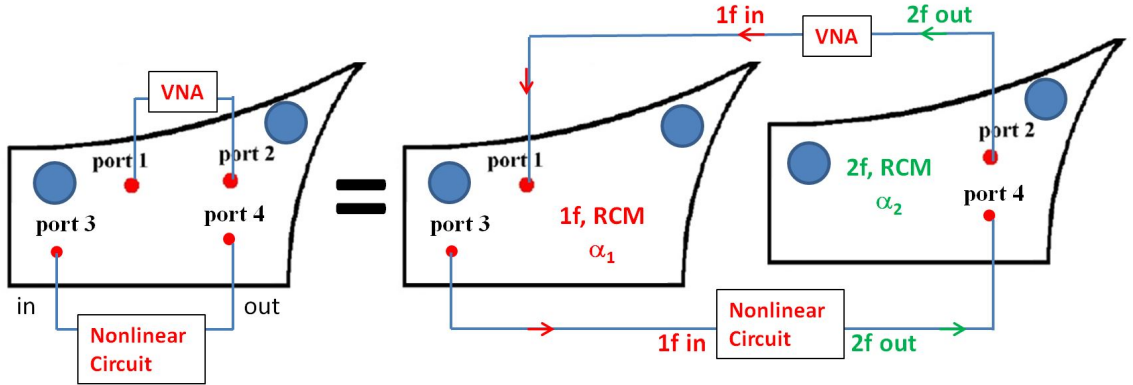


Figure 2.4: Model of the nonlinear billiard in terms of cascaded cavities. The bowtie with an active nonlinear circuit attached can be considered as two linear billiards operating at different frequencies and loss parameters coupled through the nonlinear circuit

2.3 Results

In the results shown below, there are 136 realizations for $P_{in,1f} = -5$ dBm input, 99 for 0 dBm, and 91 for +5 dBm respectively. For each realization, the VNA outputs a $1f$ signal sweeping from 3.5 GHz to 4.5 GHz with fixed power at port 1, which is $P_{in,1f}$. With the FOM one then measures the response 2nd harmonics at

port 2, $P_{out,2f}$. For each $1f$ input power, the histograms of power values of $P_{out,2f}$ are compiled over the ensemble of realizations as well as second harmonic frequency between 7 - 9 GHz. These histograms of measured 2nd harmonic power are plotted in Fig. 2.5 and will be compared with theory predictions.

To test the extended RCM model, we have two approaches. The “measured product” is a calculation based on separate measurement of each linear component, i.e. measurements of S_{13} , S_{24} . S-parameters between ports 1 and 3 are measured at 3.5 - 4.5 GHz, for 120 realizations of the positions of the perturbers. S-parameters between ports 2 and 4 are measured at 7 - 9 GHz, again for 120 different realizations of the perturber positions. In the direct experimental measurement of the $2f$ signal with the $1f$ input, the $1f$ and $2f$ signals pass through the cavity with the same perturber position. However, in the “measured product”, the S-parameters S_{13} and S_{24} are measured independently, each with a separate ensemble of perturber positions. Their values will not correspond directly to those in the case in which the entire transfer function is characterized. Statistically, the histograms for the “measured product” and “experiment” will correspond if S_{13} and S_{24} are effectively independent. By putting the measured quantities into the relation Eq. (2.2), we create 120^2 “realizations” of $P_{out,2f}$. We call this a “super data set” and its P_{2f} statistics can be compared with those measured directly.

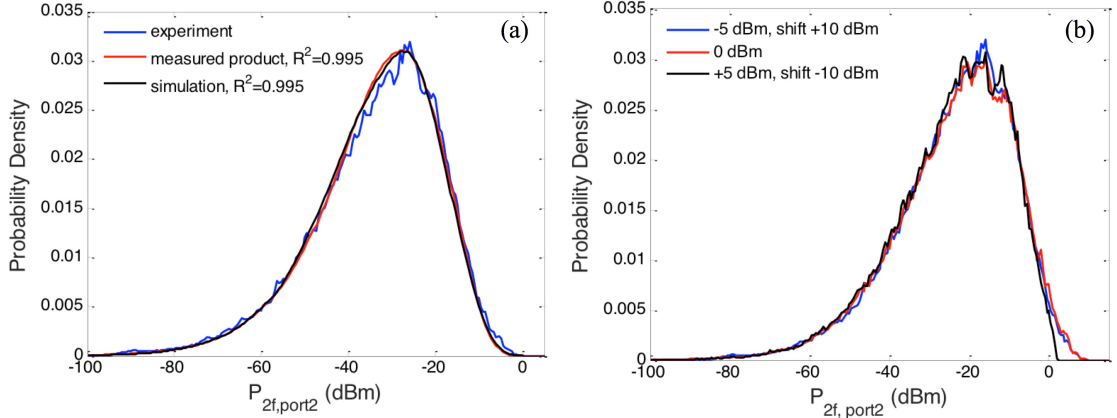


Figure 2.5: Measurement of second harmonic power statistics and test of the model of cascaded cavities. (a) The statistics of the output 2nd harmonic power predicted by the model are compared with direct measurement results (blue). The statistics are compiled over a 2 GHz range with center frequency of 8 GHz. (b) Three input powers are measured: -5 dBm, 0 dBm and +5 dBm, and the distributions are shifted by 10 dBm to overlap. The cutoff near 0 dBm for the +5 dBm curve comes from the saturation of the VNA (Model E8364C). For $P_{in,1f} = -5$ dBm, 0 dBm and 5 dBm, the mean value is -33.6 dBm, -23.6 dBm and -14.3 dBm, respectively. The standard deviations are 14.6 dBm, 14.8 dBm and 14.4 dBm, respectively.

Another approach, termed “simulation”, utilizes the RCM to generate a prediction for the statistical distribution of power values. By using the measured ensembles of $\overline{\overline{S}}_{13}(1f)$ mentioned above, $\overline{\overline{Z}}_{avg,13}(1f)$ can be derived by averaging over realizations. The RCM formulation (Eq. (1.6)) is applied to extract $\overline{\overline{\xi}}(1f)$ from the ensemble data. By fitting the histograms of $\overline{\overline{\xi}}(1f)$, the loss parameter α_1 between 3.5 GHz to 4.5 GHz is estimated. In practice, for each frequency window of 0.5 GHz, the loss parameter α_1 is determined as the average loss parameter obtained from fitting the histograms of the off-diagonal impedance elements $Re\{\overline{\overline{\xi}}_{12}(1f)\}$ and $Im\{\overline{\overline{\xi}}_{12}(1f)\}$. The same procedures are applied to the measured ensembles of $\overline{\overline{S}}_{24}(2f)$ to derive $\overline{\overline{Z}}_{avg,24}(2f)$ and α_2 between 7 GHz and 9 GHz. Having the $\overline{\overline{Z}}_{avg}$ and loss parameters in the two frequency ranges of interest, we can perform Monte Carlo

RMT simulations based on Eq. (1.7) to firstly get normalized impedance $\bar{\xi}$, then to generate ensembles of S_{13} and S_{24} using RCM (Eq. (1.6) and (1.5)). This approach can be considered as a validity test of the RCM. Again, we generate 120 realizations of S_{13} and S_{24} respectively, and substitute them into Eq.(2.2) to create a “super data set” prediction for the histogram of $P_{out,2f}$. The result is based on simulated universal quantities “dressed” by the measured non-universal features.

The loss parameters α at $1f$ and $2f$ are both less than 1. In such a low loss chaotic environment, the individual cavity mode contributions to the S-parameters will be sharp and distinct. The value of $P_{in,1f}$ at port 1 is set so that the majority $1f$ power at port 3 falls within the range where Eq. (2.1) holds. As a result, the power of the second harmonic signal spans a wide range. Figure 2.5 shows histograms of second harmonic power plotted on a log scale with units of dBm. The histogram is compiled from an ensemble of realizations and over a $2f$ output frequency range from 7 to 9 GHz. For a fixed input power over a certain frequency band, the 2nd harmonic output power varies over 8 - 10 decades. For example, Fig. 2.5(a) shows the result for input power $P_{in,1f} = -5$ dBm. The blue curve is the histogram from direct measurement, where the received power of the 2nd harmonics varies from -100 dBm to 0 dBm. It has a mean of -14.3 dBm and standard deviation of 14.4 dBm. The red curve is the “measured product”, also derived from measurement. Although derived by a different approach, the overall statistics agrees very well with our direct measurement of the second harmonic power. The black curve labeled “simulation” is created based on the RCM as described above, and as shown in the

plots, it agrees quite well with the red and blue curves, demonstrating the validity of the Random Coupling Model.

To quantify the agreement, the coefficient of determination R^2 traditionally used in statistics is calculated for each model histogram with respect to the experimental curve. R^2 is always between 0 and 1 and is interpreted as the percentage of variation in the response variable that is explained by the linear model [80]. In general, the higher the R^2 , the better the model fits to the data. The red curve “measured product” has $R^2 = 0.995$ and the black curve “simulation” has $R^2 = 0.994$, both indicating very good agreement. We emphasize that this model yielding this agreement has *no fitting parameter*.

The model (Eq. (2.2)) predicts that changing the input power should simply shift the PDFs of $P_{out,2f}$ by 10 dB for each 5 dB increase in input power. Fig. 2.5(b) shows the shifted curves of experimental results with respect to the 0 dBm case. Indeed the overall distribution has a similar shape for each input power. However, experimentally the VNA reaches its maximum detectable power at nearly 15 dBm. This is why there is a cutoff at high power for the curve of $P_{in,1f} = 5$ dBm.

2.4 Comparison with other models

In the engineering context, the reverberation chamber (RC) has been used to study the statistics of the fields scattered by nonlinear equipment, where it has implications for EMC immunity testing of digital hardware. In [81] second harmonic generation by nonlinear electronics irradiated in a reverberation chamber (RC) has

been investigated. This situation involves a “bare” nonlinear source without filtering or amplification, producing a small nonlinear response with low signal-to-noise ratio. The statistics of the re-radiated harmonic spectrum were investigated by using a model of cascaded random processes. Several models have been developed to analyze the field statistics (Rayleigh distribution) as well as harmonic fields (Combined Rayleigh and Double-Weibull distributions). However, the loss parameter of the RC is generally high (i.e. $\alpha \gg 1$). Hence these models are valid in high loss environments but show deviation in our low loss chaotic billiards, as the results below demonstrate.

2.4.1 Rayleigh distribution of electric fields

We first focus on the statistics of linear fields in the 1/4-bowtie cavity. Ref. [81] assumes that the distribution of the magnitude of the electric field strength $|\mathbf{E}|$ in a reverberation chamber follows a Rayleigh distribution $P_{Ray}(|\mathbf{E}||\sigma)$, where

$$P_{Ray}(x|\sigma) = \frac{x}{\sigma^2} \exp\left(\frac{-x^2}{2\sigma^2}\right) \quad (2.3)$$

and σ is a field scale parameter. To test this model in the 1/4-bowtie cavity, the experiment has been conducted in various loss cases, ranging from a dry ice environment ($T \sim -78^\circ\text{C}$) to reach the low loss regime (loss parameter $\alpha_1 = 0.31$ at $1f$, $\alpha_2 = 0.82$ at $2f$) to a high loss environment (loss parameter $\alpha_1 = 2.9$ at $1f$, $\alpha_2 = 4.6$ at $2f$) by adding microwave absorber segments along the perimeter of the cavity at room temperature. As loss increased, both the mean and standard deviation of field statistics were seen to decrease.

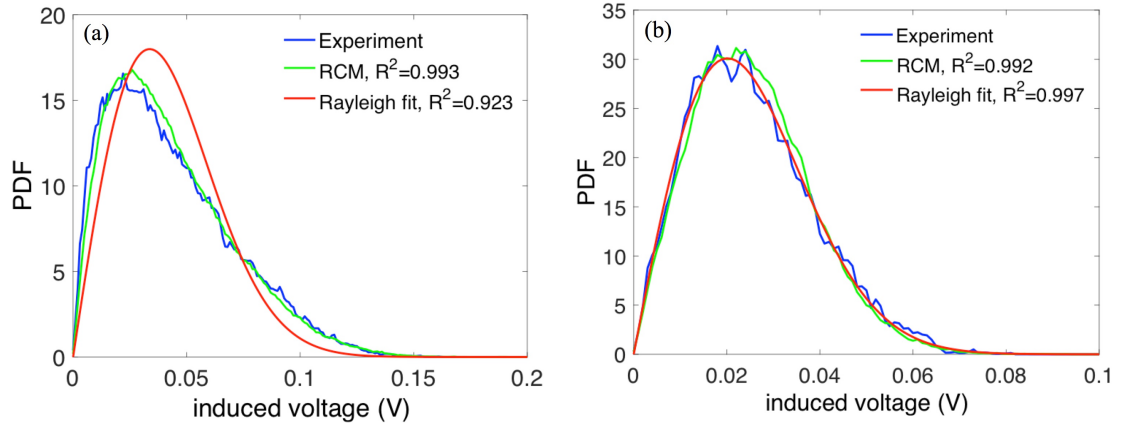


Figure 2.6: Best Rayleigh fit (red) by varying the scale parameter σ to the linear induced voltage in the load impedance between ports 1 and 3. An RCM prediction (green) is shown for comparison. The RCM prediction is generated with known Z_{avg} and loss parameter α_1 , and by applying Eq. (1) in the main text with Monte Carlo simulation. (a) low loss case $\alpha = 0.37, R^2(RCM) = 0.993, R^2(Rayleigh) = 0.923$ with $\sigma = 0.0337$; and (b) high loss case $\alpha = 2.50, R^2(RCM) = 0.992, R^2(Rayleigh) = 0.997$ with $\sigma = 0.0201$. Frequency range 3.5 GHz - 4.5 GHz.

The Rayleigh distribution relies on a scale parameter σ . Fig. 2.6 shows the best Rayleigh fit (red) to the linear field statistics between port 1 and 3 in low loss (Fig. 2.6(a)) case with loss parameter $\alpha = 0.37$ and high loss case (Fig. 2.6(b)) with $\alpha = 2.50$. Here the Rayleigh fit is applied to the induced voltage V at the receiving port since the induced voltage is proportional to the electric field at the port. To calculate the induced voltage V , the power P is converted to voltage by considering a $Z_0 = 50\Omega$ load impedance at the receiving port. As a comparison, the RCM prediction is generated (green). Without additional fitting parameters, the RCM prediction is generated with known Z_{avg} and loss parameter α_1 . Then Eqs. (2) and (3) of the main text are applied by performing Monte Carlo RMT simulation. Fig. 2.6 shows that, as expected [41, 42], the Rayleigh fit deviates from the experiment in

the low loss case and fits well to the high loss case, while the RCM prediction agrees well in both cases. In quantifying the agreement, R^2 for RCM are both larger than 99%, while $R^2 = 0.923$ in low loss and $R^2 = 0.997$ in high loss for the Rayleigh fit.

2.4.2 Combined Rayleigh distribution of second harmonic fields

We now consider the statistics of second harmonics in the case shown in Fig. 2.5. The Combined Rayleigh distribution [81] is firstly based on the assumption that the linear fields obey a Rayleigh distribution. The nonlinear element is modeled as a reradiating source for harmonics, and the generated harmonic signal is related to the incident signal by a power series for weak nonlinearity, i.e. for second harmonic signal, $V_{2f} \propto V_{1f}^2$. The received harmonic signal is therefore the result of a cascaded Rayleigh process. Using standard techniques to determine the overall distribution of combined random process, the probability density functions (PDFs) of the 2nd harmonic fields can be obtained as

$$P_{2nd}(x|\sigma) = \frac{1}{\sqrt{2\sigma}} \int_0^\infty e^{-t^2} e^{-x/(2\sqrt{2}\sigma t)} dt \quad (2.4)$$

The Combined Rayleigh distribution also has the scale parameter σ to vary. Fig. 2.7 shows the best Combined Rayleigh fits to the second harmonic induced voltage. Because the Rayleigh fit fails in the first (linear) process in the low-loss case, as a result the experimental second harmonic statistics deviate from the combined Rayleigh distribution, while both the Rayleigh and Combined Rayleigh models fit well in the high loss case, shown in Fig. 2.7. The singular RCM based “simulation” is generated for comparison. R^2 for this RCM-based simulation are both larger

than 98%, while $R^2 = 0.960$ in low loss and $R^2 = 0.991$ in high loss for Combined Rayleigh fit.

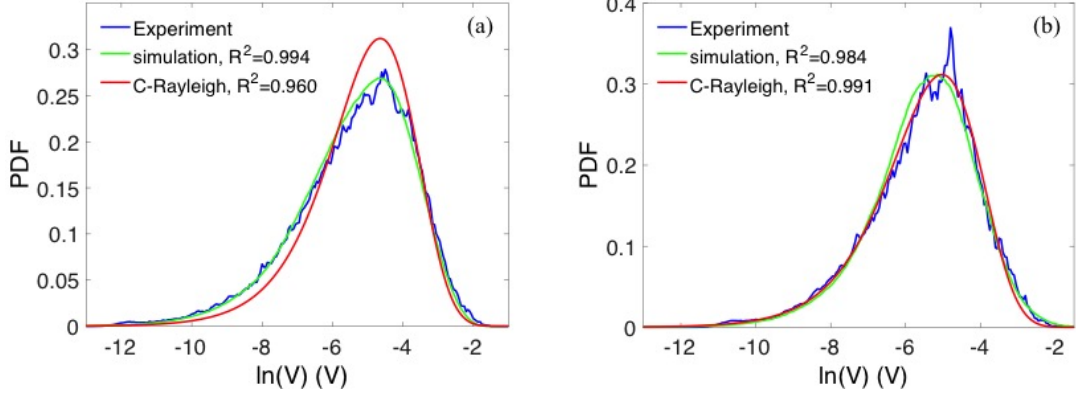


Figure 2.7: RCM-based “simulation” prediction (red) and Combined Rayleigh (green) fit to the second harmonic electric field between port 1 and 2 in: (a) low loss case, $\alpha_1 = 0.30$, $\alpha_2 = 0.78$, $P_{in,1f} = -5$ dBm, $R^2(simulation) = 0.994$, $R^2(C - Rayleigh) = 0.960$ with $\sigma = 0.0047$; and (b) high loss case, $\alpha_1 = 2.85$, $\alpha_2 = 4.56$, $P_{in,1f} = 0$ dBm, $R^2(simulation) = 0.984$, $R^2(C - Rayleigh) = 0.991$ with $\sigma = 0.0032$. Frequency range 7 GHz - 9 GHz.

2.4.3 Double Weibull distribution of second harmonic fields

Later a more versatile statistical model called the Double Weibull distribution was proposed to fit the mean normalized second harmonic electric field \tilde{z} [82], where $\tilde{z} = z/E[z]$ ($E[\cdot]$ is the expectation operator). This model describes the changing statistical harmonics distribution from the Combined Rayleigh distribution due to the nonlinearity strength variation, i.e. the power exponent n ($V_{2f} \propto V_{1f}^n$) of the nonlinear source deviates from 2 as the input amplitude V_{1f} increases [83]. \tilde{z} has a probability density function given by

$$\tilde{f}(\tilde{z}; n) = \frac{\pi\tilde{z}}{n} \Gamma_n^{\frac{2}{n}} \left(1 + \frac{n}{2}\right) \int_0^\infty x^{\frac{2}{n}-3} \exp\left(-x^{\frac{2}{n}} \Gamma_n^{\frac{2}{n}} \left(1 + \frac{n}{2}\right) - \frac{\pi\tilde{z}}{4x^2}\right) dx \quad (2.5)$$

where $\Gamma(\cdot)$ is the Gamma function. This distribution is independent of the scale parameters σ mentioned before, being a function only of the power exponent n . The Combined Rayleigh fit is a special case of this model with $n = 2$ for weak nonlinearity. The power exponent n becomes the only fitting parameter. In the high loss case where the Rayleigh fit is valid, the fitting parameter n shows a decrease from 2.11 to 1.85 as the input power increases from -5 dBm to +10 dBm, indicating saturation of the nonlinear circuit.

However, in the low loss case where both the Rayleigh and Combined Rayleigh fits fail, the 2nd harmonic statistics still fit well to the Double-Weibull distribution. Fig. 2.8(a) shows fits to the Double-Weibull distribution with $R^2 = 0.997$, however the fitted n is 2.50 in the low loss case. It should be noted that the nonlinear circuit is the same and has been explicitly characterized to obey a square law ($V_{2f} \propto V_{1f}^2$) in the operating regime of the experiment. A value of $n = 2.5$ for second harmonic generation is therefore un-physical. Therefore the changing statistical distribution from the Combined Rayleigh distribution is not only due to changes in the nonlinearity strength but also loss of the cavity. For second harmonic statistics, stronger nonlinearity causes n to decrease below 2; whereas low loss causes n to increase beyond 2. In the high loss case, the fitting parameter of the Double Weibull model approaches 2, with $n = 2.08$, as shown in Fig. 2.8(b). On the other hand the Random Coupling Model based approach predicts the statistics very well both in the low loss (Fig. 2.8(a), $R^2 = 0.997$) and high loss environment (Fig. 2.8(b), $R^2 = 0.987$), it demonstrates that Eq. (3) of the main text with the Random Coupling Model provides a simpler and physically reasonable explanation of the

data.

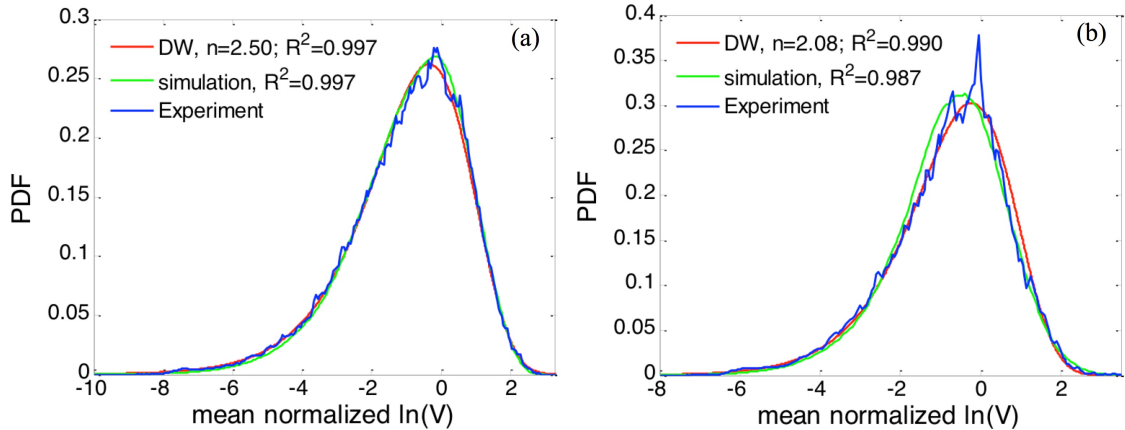


Figure 2.8: Double Weibull and RCM based simulation fit to the mean normalized induced 2nd harmonic voltage statistics between port 1 and 2 in: (a) low loss case, $\alpha_1 = 0.30$, $\alpha_2 = 0.78$, $P_{in,1f} = -5$ dBm, $R^2(simulation) = 0.997$, $R^2(D - Weibull) = 0.997$; and (b) high loss case, $\alpha_1 = 2.85$, $\alpha_2 = 4.56$, $P_{in,1f} = 0$ dBm, $R^2(simulation) = 0.987$, $R^2(D - Weibull) = 0.990$, Frequency range 7 GHz - 9 GHz of the 1/4-bowtie cavity.

2.5 Conclusions

In summary, by adding an active nonlinear circuit to the ray-chaotic 1/4-bowtie cavity, and extending the Random Coupling Model, it is possible to predict the statistics of harmonics in a nonlinear wave chaotic system. The model of nonlinear cascaded cavities Eq. (2.2), which incorporates nonlinearity into the Random Coupling Model, describes the effects of the active nonlinear circuit, and is valid both in the low loss and high loss regimes. This is the first effort to extend the RCM to the nonlinear domain. It is shown to be more general compared to previous models of similar phenomena. The model does not require any fitting parameters although a fair amount of independently-determined system-specific information is incorpo-

rated into the model. The artificially fabricated nonlinear circuit is uni-directional, filtered and amplified to produce only 2nd harmonics, making the system simple to analyze. It paves the way for generalizing RCM to more complicated nonlinear situations. It also offers an approach to nonlinear problems in acoustic, optical, atomic and other chaotic systems.

Chapter 3: Diode Loaded Bowtie Microwave Billiard

Nonlinear effects in wave chaotic systems manifest as harmonic and sub-harmonic generation, driving amplitude dependent responses, etc. We have previously studied the statistics of harmonics generated in a wave chaotic system by adding an active frequency multiplier to the 1/4-bowtie microwave billiard [2], which is a vertically thin (less than a half-wavelength) microwave cavity whose horizontal shape resembles a quarter of a bowtie (Fig. 3.1). This is quite relevant to the work that investigates the electromagnetic field statistics created by nonlinear electronics inside a wave chaotic reverberation chamber, and it has a number of applications in the EMC (Electromagnetic Compatibility) community, such as electromagnetic immunity testing of digital electronics [81,84]. Another approach to observe nonlinear effects is to create a scattering system with amplitude dependent response. To achieve this, we have introduced different sources of nonlinearity into the billiards, and in this chapter we focus on a high frequency diode. Reaching the nonlinear regime usually requires high amplitude inputs, hence we have implemented a high power vector network analyzer (VNA) which is able to measure the scattering (S) parameters for signals up to $\sim +43$ dBm ($\simeq 20$ Watts).

This chapter studies nonlinear wave chaotic properties by introducing diodes

into the bowtie billiard. Almost the electronic devices in real life contain nonlinear circuit elements such as diodes, transistors, etc, and the diode is the most common and fundamental nonlinear element. It is very convenient to add a diode as a point-like nonlinear element into the wave chaotic system. When adding this point-like nonlinearity, it can be incorporated into the source port to construct a nonlinear source, or it can also be added randomly into the billiard at locations far away from the source to form a nonlinear environment. The following two sections study these two cases correspondingly, starting with the simplest case where only one diode is added.

3.1 Bowtie with a Nonlinear Port

In this work, we show the results for measurements of the nonlinear scattering parameters in a diode-loaded 1/4-bowtie quasi two-dimensional microwave cavity. The 1/4-bowtie cavity is a ray-chaotic billiard that displays universal statistical properties predicted by RMT and RCM [11, 12, 24–26, 35, 37, 42, 72, 73, 79, 85, 86]. In this case the diode acts as a nearly point-like nonlinearity in a wave chaotic system. Attaching a diode to the excitation port, we observed that the raw cavity statistics of the impedance change substantially with the excitation power. We extend the RCM to this situation and use it to analyze our experimental results. We find that when the radiation impedance becomes nonlinear, short orbits between the port and a nearby wall, and the raw impedance statistics are strongly modified. We also find that many of these changes are due to the fact that the admittance of the diode

changes with the excitation power. The nonlinear diode competes with the cavity admittance, substantially altering the response of the system. By implementing the lossy port model extension of the RCM [48–50], the results are well explained by the changing radiation efficiency of the diode-loaded port. As a result, The diode effectively acts like a protection element in this configuration.

In the small signal limit, our system can be approximated as linear. To observe a nonlinear response, the system must have some sort of nonlinear property, and a large excitation signal is required. In our earlier studies of wave chaotic systems with one port or multiple ports, we measured the scattering parameters and used these measurements to study the statistical properties of the system. Here we measure the high power S-parameters including a nonlinear element in the wave system, at power levels achievable up to +43 dBm.

The Vector Network Analyzer (Keysight N5242A PNA-X) has been upgraded with high power option H85 [6]. By removing the bias tee, it enables fully calibrated high power S-parameters measurements up to 20 W (+43 dBm). The external booster amplifier, coupler, attenuator, and isolators are chosen as follows. We have used an RF-Lambda amplifier RFLUPA0218G5 working in the frequency range of 2-18 GHz, with output power up to +38 dBm (3 dB compression). By adding couplers (RF-Lambda RFDC2G18G20) and additional attenuators, this configuration is optimized for high power measurement. Note that the signal to noise ratio (SNR) is decreased as the excitation power decreases. Measurements are taken at powers of -5, +5, +15, +25, and +30 dBm, in the frequency range 4 ~ 18 GHz, limited by the isolator (Fairview Microwave SFI0418) bandwidth.

To induce strong nonlinearity, a diode (Infineon BAS7004 with two diodes in the package but only one is electrically connected) is soldered between the center pin and cavity ground, as shown in the inset to Fig. 3.1. From the datasheet [87], this diode has low transition capacitance, $C \sim 1.5$ pF at 1 MHz, which decreases nonlinearly to ~ 0.5 pF as the reverse voltage increases. Its differential resistance also changes nonlinearly as a function of the forward current. For typical forward currents $I_F = 1 \sim 15$ mA, the resistance R changes from 80 to 20 Ω . A rough estimate for the time constant $\tau_{RC} = RC \sim 100$ ps, which is close to the charge carrier life-time as given in the data sheet. Thus this diode can respond in the GHz frequency range and produces clear nonlinear responses, making it suitable for our microwave wave chaos experiments [88, 89]. In addition, the diode package is significantly smaller than the wavelengths used in this study (30-75 mm), rendering it approximately “point like”. The connection shown in Fig. 3.1 has advantages in terms of stability and reproducibility, due to the fact that when the bowtie billiard is opened, the antenna and the top plate are attached together as one piece, and the bottom plate is a separate piece. This in turn allows for excellent reproducibility of $\bar{\bar{Z}}_{rad}$, $\bar{\bar{Z}}_{cav}$ and $\bar{\bar{Z}}_{avg}$ measurements.

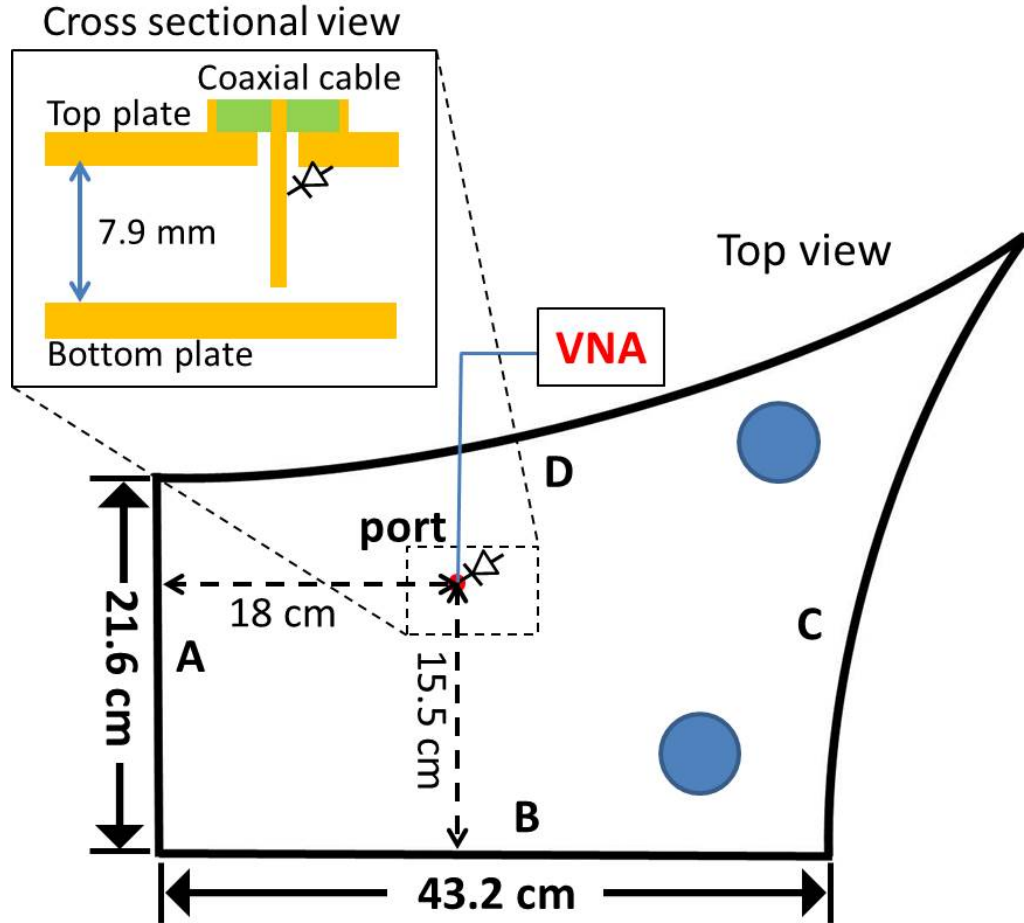


Figure 3.1: Top view of the experiment setup of the 1/4-bowtie quasi-2D microwave billiard loaded with a diode attached to the single port. The diode (Infineon BAS7004) is connected between the center pin of the port and the top plate. The antenna pin is 7.6 mm long, 1.27 mm in diameter. The diode package has dimension $1.3 \times 2.9 \times 1 \text{ mm}^3$. The Vector Network Analyzer (Keysight N5242A PNA-X) measures the scattering parameter at excitation levels up to +43 dBm with microwave wavelengths from 3 to 7.5 cm. The two blue solid circles are metallic perturbers that can be moved around to create ensemble realizations. The inset shows a side-view cross section through the diode-loaded antenna.

3.2 Results

3.2.1 Diode-Loaded Port Radiation Impedance

We first characterize the nonlinear port by measuring the radiation impedance. The radiation impedance characterizes the port properties alone. It is measured by creating an outward-only wave propagation condition in the experiment. This is achieved to good approximation by covering the perimeter of the bowtie billiard with microwave absorbers, as shown in Fig. 3.2(a). The radiation impedance measured without the diode is nearly identical for different input powers. Based on our measurements it is safe to assume that there are no clear nonlinear effects due to the microwave absorbers. Fig. 3.2(b) shows the measured radiation scattering parameter S_{rad} at different input power levels, and includes the case of the antenna without the diode as well. Firstly, by adding the diode, the coupling of the port has been changed substantially. The optimal coupling near 6 GHz for the antenna has been moved to 8 ~ 9 GHz when the diode is added. Comparing the nonlinear port radiation impedance at different power levels, there is a nonlinear change in the 4 ~ 9 GHz range. The coupling is better at low power and the port generally reflects more as power increases.

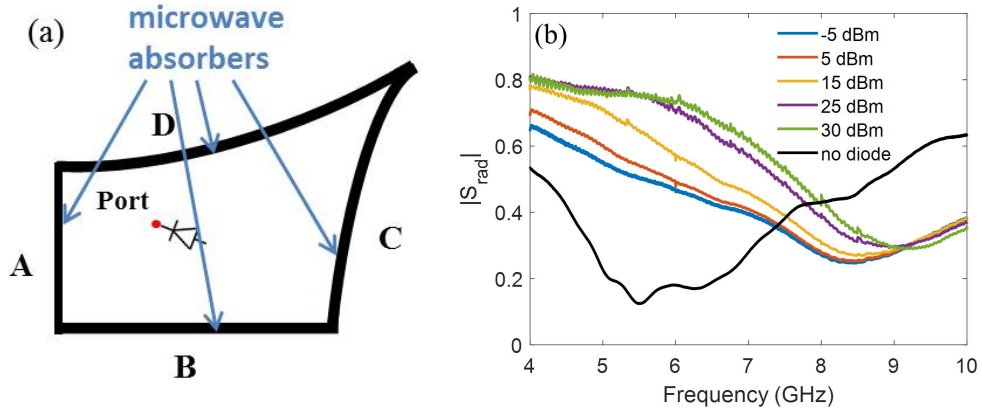


Figure 3.2: (a) Schematic illustration of the perimeter of bowtie covered with microwave absorbers to facilitate measurements of the radiation impedance with walls A, B, C and D labeled. (b) Measured $|S_{rad}|$ in the radiation case at different input powers, compared to the case of the antenna with no diode.

3.2.2 Short Orbits

Short orbits are another system specific feature that the RCM can incorporate for a more complete characterization of a complex scattering system. Short orbits between the ports can survive over an ensemble average because they appear in many or all of the realizations without modification. In refs. [27–29], the theory was developed and experimentally validated. The results for a single short orbit measurement are shown in Fig. 3.3. The inset of Fig. 3.3(a) is the experimental configuration for measuring a short orbit between the port and wall A of the billiard. The microwave absorbers of wall A are removed, so that there is a ray that goes into the billiard through the port and immediately reflects from wall A and goes back to the port. The direct measurements of the reflection S-parameter S_A for this case are shown in Fig. 3.3(a). We interpret the systematic wiggles in $|S_A|$ versus

frequency (Fig. 3.3(b)) as arising from the short ray trajectory. The periodicity is a function of the distance between the port and wall A. The experimental short ray impedance correction is given by [28, 29]

$$\bar{z}_{cor}^{Exp} = Re\{\bar{Z}_{rad}\}^{-1/2} \cdot (\bar{Z}_{wall} - \bar{Z}_{rad}) \cdot Re\{\bar{Z}_{rad}\}^{-1/2}, \quad (3.1)$$

where \bar{Z}_{wall} is the measured impedance of the billiard with specific wall(s) exposed, and \bar{Z}_{rad} is the radiation impedance as deduced from the data in Fig. 3.2. Theoretically, the short ray correction here is given by [27–29]

$$z_{cor}^{Theory} = -exp[-(ik + \kappa)L - ikL_{port} - i\pi], \quad (3.2)$$

where z_{cor}^{Theory} is the correction to the impedance due to the short ray that goes into the billiard through port 1 and goes back through port 1, κ is the effective attenuation parameter that takes account of propagation loss, L is twice the distance between the nonlinear port and the exposed wall, which is 36 cm here, L_{port} is the port-dependent constant length between the antenna and the input/output port. L_{port} is typically 1-2 cm and is caused by the difference in location between the calibrated reference plane at the end of the VNA transmission line and the practical reference plane at the port antennas, due to the additional length in the SMA connector.

Fig 3.3(b) shows the comparison between the theory and experiment for the low power (-5 dBm) and high power (+30 dBm) cases. For the low power case, the periodicity of the short ray z_{cor}^{Exp} agrees reasonably well with the theory, although the amplitude of the experimental curve varies with frequency. For the high power case, there is larger disagreement between the theory and the experiment, both

in periodicity and amplitude. This indicates that this nonlinear port destroys the simple short orbit behavior, although at low power, it can still be approximated as a linear port. As will be shown below, the deviation at high power is because the diode admittance gets larger under high power excitation, such that it dominates over the billiard admittance. As a result, the short ray impedance correction is strongly modified. To some extent, this applies to the low power case as well. Another concern is that the short ray calculation assumes the port to be a point-like object. By attaching the diode, whose dimension is comparable to the antenna, this nonlinear port has a more complicated structure, rendering the port an extended object with no single “position” for the short-orbit calculation.

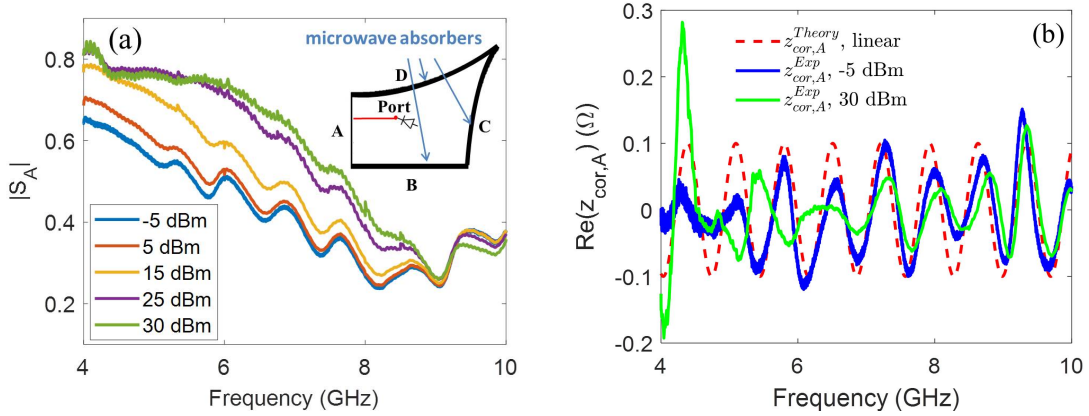


Figure 3.3: (a) S_A measurement results as a function of frequency due to one short orbit between the port and wall "A" shown in the inset. The short orbit creates systematic variations in the S-parameters. The periodicity is related to the distance between the port and the exposed wall. The inset shows the experimental configuration for measuring the short orbit. The microwave absorbers are removed from wall A only, creating a single short orbit between the port and wall A. (b) Comparing short orbit corrections to impedance, $Re(z_{cor,A})$ from the experimental results for low power (+5 dBm, blue) and high power (+30 dBm, green) cases, with theoretical calculation (red), which assumes a linear response.

3.2.3 Ensemble Realizations

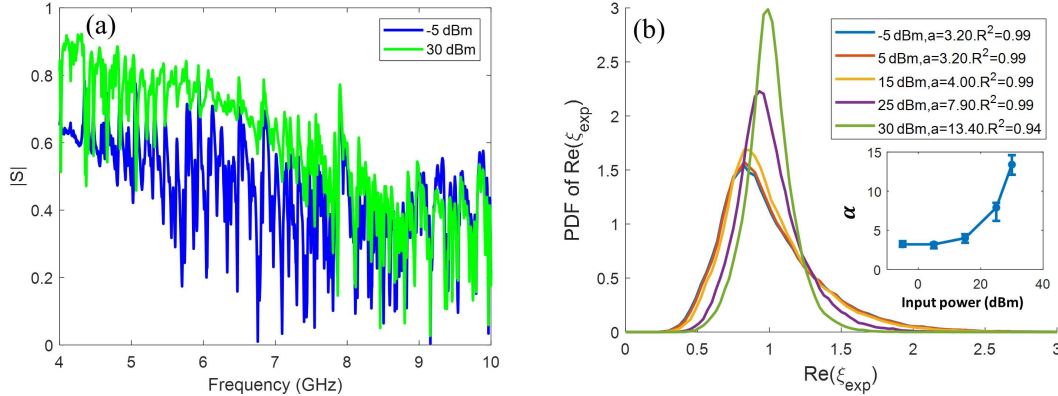


Figure 3.4: (a) Comparing the reflection S-parameter $|S|$ of a typical single realization of the 1/4-bow-tie cavity with diode-loaded port for low power (blue, -5 dBm) and high power (green +30 dBm). (b) Histogram of normalized $Re(\xi)$ obtained from ensemble data using traditional linear RCM for a 1 GHz window centered at 7 GHz. The resulting fitted loss parameter α increases with power as shown in the inset. R^2 values in the legend indicate the goodness of fit [2].

Having studied how the system specific properties change in the presence of the nonlinear port, we next analyze the statistics of the cavity itself. The microwave absorbers are removed from all of the walls of the billiard. The metallic perturbbers shown in Fig. 3.1 are moved around to create 120 distinct static realizations. Fig. 3.4(a) shows reflection vs. frequency results for a typical realization for low (blue) and high (green) input power. They have similar shapes as in the radiation case, but are “dressed” with many resonance fluctuations. The linear RCM approach applies well in the low power case, and we follow the RCM normalization process to determine an experimental approximate, ξ_{exp} [28,32,79]. Fig. 3.4(b) shows, PDFs of $Re(\xi_{exp})$ in the 6.5 to 7.5 GHz range for several different input powers. Clearly the

PDF of the normalized impedance $Re(\xi_{exp})$ changes substantially with power, being more widely distributed in the low power case, indicating stronger fluctuations, a property which is associated with lower loss parameter α . Note that the $Re(\xi_{exp})$ distribution is more concentrated near unity as power increases, consistent with a high loss (high α) situation. If we naively fit this distribution function to the RCM using α as the sole fitting parameter, the fitted loss parameter α increases with power, as shown in the inset. The raw statistics of the system change substantially with power because of the presence of the nonlinear port. However it should be noted that these ξ_{exp} PDFs show substantial deviations from RMT predictions (note the low fit R^2 values at high power), making it clear that naive application of the RCM breaks down in the nonlinear regime.

3.2.4 Radiation Efficiency of the Nonlinear Port (High Loss System)

In the RCM treatment presented above, we expect the loss parameter of the system to be independent of the excitation power as long as the properties of the cavity remain unchanged. The nonlinear property in this case is only associated with the port. The RCM described in Eq. (1.6) is derived assuming a lossless linear port. But this is no longer the case in this experiment. As we can see from Fig. 3.4(a) particularly in the vicinity of 6 GHz, the fluctuations are suppressed in the high power case, indicating that excitations of the cavity modes is suppressed. In this case, the port must be considered as a lossy port. Ref. [48, 49] have derived a generalization of the RCM to account for the loss of the port. A radiation efficiency

η is introduced to quantify the ratio of the power radiated by the port to the input power to the antenna, $\eta = P_{rad}/P_{in}$, (η is real and $0 \leq \eta \leq 1$). In a high loss system (i.e. $\alpha \gg 1$), it can be shown that the impedance of a lossy antenna inside a complex enclosure can be approximated as

$$\bar{\bar{Z}}_{in} = \bar{\bar{Z}}_{ant} + \eta \cdot Re\{\bar{\bar{Z}}_{ant}\} \cdot \delta\bar{\bar{\xi}}, \quad (3.3)$$

where η is the radiation efficiency of the antenna, $\delta\bar{\bar{\xi}} = \bar{\bar{\xi}} - \bar{\bar{I}}$, $\bar{\bar{I}}$ is the identity matrix with diagonal elements $1 + i0$, and $\bar{\bar{Z}}_{ant}$ is the input impedance of the lossy antenna radiating in free space. Ref. [50] has successfully applied this model to a scaled cavity, where the radiation efficiency accounts for the loss in free-space propagation suffered through a remote injection path. In our case $\bar{\bar{Z}}_{in}$ can be considered as $\bar{\bar{Z}}_{cav}$ and $\bar{\bar{Z}}_{ant}$ can be considered as $\bar{\bar{Z}}_{avg}$, therefore Eq. (3.3) can be modified as

$$\bar{\bar{Z}}_{cav} = i \cdot Im\{\bar{\bar{Z}}_{avg}\} + (\bar{\bar{I}} + \eta \cdot \delta\bar{\bar{\xi}}) \cdot Re\{\bar{\bar{Z}}_{avg}\}, \quad (3.4)$$

which is valid in the limit $\alpha \gg 1$. To determine η for the nonlinear port, we first measure $\bar{\bar{\xi}}_{cav}$ of the billiard when there is no diode attached to the antenna. In that case $\bar{\bar{\xi}}_{cav}$ describes the properties of the billiard alone, (because all system-specific properties have been removed), and as such it is a linear system. We use the linear RCM approach, creating 120 realizations with the two perturbers, then applying Eq. (1.6) to extract $\bar{\bar{\xi}}_{cav}$ and fit to RCM to find the corresponding loss parameter α [28, 32, 79]. Additionally, to make the bowtie billiard a high loss system, the perimeter of the billiard is partly (but uniformly) covered with microwave absorbers, tuning the loss parameter to be $\alpha = 3$ (4.5 GHz) to $\alpha = 7$ (9.5 GHz). Then using the value of α which characterizes loss in the cavity and $\bar{\bar{\xi}}_{cav}$, we go back to the

diode-loaded nonlinear port case, utilize Eq. (3.4) and vary η so that the statistics of $\bar{\xi}(\eta)$ agrees with $\bar{\xi}_{cav}$. Fig. 3.5(a) shows the fitted radiation efficiency from $Im(\xi)$ statistics, (the $Re(\xi)$ statistics give similar results).

Fig. 3.5(a) shows that the radiation efficiency is strongly power-dependent in the frequency range 4 ~ 10 GHz. Between 6 and 9 GHz, the radiation efficiency decreases with increasing power, meaning the port is getting more lossy as the excitation power increases. There is a cross-over regime at low frequency 4 ~ 6 GHz, where the radiation efficiency increases at high powers. And although it is not shown in the plot, at 10 GHz and above, the radiation efficiency is almost independent of power.

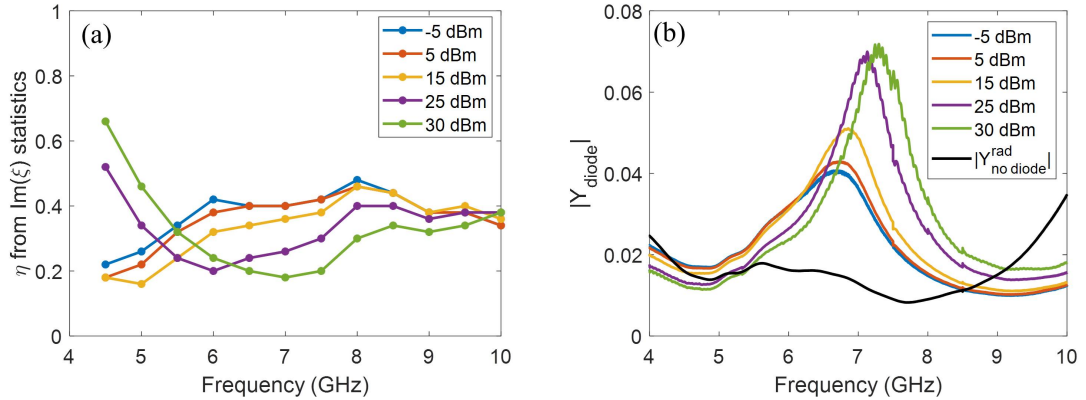


Figure 3.5: (a) Fitted radiation efficiency η (from $Im(\xi)$ statistics) vs. frequency and power. Each fit was done with data from 120 realizations and a window of 1 GHz. (b) Plot of diode admittance magnitude vs. frequency at various rf powers, as well as the radiation admittance of the linear port $|Y_{no diode}^{rad}|$

To explain the results, we are interested in characterizing the diode admittance under different excitation powers. The diode is connected between the center pin and the ground of the port. The billiard radiation admittance can also be

considered as being connected between the center pin and ground. Therefore a simple model is constructed by considering the diode and the billiard to be connected in parallel. By measuring the port radiation admittance with ($Y_{with\ diode}^{rad}$) and without the diode ($Y_{no\ diode}^{rad}$), the diode admittance can be approximated as $Y_{diode} \simeq Y_{with\ diode}^{rad} - Y_{no\ diode}^{rad}$.

Fig. 3.5(b) shows the experimental results of $|Y_{diode}|$ compared with $|Y_{no\ diode}^{rad}|$. Between 4 ~ 6 GHz, $|Y_{diode}|$ has similar values to $|Y_{no\ diode}^{rad}|$ and changes little with power. Thus the diode admittance competes roughly equally with the billiard admittance. A small change in admittance value may result in a big change in fitted radiation efficiency. However, between 6 and 9 GHz, the diode admittance dominates the billiard admittance and generally increases with power. In this frequency range, because the diode admittance is much larger than the billiard admittance and increases with power, the radiation efficiency of the port decreases, consistent with the results in Fig. 3.5(a).

To better understand the nonlinear port, we built a circuit model for simulation in the finite difference time-domain code called CST(Computer Simulation Technology). The SPICE models of the diode as well as the package are provided by the manufacturer. In addition to the SPICE models, the dielectric properties of the package near the port also affect the radiation impedance, and this was added to the model. The internal capacitances of the package SPICE model were altered because the diode is being used beyond its design frequency range. The simulated amplitude dependent radiation S-parameters show relatively good agreement with the experimental results (see section “Simulation in CST”). In addition the resultant

radiation efficiency that is directly calculated as P_{rad}/P_{in} is in general agreement with the experimental results. Based on the circuit model, the nonlinearity arises from the diode, which is approximated with an exponential I-V diode function [90]. The diode nonlinearity is shorted by parasitic capacitance in the package SPICE model at high frequencies, thus the port model does not have power dependence at 10 GHz and above, consistent with the data.

3.2.5 Simulation in CST

To create a model that resembles the nonlinear port in CST, we first draw a 3D model that has the same dimensions as the physical port. All of the product information about the diode and its packaging can be found on the manufacturer’s webpage [87]. We have taken into account the diode package dimensions, the SPICE model of the diode and the SPICE model of the package. Fig. 3.6(a) shows the port configuration in CST. The physical diode package is approximated as a dielectric block with its relative dielectric constant used as a fitting parameter (fitted $\epsilon_r = 10$ as shown in Fig. 3.6(a)). The radiation scattering parameter is a property of the port, hence the shape of the cavity does not play a role. In other words we establish a condition where the waves radiating from the port are not reflected back to the port. To achieve this, the top and bottom parallel rectangular plates are terminated with radiation boundary conditions. There is only one external excitation port which is defined on the antenna, and it is labelled as the yellow block with number “1” in Fig. 3.6(a). To include the SPICE model of the diode and package, another differential

port, port 2, is also built between the center pin and ground. The SPICE models of the diode and the package are integrated into one file "pack2d_v5" and attached to port 2. The details of the SPICE model are given in Fig. 3.6(b). There are two diodes in the package, and three pins, but we only connected two pins, say between node 3 and node 2. The package model is specified to be valid up to 6 GHz. To adapt the model to our situation where frequency is applied up to 18 GHz, we have adjusted all the parasitic capacitances, i.e. C13, C23, and C12, to be approximately 2 orders of magnitude smaller than specified. The diode model for D1 and D2 is the standard SPICE model including both DC characteristics and dynamic effects.

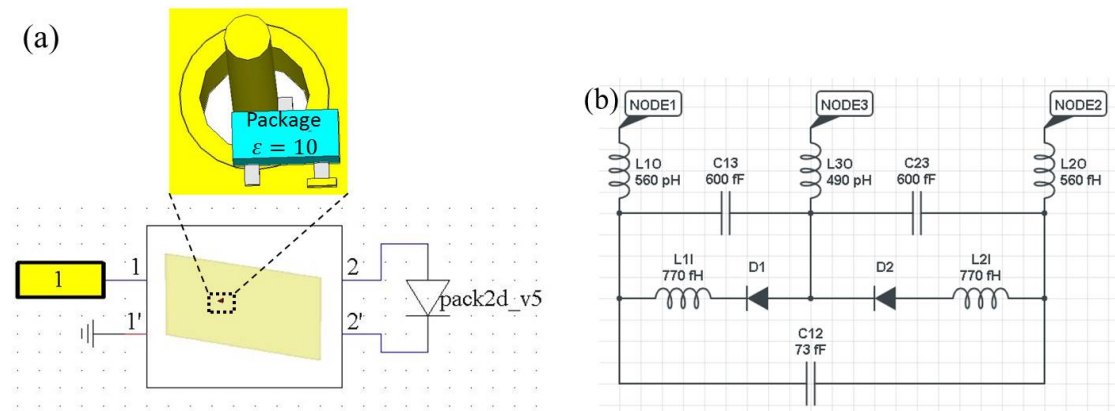


Figure 3.6: (a) Model in CST to simulate the radiation S-parameters of the nonlinear port. The physical dimension and dielectric properties of the diode package are included in the CST model. Note that the parallel plate waveguide is terminated with radiating boundary conditions on all sides. (b) The complete SPICE model of the diode and the package, indicated as 'pack2d_v5' in (a).

The results of the simulation are shown in Fig. 3.7(b), and compared with the radiation case experimental results shown in Fig. 3.7(a). The black curve is the radiation S-parameter for the linear case where there is no diode attached to the port. Adding the diode, the overall coupling to the cavity is changed substantially,

and this is captured in the model. When changing the amplitude of the incident wave from 0.1 V to 10 V, the simulated radiation S-parameters show similar amplitude dependence as the experimental results. Thus the model captures the essential behavior of the nonlinear port radiation properties.

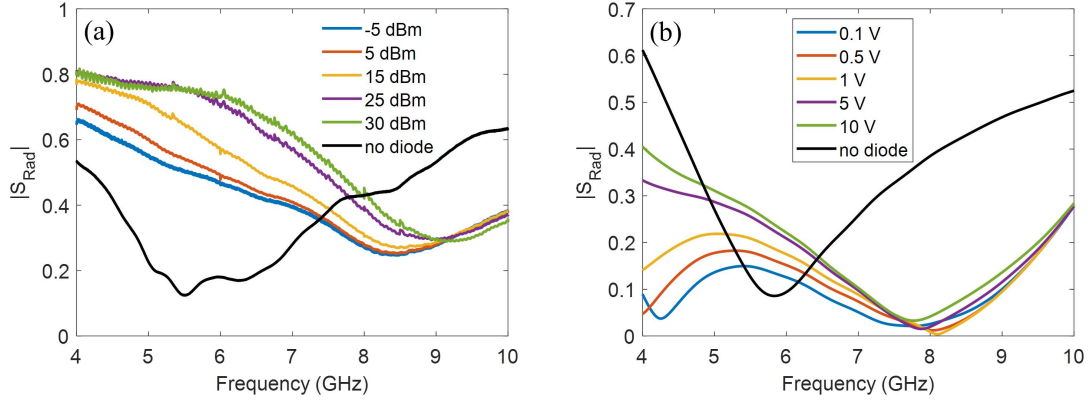


Figure 3.7: (a) Experimental results of the radiation S-parameters at different input powers. (b) Simulation in CST by importing the SPICE model of the diode and package, and adding a dielectric block representing the physical dimension of the package. $|S_{Rad}|$ for different amplitudes with diode and no diode case.

Furthermore, we are also able to simulate the port radiation efficiency, which is the ratio of the radiated power to the input power at the port. The total power from the source P_{tot} is decomposed into several parts, i.e. the power directly reflected by the port P_{ref} , the power loss at the port, the power loss in the cavity, and the power radiated through the boundary P_{rad} . The power loss by the cavity is the Ohmic loss of the copper parallel plate which is negligible. The input power at the port can be calculated from the difference between the total power P_{tot} and the reflected power P_{ref} . In the simulation, the total power is a constant over frequency, and the reflected power can be calculated from the simulated S_{11} . To get the radiated

power, we have defined 4 faces along the boundary of the parallel plate model, as shown in Fig. 3.8. By integrating power on these 4 faces and summing them up, we can get the total power radiated P_{rad} .

The radiation efficiency η is then calculated as $\eta = P_{rad}/(P_{tot} - P_{ref})$. Fig. 3.9(b) shows the simulated radiation efficiency for different input amplitudes of the nonlinear port. Also shown are the experimental results in Fig. 3.9(a), where the radiation efficiency η is fitted by comparing the statistics of normalized impedance ξ with that in the linear case. It is clear that the CST simulation reproduces the key features of the experimental case. There is a regime in which η increases with power at low frequency. In the intermediate frequency regime, the radiation efficiency decreases as the incident power increases. At high frequency, the behavior tends to be power independent. Therefore we conclude that the radiation efficiency model captures the essential behavior of the nonlinear port.

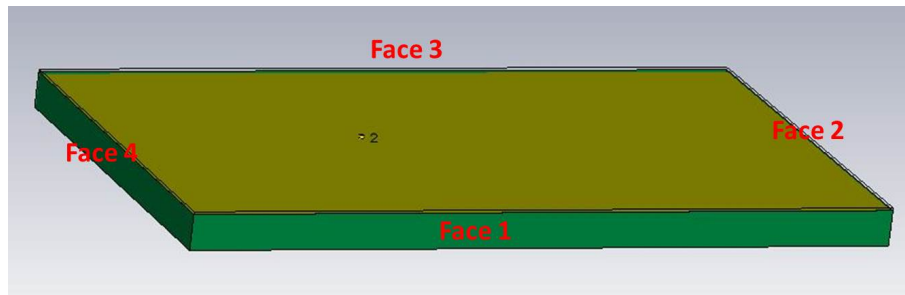


Figure 3.8: Model in CST to simulate the radiation efficiency with the nonlinear port. Four faces are defined along the perimeter of the parallel plate structure, and the port is labelled ‘2’. The total power radiated through the boundary can be calculated by integrating the power density along each face, and summing them up along these 4 faces.

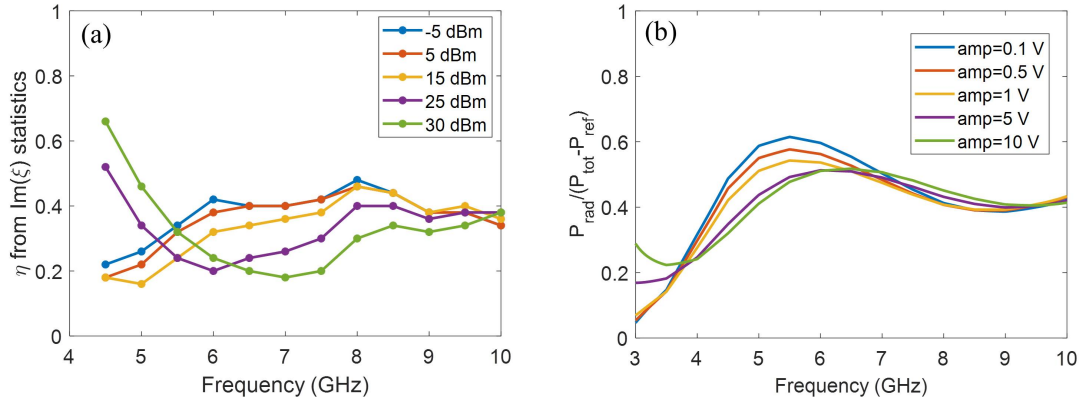


Figure 3.9: (a) Experimental radiation efficiency obtained by fitting the statistics of ξ . (b) Radiation efficiency simulated in CST, by directly calculating the ratio of $P_{\text{rad}}/(P_{\text{tot}} - P_{\text{ref}})$.

3.3 Discussion and Future Work

3.3.1 Nonlinear Port with a Diode

We have shown that by attaching a diode to the center pin and ground of an antenna, the port shows dramatic nonlinear behavior. By measuring the radiation impedance, which characterizes the port properties, we find the impedance changes considerably with the excitation power. The nonlinearity mainly occurs below 10 GHz, which is consistent with the diode time constant ($\tau \sim 100$ ps, $1/\tau \sim 10$ GHz). “Short orbits” are another system specific property. At low power, the short orbit behavior can still be approximately explained by theory, treating the port as a linear point source. As power increases, the short orbit correction deviates from the theoretical prediction. As the radiation efficiency fitting results show, this is because at high power the diode admittance dominates over the billiard admittance.

For the statistical results, if we blindly apply the RCM to the billiard with diode-loaded port, one finds that the loss parameter increases with input power. The RCM posits that the loss parameter determines the universal properties of the chaotic system. In our case the billiard properties should not change with power because the nonlinearity is only associated with the port. We applied the newly developed radiation efficiency model to the port, using the radiation efficiency η to quantify the proportion of power from the source radiated into the billiard. At high power in the nonlinear region, the diode consumes most of the power, causing the radiation efficiency to decrease. The diode thus prevents high power signals from getting into the billiard [91].

There are several interesting questions for further study of this system. First, the billiard had to be intentionally modified into a high loss system in order to use the radiation efficiency model. The statistics of low-loss nonlinear systems cannot be addressed at this time. In addition, another behavior we have observed is the loss of reciprocity in a two-port version of this system, where one port is a nonlinear port and the other is linear. We observed that $S_{12} \neq S_{21}$ when large amplitude signals are applied. We note there is no general reciprocity theorem that holds for nonlinear systems [92]. This behavior can be understood by considering that with equal powers injected in both ports, the diode will be driven to nonlinearity when power is injected in the port hosting the diode, and to a lesser extent when the linear port is excited.

Besides the approach we used in this paper to analyze the nonlinear system, we mention for completeness that high power S-parameters are sometimes called

hot S-parameters [93], and the nonlinear effects can be fully characterized by the so-called X-parameters measured by the nonlinear VNA [94,95]. However we believe that the present treatment is best suited for understanding the statistical properties of nonlinear wave chaotic systems in the semi-classical regime.

3.3.2 Diode Located in the Billiard

Several kinds of diodes have been tested in the bowtie. In addition up to 30 diodes have been placed randomly in the billiard. While no substantial power dependent S-parameters have been measured so far, this might be due to the fact that the diodes we have used are not coupling well enough to the signals. Simulation in CST has shown that for diodes scattered around the bowtie billiard, there are power dependent statistical features.

Fig. 3.10 is the simulation model of the bowtie billiard with two cylindrical perturbers and a diode connected between the top and bottom plates at a location away from the ports. The diode electric model and parameters are also shown in the figure. The diode is fixed and the two perturbers have been moved around for 90 realizations. The simulation is performed in the time domain to get the S-parameters for each realization. The excitation signal is a Gaussian signal in the frequency range of 2-16 GHz, and its amplitude can be varied.

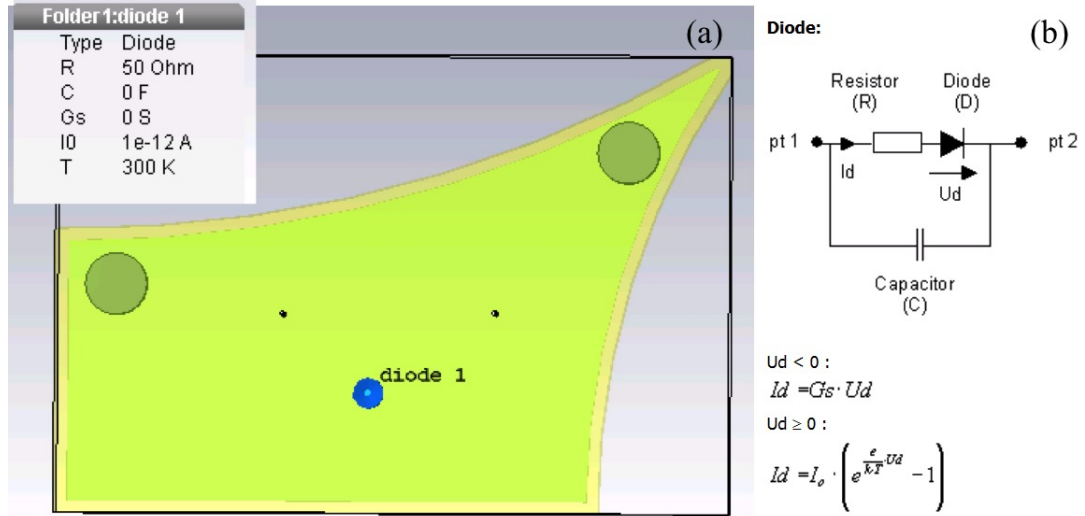


Figure 3.10: Model of the bowtie billiard (a) and diode (b) in CST

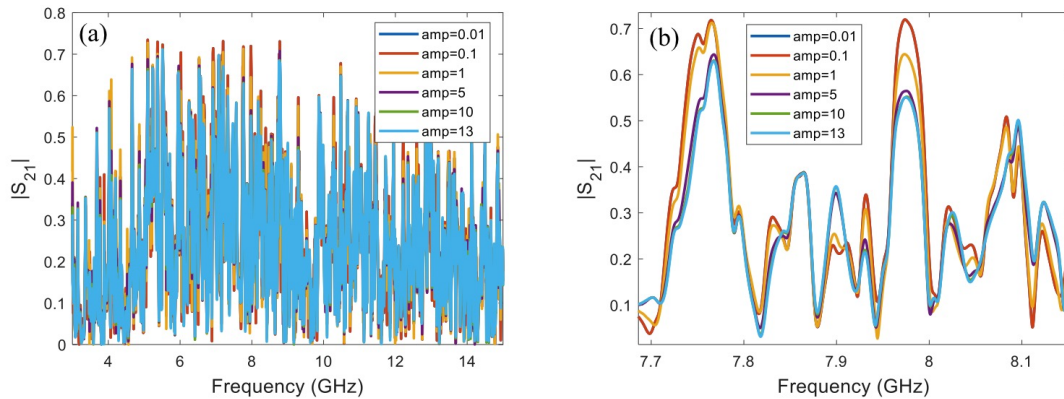


Figure 3.11: Simulated S_{21} for different input amplitudes of the diode-loaded 1/4-bowtie (a) 2-16 GHz range; (b) Zoomed-in view of several modes near 7.9 GHz shows that nonlinearity starts to appear for $amp > 0.1$.

Fig. 3.11 shows the S_{21} of one realization for different excitation amplitudes, ranging from amplitude $amp = 0.01$ to 13. Note that CST uses the unit of \sqrt{W} for the amplitude which is proportional to V (Volt). Fig. 3.11(b) is a detailed view of several resonant peaks near 7.9 GHz, showing that S_{21} changes with the input amplitude. Note that $S_{21}(f)$ with $amp = 0.1$ overlaps with $amp = 0.01$ which

indicates it is in the linear case. For pulse amplitude $amp > 0.1$, nonlinear response from the diode changes S_{21} . For many realizations, the simulation will become numerically unstable if the excitation amplitude is too large. This is because the time step is too large as the amplitude increases. The instability problem can be solved by choosing a smaller stability factor for the time step. As a result of the smaller time step, the total simulation time gets longer. Considering the trade-off, $amp = 0.1$ and $amp = 12$ are selected for the ensemble simulation, which differ by two orders of magnitude in the incident pulse amplitude.

Similar to the case of the nonlinear port experiment, several features mentioned before are also observed for the scattered diode case in simulation. Fig. 3.12(a) shows that $S_{12} \neq S_{21}$ for large amplitude $amp = 12$ while $S_{12} = S_{21}$ for $amp = 0.1$. Note also that S_{avg} is different for $amp = 0.1$ and $amp = 12$, as shown in Fig. 3.12(b).

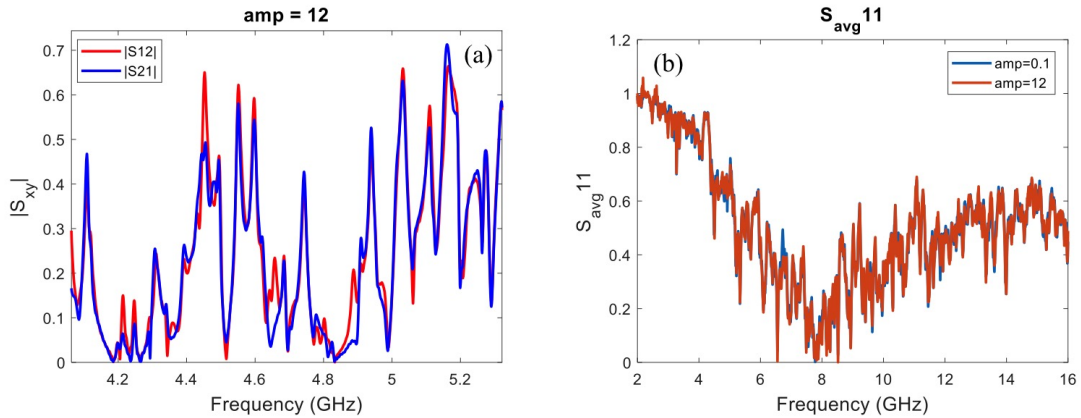


Figure 3.12: Plots of S-parameters vs. frequency in the diode loaded 1/4-bowtie. (a) $S_{12} \neq S_{21}$ for high amplitude, $amp = 12$; (b) S_{avg} over 90 realizations for $amp = 0.1$ and $amp = 12$.

For the statistical analysis, applying the linear RCM algorithm, the statistics

of the normalized impedance $\bar{\xi}$ are shown to be different depending on the excitation amplitudes, as seen in Fig. 3.13(b). As a result, the fitted loss parameter α obtained from the normalized pdfs are different for the different amplitudes. Fig. 3.13(a) shows that the fitted loss parameter α is larger for high amplitude $amp = 12$ compared with the low amplitude case $amp = 0.1$. Recall that in the nonlinear port case, higher input powers result in smaller loss apparent parameter. Further study of this discrepancy need to be conducted. Also differing from the nonlinear port case, these statistical differences are observed for all of the 8 $\bar{\xi}$ quantities, and they are fairly consistent among the 8 quantities. The goodness of fit R^2 are all > 0.99 , indicating very good fit.

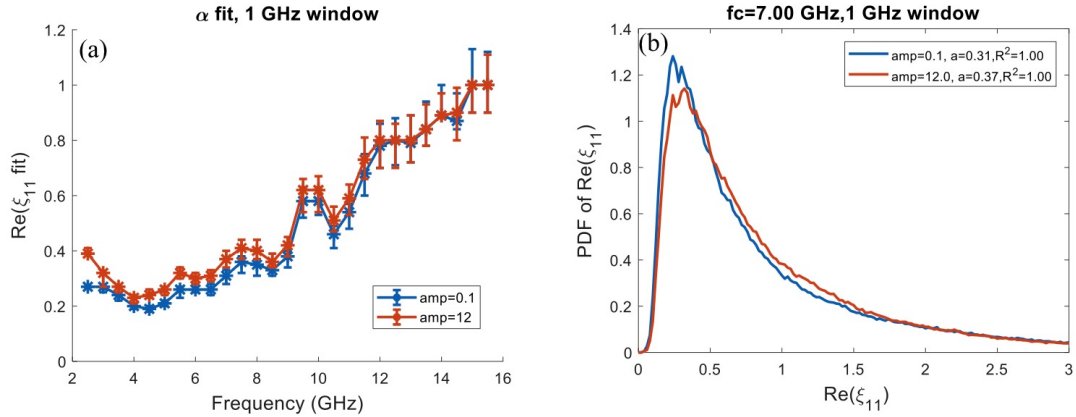


Figure 3.13: (a) Fitted loss parameter α from $Re(\xi_{11})$, using a 1 GHz window for different input amplitudes, the higher amplitude excitation signal results in larger fitted loss parameter; (b) The histograms of normalized impedance $Re(\xi_{11})$ at $f_c = 7$ GHz shows clear differences between the $amp = 0.1$ and $amp = 12$ cases, resulting in different fitted loss parameter.

3.4 Conclusions

To conclude, a diode based nonlinear port alters the radiation impedance, short orbits, and raw impedance statistics of a wave chaotic systems from those observed in linear systems. By using the Random Coupling Model with incorporation of the diode nonlinear properties and a lossy port model, these nonlinear phenomena are well explained, and verified by the simulation. The nonlinear property of the port can be applied to protect delicate circuits from high power electromagnetic microwave interference.

Chapter 4: Superconducting Cut-Circle Microwave Billiards

Besides nonlinear circuits introduced in the room temperature environment, superconducting materials offer another source of nonlinearity at microwave frequencies. Their nonlinearity mainly comes from the surface impedance $Z = R + iX$. This chapter presents the details of the experiments done on two superconducting microwave billiards. One is made of Lead (Pb) material which mainly shows a nonlinear resistivity R , and the other is Titanium Nitride (TiN) on Si wafer which is expected to have a nonlinear reactance X . We are still working on the experiment of TiN on Si wafer billiard. Here, the up-to-date results are recorded.

4.1 Nonlinear Impedance of the Lead Coated Superconducting Cut-Circle Microwave Billiard

The Pb coated on Copper cut-circle cavity has been used for wave chaos measurements by several groups [3, 23]. Below the transition temperature $T < T_c$, for lead $T_c = 7.2$ K, the cavity boundary is made of superconducting material Pb. It has been shown to give rise to a wave chaotic billiard with a very low loss parameter $\alpha \sim 0.01$ [3]. However, materials in the superconducting state are intrinsically nonlinear. Therefore this system is a very good candidate to realize a distributed

nonlinear wave chaotic system.

4.1.1 Experimental Setup

The cavity dimensions are shown in Fig. 4.1(a). The cavity has a height of $h = 0.8$ cm and is considered to be a 2D billiard for frequencies $f < c/(2h) = 18.75$ GHz. The perturber is made of Teflon and the perturbation is done by rotating the perturber (note arrows in Fig. 4.1(a)) through a mechanical feed-through in the refrigerator. The experimental setup and in-situ calibration have been discussed in detail in [3] and here we follow the same procedure. To observe the nonlinearity, the S-parameters are measured at different input powers. We have tried to replace the perturber with a Nb cylinder with diameter of 4 cm. Nb has $T_c = 9.3$ K which may make the system even more nonlinear but will reduce the volume of the cavity since it is metallic. It turns out that the statistical results are not as good as from the Teflon perturber. So we continue to use the teflon wedge perturber.

Fig. 4.1(b) shows the measured transmission S-parameters for different excitation powers at $T = 5.7$ K. One resonant peak at 8.84 GHz is also shown. It shows that by increasing the input power, the resonant peak shifts a little, while the height decreases, indicating that the insertion loss increases. This superconducting cavity mainly shows nonlinear resistive behavior.

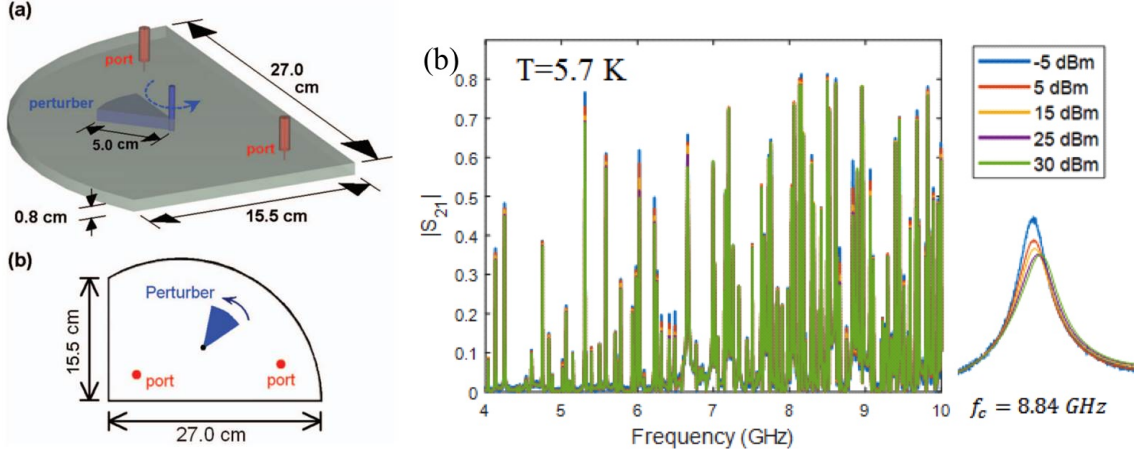


Figure 4.1: (a) From [3], dimension of Pb coated cut-circle cavity with a Teflon perturber. The height of the cavity is $h = 0.8$ cm. Area $A = 0.0409$ m². (b) $|S_{21}|$ of the Pb cut-circle cavity at $T=5.7$ K for different input powers.

To obtain a base temperature below 1 K, all the stainless steel parts are replaced by brass or aluminum to improve their thermal conductivity. Fig. 4.2 shows the experimental setup in the dilution refrigerator. The resulting S-parameters are similar to Fig. 4.1(b) at $T=5.7$ K, but slightly more nonlinear. We also found that $\bar{\rho}_{12} = 0.993$, which is smaller than those obtained in the pulsed tube refrigerator. The S-parameters mainly show resistive nonlinearity. As presented in Fig. 4.1(b), the larger the input power, the lower the resonant peak, indicating a smaller quality factor.

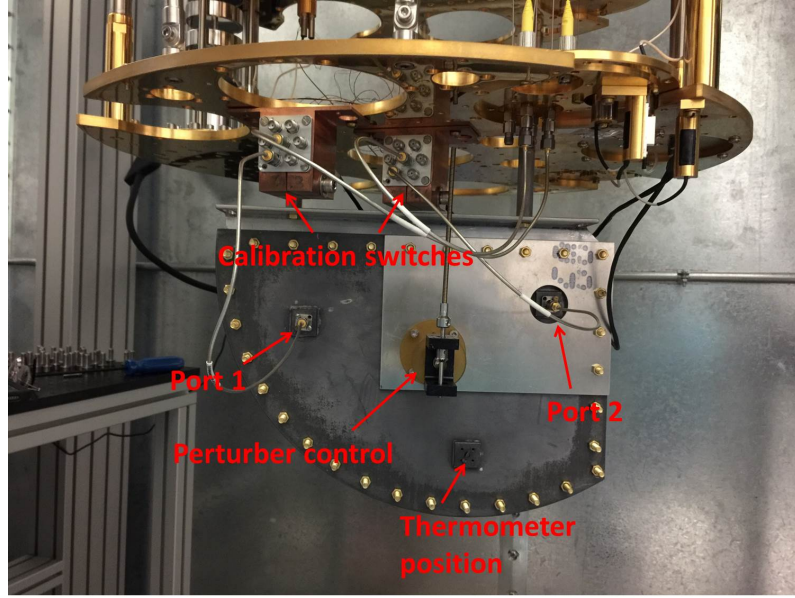


Figure 4.2: Picture of the Pb cut-circle hung on the mixing chamber plate in the BlueFors XLD400 dilution refrigerator.

To create an ensemble of realizations, a perturbation is introduced by rotating the Teflon perturber. Another improvement in the dilution refrigerator experiment is that the mechanical rotation is now controlled by a motor inside the cryostat. Traditionally, the mechanical feed-through requires a rod extending from room temperature all the way down to the cavity in order to rotate the perturber. This configuration requires an opening in the plate at every stage of the fridge. However these openings mean that the thermal radiation can not be totally blocked. In addition there is a thermal connection to the room temperature environment through the rotary axis. One trial has shown that with the manually controlled mechanical feed-through, the lowest temperature reached by the billiard is 600 mK. To avoid this problem, we employ a motor located inside the cryogenic environment. A Phyton VSS stepper motor for in-vacuum and cryo applications is installed and can be

controlled by Matlab through a LabVIEW program (At the time of the experiment, there was a communication/USB port issue with the computer. Matlab sometimes lost communication with LabVIEW, so the perturbation had to be manually monitored by means of the motor for each realization). This setup makes the mechanical perturbation more consistent and automated. However, the electrical current sent to the motor will generate heat, and since the base temperature is below 1 K, the system is very sensitive to even a small amount of heat. Therefore the motor is mounted on the 4 K plate, several stages above the mixing chamber plate. To minimize heat transfer, a stainless steel tube is used to connect the motor and the gear stage that is attached to the billiard. The torque that can be applied by the motor is determined by its current. It has a “stop” current I_{stop} and a “run” or “boost” current I_{run} . I_{stop} is the current supplied when the motor is in the hold position and I_{run} is the current supplied when the motor tries to rotate. A good mechanical arrangement of the billiard and motor can decrease the torque required to hold and move the perturber. In this run, I_{stop} is set to 0.1 A and $I_{run}=1$ A. Powering on the motor has the effect of gradually increasing the base temperature. And whenever the motor is powered to rotate, the temperature on the 4 K plate will have a spike increase of around 0.05 K, see the blue line in Fig. 4.3.

On the other hand, the high power VNA is connected to measure the S-parameters up to +35 dBm. At the highest power $P_{in} = +35$ dBm, for a continuous sweeping time of less than 20 s with 5 averages, the temperature of the billiard could increase from 800 mK to more than 1 K. It then takes around 10 mins relaxation time to get the cavity back to 800 mK. As the input power decreases, the temperature

increase and relaxation time are also smaller. In total, to measure 5 different powers (-5, 5, 15, 25, 35 dBm), it takes ~ 15 mins. The temperature changes during measurement are shown in Fig. 4.3. A maximum of 32001 frequency data points can be taken in each sweep. In order to observe each resonant peak in the S-parameters, a 3 GHz frequency window is swept each time. So for each realization in the 4-16 GHz range, it usually takes 1 hour, and more than one week to measure 100+ realizations.

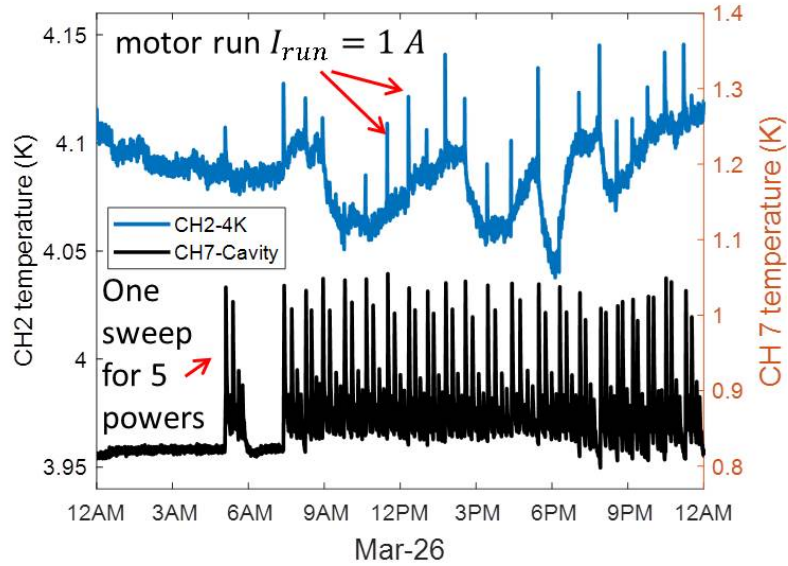


Figure 4.3: Temperature vs. time, blue line (left axis) is the temperature change on the 4 K plate, the spikes indicate when the motor is powered to rotate the perturber in the cavity; the black line is the temperature on the Pb cavity (right axis), a typical measurement sweeps from high power (35 dBm) to low power (-5 dBm) and takes around 15 minutes.

Because of the heat introduced by the motor and VNA, the base temperature of the Pb cavity has increased. When taking ensemble statistics, ideally the cavity is expected to be at the same temperature for each realization. The lower the starting temperature, the longer the time it takes for relaxation. A starting temper-

ature of $T=800$ mK is chosen considering the trade-offs. The motor has a rotation step parameter for each move, a value of 5.6 for that parameter approximates a 1 degree rotation. By rotating the Teflon perturber in this way, an ensemble of 114 realizations at 5 input powers have been recorded.

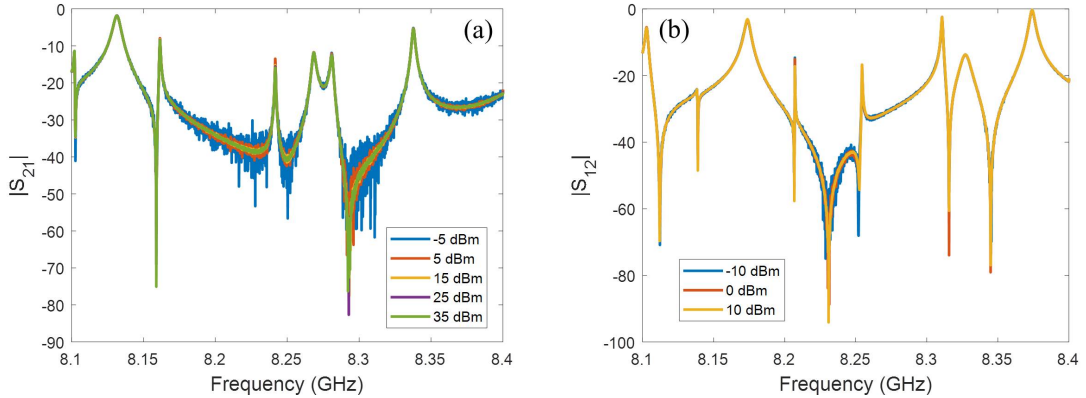


Figure 4.4: (a) Comparing $|S_{21}|$ for different output power levels (-5, 5, 15, 25, 35) dBm, measured with high power network analyzer configuration with the superconducting Pb cavity at 800 mK. The signal-to-noise (SNR) for low power measurement is clearly reduced. (b) $|S_{21}|$ for different input powers (-10, 0, 10) dBm, measured with a network analyzer in the standard configuration.

Because of the external components (amplifier, coupler, isolator, etc) used, the PNA with high power option imposes some limitations in dynamic range and frequency. Especially at low powers, we can observe that the signal to noise ratio (SNR) of the measured S-parameters is reduced, see Fig. 4.4(a). The reason why the low power results are more noisy is addressed in Appendix C. To have better results at low powers, we have connected another version of the PNA N5242A in the standard low power configuration. A total of 200001 data points are taken in the 4~16 GHz range, at powers -10, 0, 10 dBm, respectively, and 121 realizations are taken. A typical S_{21} result is shown in Fig. 4.4(b). The low power results are

better than those taken with the high power option, and the SNR also improves as power increases. With a rotation angle of 3.4° for each realization, a full circle takes around 106 realizations, as shown in the correlation coefficient $\rho(S_{12}^{(1)}, S_{12}^{(k)})$ in Fig. 4.5(a). In Fig. 4.5(a), the S_{12} correlation $\rho(S_{12}^{(1)}, S_{12}^{(k)})$ between realization No. k and the No. 1 realization is plotted.

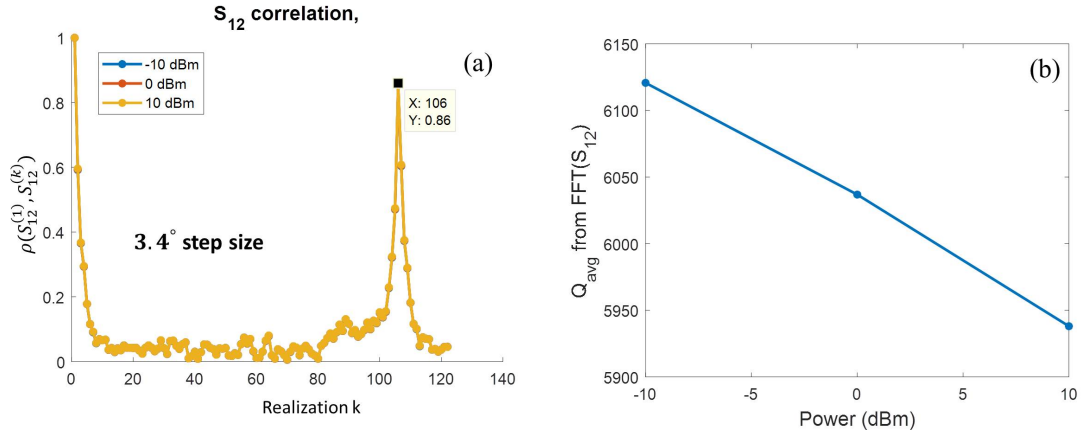


Figure 4.5: (a) Correlation coefficient $\rho(S_{12}^{(1)}, S_{12}^{(k)})$ for realizations of the superconducting Pb cavity at 800 mK measured with low power network analyzer (-10, 0 10) dBm, where k is the number of realizations; (b) Averaged quality factor Q at $T=800$ mK decreases with increasing input power.

Fig. 4.5(b) shows the quality factor Q calculated from the Fourier Transform of S_{12} (4-16 GHz) for the different input powers. (Appendix A Fig. A.4 shows an example for calculation of Q .) Consistent with the single resonant peak shown in Fig. 4.1(b), the higher the input power, the lower the resonant peak, indicating a smaller quality factor. The surface resistance of the cavity can be nonlinear for a number of reasons. One possibility is that the higher input power brings heat locally to the cavity. Some domains of the cavity experience a local temperature increase. The surface impedance $Z_S = R_S + iX_S$ of the Pb cavity changes with temperature.

It is generally observed in superconductors that R_S increases with temperature. As a result, the resonant peaks in $|S_{12}|$ decrease with increased input power, and so does the quality factor Q .

Concerning systematic errors, there is error coming from the TRL calibration. During the calibration a number of different standards are measured, requiring switching to different channels. There is an assumption that each channel has the same length and characteristics, but this will never be the case in practice [3]. And there are interconnects in the transmission lines from the VNA down to the billiard which will also induce noise.

4.1.2 Noise Effects and Low Loss Limit

Now we have created ensembles of realizations of the superconducting Pb cavity for different input powers. It is very interesting to see whether there are any statistical properties changing with power, especially when the RCM normalization procedure is applied. Following similar procedures to those in [3], the in-situ calibration is applied through Thru-Reflection-Line (TRL) methods followed by the pseudo-open approach. With the calibrated S-parameters, the RCM procedures are applied to get $\overline{\overline{S}}_{avg}$, $\overline{\overline{Z}}_{avg}$, $\overline{\overline{\xi}}$, etc. Those calculations are performed for each power independently. By fitting the statistics of the “universal” impedance $\overline{\overline{\xi}}$, the loss parameter α , which indicates the lossyness of the system, can be extracted. Fig. 4.6 shows an example of $Re(\xi_{12})$ statistics in the 12~13 GHz range for different input powers. The fitted loss parameter α is in the range of less than 0.1. For a

two-dimensional billiard, the loss parameter α is inversely proportional to the quality factor Q , $\alpha = k^2 A / (4\pi Q)$, where $k = 2\pi f / c$ is the wave number of frequency f and A is the area of the billiard. As seen from the single realization results, the quality factor Q decreases with increasing input power, so it is expected that the loss parameter α should increase with increasing input power. However, Fig. 4.6 inset shows that the fitted loss parameter α actually decreases with increasing input power. Also note that the results from the standard network analyzer configuration show generally smaller α compared with the results from the high power network analyzer configuration.

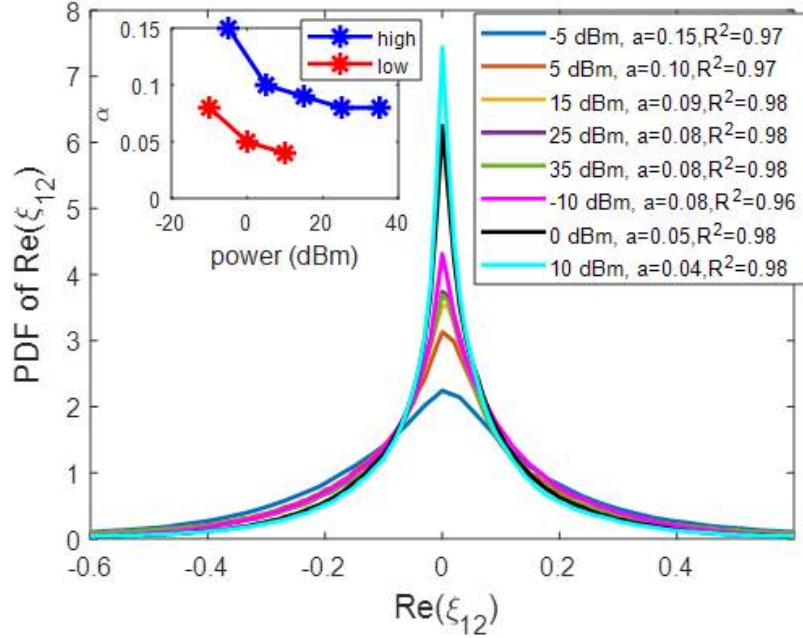


Figure 4.6: $\text{Re}(\xi_{12})$ statistics of the superconducting Pb cavity at 800 mK in the 12~13 GHz range for different input powers, including both high power and standard configurations. The fitted α and goodness of fit R^2 are also given in the legend. The inset shows the fitted loss parameter α vs. the input power, for the high power and low power configurations, respectively.

As we observe in the measured S-parameters shown in Fig. 4.4, we suspect

that perhaps the noise has an effect on the statistical results. This is of particular concern in such a low loss system, which requires a large dynamic range to measure its S-parameters. To analyze the effect of noise on the statistical results, we have done some simulations to artificially add noise to the S-parameters. There are several approaches to adding noise. Firstly, we start from the experimental data. A relatively “clean” set of measured S-parameters is chosen, such as the one measured at high power $P_{in} = 25$ dBm. And then for each realization, a white Gaussian noise is added using the Matlab built-in function *awgn* with parameter *snr*. Fig.4.7(a) shows an example of adding noise of different *snr* to S_{21} data. This artificially modified data displays clear similarity to the measured data in Fig. 4.4. Next, ensembles of S-parameters with different amounts of noise are simulated. We can apply the RCM procedures to obtain the statistical results and the fitted loss parameters. As shown in Fig. 4.7(b), the statistics of $Re(\xi_{12})$ in the 12~13 GHz range change because of noise. In particular note that the fitted loss parameter α increases as the noise intensity is increased.

In another simulation, we have tried to add random noise (Matlab function *rand*) constrained the maximum amplitude. A third approach is to start with $\bar{\bar{Z}}_{avg}$ and a loss parameter, say $\alpha = 0.01$. Firstly to generate a set of $\bar{\bar{\xi}}$ determined by α based on RMT. Next $\bar{\bar{\xi}}$ is coupled to $\bar{\bar{Z}}_{avg}$ through the RCM construction $\bar{\bar{Z}}_{cav} = i \cdot Im(\bar{\bar{Z}}_{avg}) + [Re(\bar{\bar{Z}}_{avg})]^{1/2} \cdot \bar{\bar{\xi}} \cdot [Re(\bar{\bar{Z}}_{avg})]^{1/2}$. An ensemble of realizations of $\bar{\bar{Z}}_{cav}$ can be created, and then converted to $\bar{\bar{S}}_{cav}$. Similarly, by adding different amount of noise to $\bar{\bar{S}}_{cav}$, the effect on the statistical properties can be analyzed. This method of simulation gets rid of any experimental restrictions and we can vary

the loss parameter α to observe the effect of noise on the subsequently generated “data” for \bar{S}_{avg} . All these simulations show similar results to that shown in Fig. 4.7. For a low loss system, where $\alpha < 0.1$, the noise can clearly cause a change in the deduced “universal” statistics. The higher the noise level, the larger the fitted loss parameter α for a given amount of loss in the cavity. Hence the statistics do not reflect the properties of the system under test. We conclude that there is a low loss limitation to our nonlinear RCM analysis.

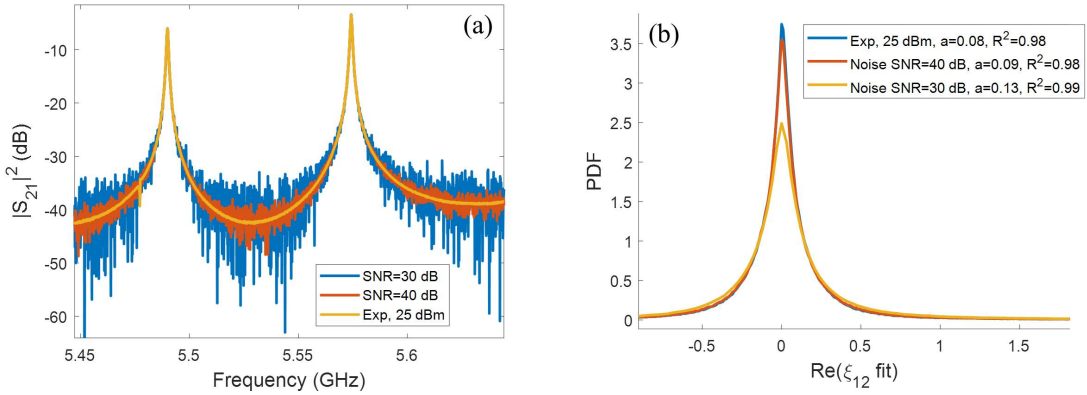


Figure 4.7: (a) Adding white Gaussian noise to measured S_{21} vs. frequency data with different snr . The snr values are 40 dB and 30 dB. (b) Statistics of $Re(\xi_{12})$ in 12~13 GHz and fitted loss parameter α as a result of adding noise.

To explain how the noise plays a role in the RCM analysis, we can take a look at the distributions of $\bar{\xi}$ for small α . As shown in Fig. A.6, for low loss parameter α , the $Re(\xi_{11})$ statistics are distributed in a narrow region just above 0. The distribution has a sharp peak close to 0 for small α . As α increases, the statistics are more widely distributed and centered close to 1. As noise is added, the $Re(\xi_{11})$ statistics change and tend to be more Gaussian-like distributed instead of being narrowly peaked. This in turn causes the fitted α to increase. For the $Im(\xi_{11})$ statistics,

the distribution is widely spread for a low loss system and narrowly focused for a high loss system, all centered at 0. Therefore the noise effect on the statistics is not as prominent on $Im(\xi_{11})$ as that on the $Re(\xi_{11})$ statistics. The properties for the off-diagonal distributions are similar. The $Re(\xi_{21})$ distribution is narrowly focused around 0 and the $Im(\xi_{21})$ statistics are widely distributed for low loss parameter α . Similarly as a result, the statistics of the real part is more susceptible to noise than the imaginary part.

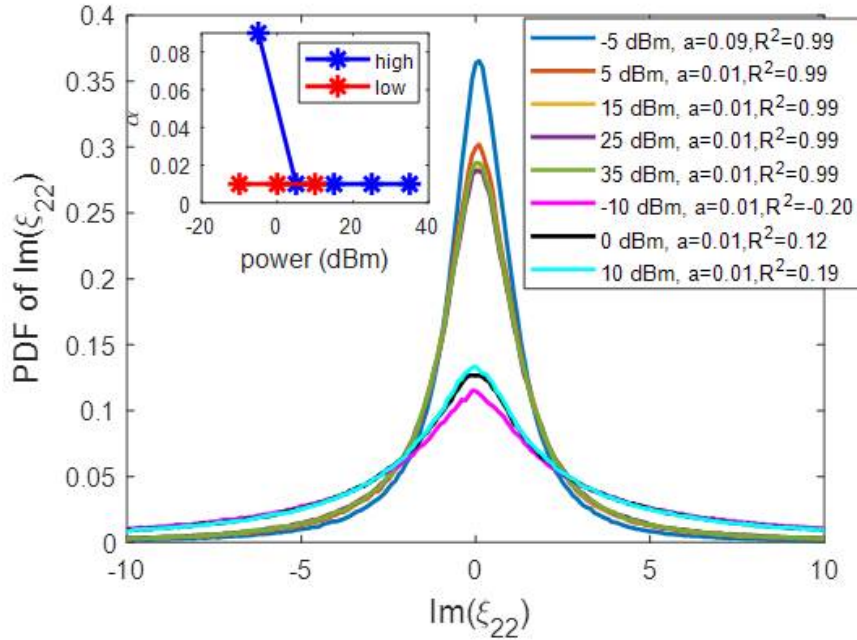


Figure 4.8: $Im(\xi_{22})$ statistics for the 12~13 GHz range of the superconducting Pb cavity at 800 mK for different input powers, including both high power and standard configurations. α is the fitted loss parameter and R^2 is the goodness of fit. The inset shows the fitted loss parameter α vs. the input power, for the high power and low power configurations, respectively.

Fig. 4.9(a) shows the RCM theoretical distributions for low loss parameters $\alpha \leq 0.1$, and compared with the theoretical prediction for zero loss (a Lorentzian [26, 72, 73]). It is predicted that in the low loss limit $\alpha \sim 0$, $Im(\xi_{11})$ tends to be

a Lorentzian distribution with formula $P(x) = \frac{1}{\pi(1+x^2)}$. As seen from Fig. 4.9(a), for $\alpha < 0.1$, the distributions look identical when plotted on a linear scale. The differences among them mainly occur in the long tails. Fig. 4.9(b) shows their differences in the tails if the distributions are plotted on a log scale. The smaller the loss parameter, the distribution spreads over a wider range. Stated another way, the variance of the distribution increases as the loss parameter decreases.

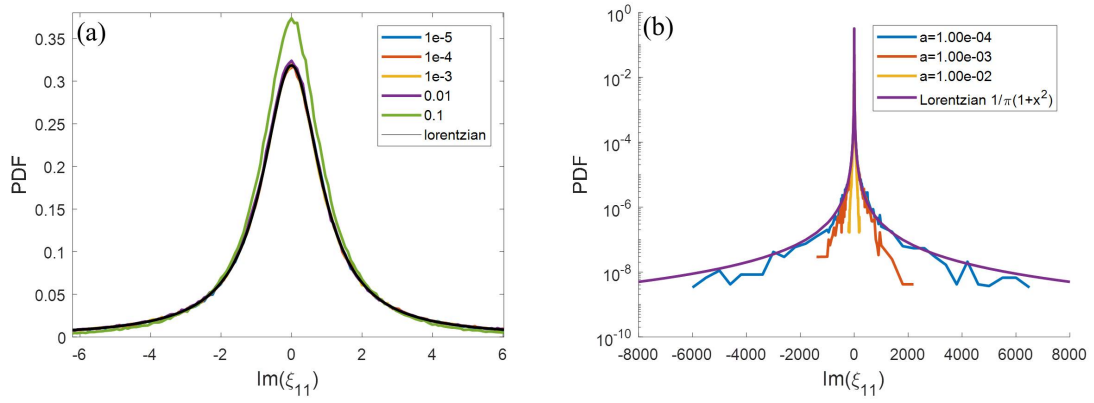


Figure 4.9: RCM predicted $Im(\xi_{11})$ statistics for low loss parameters $\alpha \leq 0.1$. Distributions are plotted in linear scale (a) and log scale (b), and compared with the Lorentzian analytical expression which is expected in the $\alpha = 0$ limit.

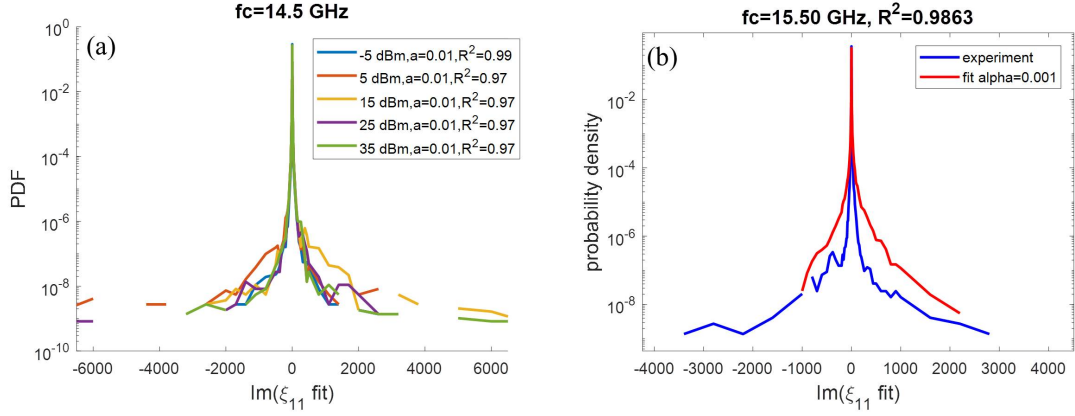


Figure 4.10: (a) Experimental statistics of $\text{Im}(\xi_{11})$ of the superconducting Pb cavity at 800 mK for the 14~15 GHz range for different input powers, plotted in log scale. (b) A best fit to the tail of $\text{Im}(\xi_{11})$ at $P_{in} = 35$ dBm showing the loss parameter α is on the order of 10^{-3} .

Due to the noise (as discussed above), the imaginary statistics tend to give a smaller loss parameter from the billiard data. In order to properly find α , we need to see the long-tail distributions of $\text{Im}(\xi)$. Fig. 4.10(a) shows the experimental results of the statistics of $\text{Im}(\xi_{11})$ in the 14~15 GHz range for input powers in the high power configuration. As the power increases, the tails tend to be longer, i.e. the distribution is more widely distributed. The distribution of $\text{Im}(\xi_{11})$ can spread up to normalized values of 6000. Compared with the theoretical distribution shown in Fig. 4.9(b), the loss parameter could be as low as 10^{-4} . Fig. 4.10(b) shows a best fit to the statistics in the 15~16 GHz range. The best fit gives $\alpha \sim 10^{-3}$. However, the tails of the blue curve clearly stretch out further than the fit (red). If we calculate the variance σ^2 of the distribution, and assume $\alpha = 1/(\pi\sigma^2)$, then the resulting $\alpha \sim 0.0003$. Thus there is no definitive conclusion of what the real α is.

4.1.3 Further Discussion

From Fig. 4.6, One can see that the statistics measured with the standard configuration give smaller loss parameter than those measured with the high power configuration. This indicates that the new VNA in standard configuration has lower noise and larger SNR. Fig. A.6 shows that from the $Im(\xi_{11})$ statistics, the lower the α , the lower the maximum height in the distribution (which occurs at $Im(\xi_{11}) = 0$), until it approaches $1/\pi = 0.318$ as $\alpha \rightarrow 0$. This means that the PDF at $Im(\xi_{11}) = 0$ should not decrease lower than 0.318. However, the distributions of $Im(\xi_{11})$ shown in Fig. 4.8 have maximum height around 0.18 for the standard configuration data sets. This appears to be unphysical and results in very poor fittings with low R^2 .

We did a series of simulations and RCM analysis to get a deeper understanding of the statistical properties of low-loss billiards. We start with a S_{avg} from experiment, and transform it to Z_{avg} . For $\alpha = 0.1, 0.01, 0.001, 0.0001$, an ensemble of 120 realizations of ξ are generated from RMT, respectively. As before, an ensemble of Z_{cav} and S_{cav} are simulated accordingly. Then from Z_{cav} , if we apply RCM to get the normalized impedance ξ , the statistics of $Re(\xi_{11})$ and $Im(\xi_{11})$ are shown in Fig. 4.11. We find, as in the experiment, the smaller the α , the worse the fitting. Also note that for the $Im(\xi_{11})$ distributions, the lower its peak value at $Im(\xi_{11}) = 0$ as α decreases. One possible reason is that the smaller the α , the more widely distributed the $Im(\xi)$, and a much larger ensemble of statistics with good accuracy is required to generate good statistics. This simulation might help to explain the unphysical results observed for the statistics of $Im(\xi_{11})$ at powers -10, 0, and 10 dBm.

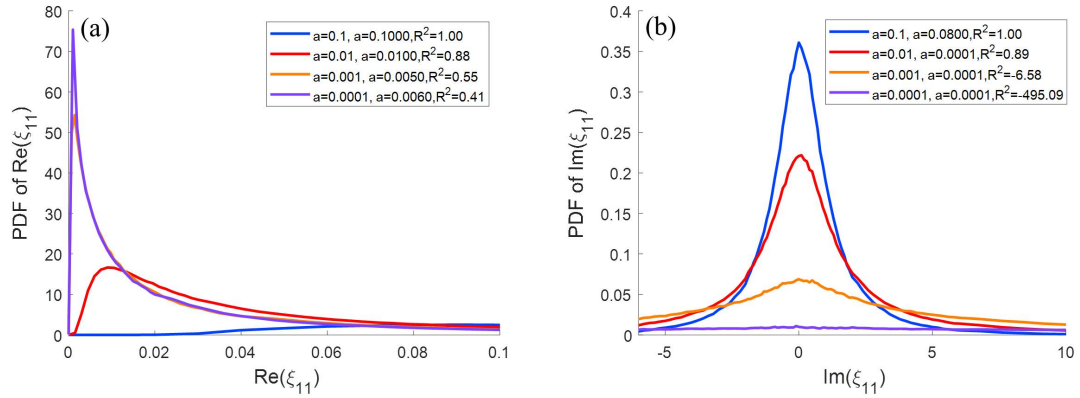


Figure 4.11: A simulation of 120 realizations starting with S_{avg} and different loss parameters. Then RCM is applied to get: (a) Statistics of $Re(\xi_{11})$. (b) Statistics of $Im(\xi_{11})$.

As mentioned in the above discussion, there is an inconsistency of the fitted loss parameter α between the statistics of $Re(\xi)$ and $Im(\xi)$, shown in Fig. 4.6 and Fig. 4.8. We find that this result is prevalent in this billiard. We find that the fitted loss parameter from the $Im(\xi)$ statistics is always smaller than that from the $Re(\xi)$ statistics. We have tested the results in many configurations. For example, we have directly connected the VNA to the billiard at room temperature, which eliminates the transmission lines in the fridge and the TRL calibration. We have investigated whether it is because the perturber is localized in one position, so that the perturbation is not good enough, or that the port is too close to the edge of the billiard. To find the answer, we created a CST model (Fig. 4.12(a)) to get large ensembles of statistics. The port positions have been changed and the two perturbers are allowed to move all around the billiard. Fig. 4.12(b) shows the results of the fitted α from $Re(\xi_{12})$ and $Im(\xi_{12})$ statistics for an ensemble of 99 realizations. α is determined from the largest R^2 which is best fit to the PDF. The

error bar is determined by the change in fitted α that results in a 0.005 change from the best fit R^2 . Note that the error bar in $Im(\xi)$ is much larger than that in $Re(\xi)$. This also shows that in the low loss region, the PDF of $Re(\xi)$ changes more quickly than $Im(\xi)$, hence it is more susceptible to noise. The discrepancy at low frequencies in Fig. 4.12(b) can be understood from the fact that the mode density is low and the wavelength is becoming comparable to the billiard dimension, thus the statistics are not good. In the high frequency end, the loss parameters tend to agree with each other considering the uncertainty. Overall, there is a tendency for fit α from $Re(\xi_{12})$ statistics are larger than that from $Im(\xi_{12})$ statistics. These numerical results are qualitatively similar to the experimental results, confirming our suspicions that noise is playing a dominant role in our data analysis for this nonlinear billiard.

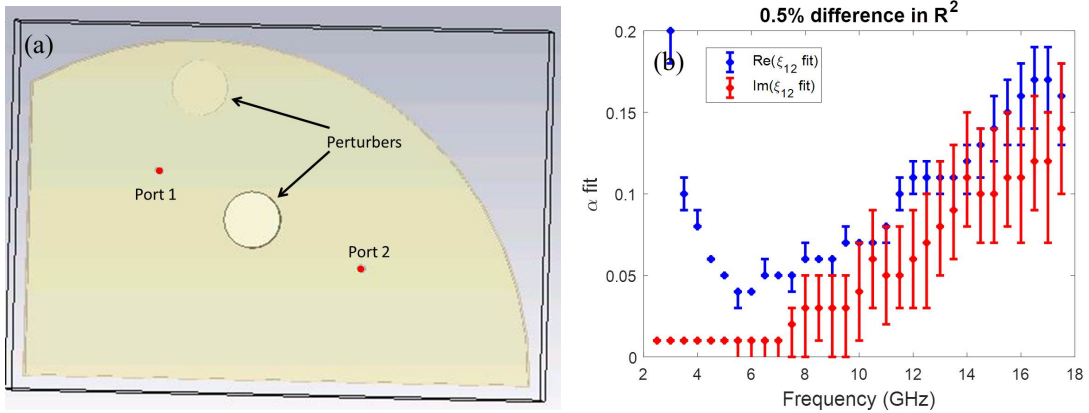


Figure 4.12: (a) A CST model of the cut-circle billiard. The loss parameter of the billiard can be tuned by changing the conductivity of the metal walls. (b) The fitted loss parameter from $Re(\xi_{12})$ statistics compared with that from $Im(\xi_{12})$ statistics.

4.1.4 Conclusion

We have shown that by putting a Pb coated cut-circle billiard into the dilution refrigerator we have achieved a base temperature down to 500 mK and created ensembles of realizations at 800 mK to 1 K with input powers up to 35 dBm. With a cryogenic motor, we are able to make the perturbation more automatic and more systematic. We have used two vector network analyzers to measure the S-parameters at different powers. One implements with high power option that measures S-parameter from -5 to +35 dBm. One is in a standard configuration that measures between -10 to +10 dBm. We have shown that the billiard is in the superconducting state and observed that the measured S-parameters are power dependent.

From a single realization result, the data shows that the Pb billiard mainly shows nonlinear resistance. The resonant peak in the S-parameters decreases as the input power increases and there is virtually no shift of the resonance frequency with power. As power increases, more circulating energy gets into the billiard. This causes a nonlinear change in the surface impedance $Z_S = R_S + iX_S$. We observe that mainly the resistance R_S increases, and as a result, the resonance in the S-parameters decreases. Equivalently, the quality factor Q of the billiard decreases with increasing power. The quality factor Q can also be calculated from the decay time of the Fourier transform of the S-parameters. It shows that Q is around 6000 and decreases by around 100 as the input power increases by 10 dBm.

We are interested in the statistics of this nonlinear billiard. From Fig. 4.5(b),

we see that $Q \sim 6000$ and for $\Delta Q \sim 100$, we can make an estimation of the change in α from the equation $\alpha = k^2 A / (4\pi Q)$. We expect $d\alpha = -\frac{k^2 A}{4\pi Q^2} dQ = -\frac{\alpha}{Q} dQ$ or $d\alpha/\alpha = -dQ/Q$. For $Q = 6000$, $A = 0.0409 \text{ m}^2$, $f = 10 \text{ GHz}$, with $k = 2\pi f/c$, we can estimate $\alpha = 0.024$. We expect that for a decrease of quality factor $dQ = 100$ would result in an increase of loss parameter $d\alpha = 4 \times 10^{-4}$, which is a $\sim 1.6\%$ change in α . Such a small change will be hardly seen in the statistics. However, it turns out that the statistics change in a different direction from the Q . As the input power increases, the loss parameter α obtained by fitting to the normalized impedance statistics decreases. We found the reason to be the noise in the measurement setup. The signal-to-noise ratio of the S-parameter measurements decreases as power decreases. In such a low loss limit, the resulting noisy statistics change in a way that resemble a higher loss case. We note that the statistics of the real part of ξ are more susceptible to noise as the distribution is more sensitive to α than that of the imaginary ξ statistics. It is very difficult to accurately determine the loss parameter of the low loss system as it requires a measurement setup with large dynamic range and it also requires a very large and high quality ensemble of data.

σ^2 is sensitive to small changes in α at low α since $\sigma^2 \sim 1/\alpha$. But good measurement of σ^2 requires very good statistics of the ξ distribution. This requires very good calibration in the limit where $|S| \rightarrow 1$ (i.e. for very large fluctuating values of the impedance). To improve the results, as mentioned in Appendix C, the attenuation of the external attenuators can be decreased a little bit. For the PNA, the IF filter bandwidth can be decreased in order to increase the signal-to-noise

ratio of the S-parameter measurement, although as a result, the sweeping time will increase. However these measures only yield limited improvement. Furthermore, the trade-off among measurement time, heating effects, and noise effects need to be considered.

4.2 TiN on Si Wafer Cut-Circle Microwave Billiard

Kinetic inductance comes from the inertia of the superconducting electrons making up the rf current in the material. It is different from geometrical inductance which comes from the inertia of magnetic field lines created by a current. From the review written by Jonas Zmuidzinas [76], we get the idea that Kinetic inductance can be made to change value substantially when a dc/ac current is passed through the superconductor, without changing the losses at all. They can grow TiN superconducting films on Si wafers. The TiN material has very large kinetic inductance and has a strong nonlinear reactance. Based on this, we proposed to create a chaotic cavity with a TiN on Si wafer like the cut circle cavity. The two superconducting films make a parallel plate resonator, assuming the open edges do not radiate too much. We can excite it from the edge at two ports. We then slice off a section of the wafer to make it a cut circle billiard. The chaotic property of a circular billiard with a straight cut has been discussed in [96]. The combination of wave chaos and nonlinearity of the superconductor will make it interesting to both communities. A series of finite-element numerical simulations are made to verify this idea.

4.2.1 Simulations of the TiN Cut-circle Billiard In CST

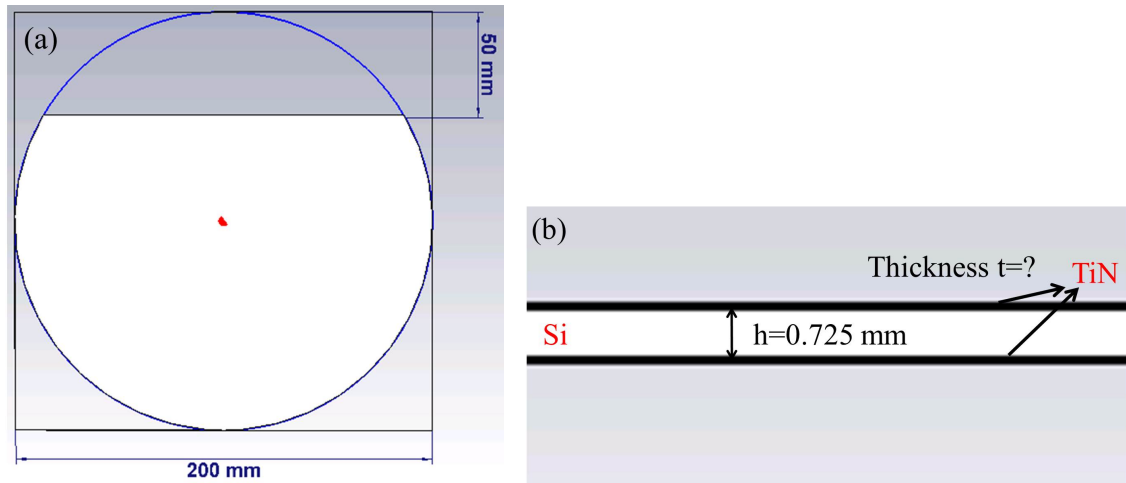


Figure 4.13: Dimensions of the proposed billiard. (a) Top view: the Si wafer has a diameter of $D=200$ mm. A straight cut of 50 mm wide is made from the edge. (b) Cross-sectional view (not to scale): TiN is coated on both top and bottom of the Si wafer. The thickness of the Si wafer is $h=0.725$ mm. The thickness of the TiN has not been decided yet and needs further discussion.

The dimensions of the proposed billiard are shown in Fig. 4.13. The Si wafer has a standard dimension of diameter $D = 200$ mm and thickness $h = 0.725$ mm. A 50 mm wide part is cut away from the edge to make it a cut-circle ray-chaotic billiard (white area in Fig. 4.13(a)). It can be cut by any amount between 0 and $R = 100$ mm [96], for any crystal direction that is convenient. TiN will be coated on top and bottom of the Si wafer, and the edges will be left un-coated. The thickness of the TiN has not been decided and needs more discussion due to our limited experience with this material. The sample needs to have high kinetic inductance and strong (mainly) inductive nonlinearity at high rf current density, while having minimal resistive nonlinearity at the same time.

4.2.1.1 Eigen Modes of the TiN Cut-circle Billiard

Consider a billiard with walls in the shape of a cut circle. All orbits of a Newtonian particle placed in such a billiard will be classically chaotic [96, 97]. We are interested in the wave properties of such billiards in the short wavelength limit, which is the regime of wave chaos. To verify that the cut-circle Si wafer billiard can be used in our setup, the first question is its resonance frequencies and eigen modes. We normally operate in the range of less than 20 GHz. Si has a dielectric constant of $\epsilon_r = 11.9$. The wavelength would be reduced by a factor of $\sqrt{11.9} = 3.45$ compared to free space. A Si wafer normally has thickness in the range of less than 1 mm. By choosing a $D = 200$ mm diameter Si wafer with thickness of $h = 725 \mu\text{m}$, the fundamental resonant mode is approximately at $f_1 = \frac{c}{D\sqrt{\epsilon}} = 433$ MHz, and the cut-off frequency for higher order modes is at $f_c = \frac{c}{2h\sqrt{\epsilon}} = 60$ GHz.

Fig. 4.14(a) is a CST model made by cutting 50 mm away from a Si wafer with top and bottom coated with PEC (perfect electrical conductor) material, and the edges open. Two antennas are around 1 mm away from its edge to couple microwave signal into the cavity. This configuration was shown to have good coupling for a parallel plate resonator [98]. Fig. 4.14(c) shows the results of the S-parameters which demonstrate good coupling between the antenna and the billiard. And by looking at the electric field distribution, we see that the microwave signal is indeed coupling into the Si wafer (and not simply propagating on the outer surfaces). The resonant peaks in S_{21} should correspond to the eigen modes of the Si wafer. Fig. 4.15(a) shows a zoomed-in view of the resonant peaks near 5.9 GHz. The green

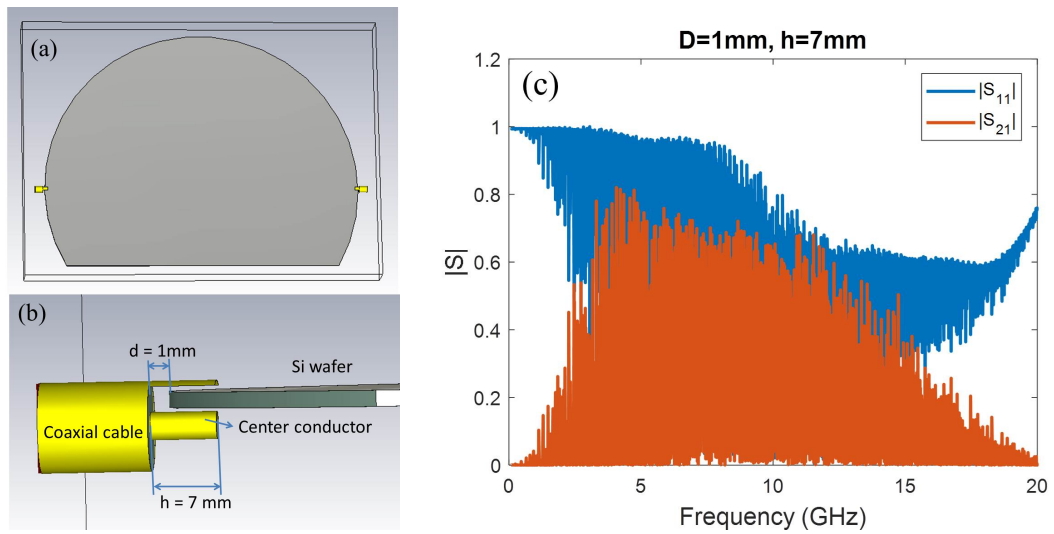


Figure 4.14: (a) 3D model of the TiN on Si cut-circle billiard with two antenna ports to couple signals in/out of the resonator. (b) A detailed view of how the antenna couples to the billiard. (c) Simulated S-parameters of the configuration with antenna to cut-circle edge distance $d = 1$ mm and antenna center pin length $h = 7$ mm.

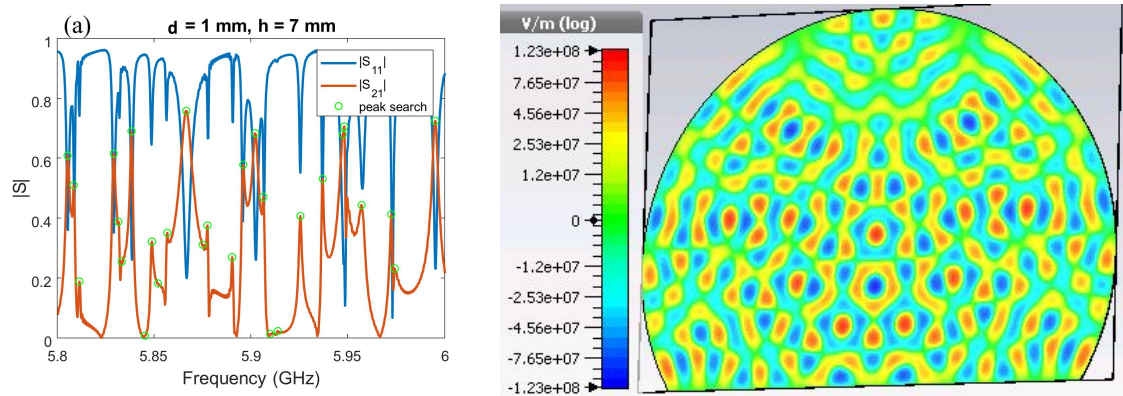


Figure 4.15: (a) A detailed view of the S-parameters near 5.9 GHz, search S_{21} peaks as the eigen frequencies, excluding wiggles caused by finite time truncation of the signal. (b) Field distribution for the 495th eigen mode at frequency 7.026 GHz

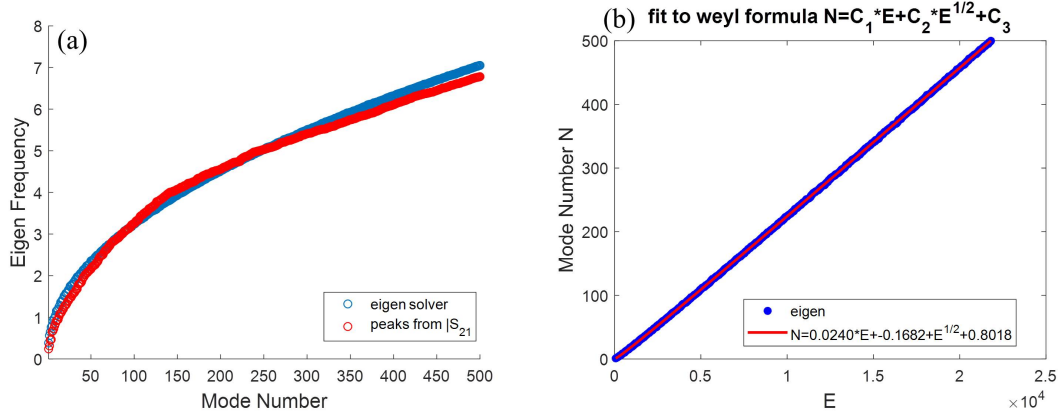


Figure 4.16: (a) The mode frequencies found from S_{21} peaks, compared with the first 500 eigenmodes solved for the closed Si wafer cut-circle. (b) Eigen mode frequencies fit to Weyl formula.

circles are the results of searching for the resonant frequencies, neglecting small wiggles caused by finite time truncation in the simulation. The first 500 modes of the closed billiard are solved in the eigen solver. Fig. 4.15(b) shows the electric field distribution for the 495th eigen mode at 7.026 GHz. Fig. 4.16(a) shows the comparison of the calculated eigen modes with the S_{21} resonant peak frequencies. They have relatively good agreement. The number of “energy levels” N with energy less than $E \sim k^2 = (2\pi f/c)^2$ in a two-dimensional billiard and is given by the Weyl formula $N(E) = C_1 * E + C_2 * E^{1/2} + C_3$, where $C_1 = A/4\pi$, $C_2 = -L/4\pi$, and A is the cross-sectional area of the cavity and L is the perimeter of the cavity. For our Si cut-circle billiard, $A = 0.011 \text{ m}^2$, $L = 0.3826 \text{ m}$. By fitting the first 500 eigen modes to the Weyl formula as shown in Fig. 4.16(b), it is estimated that there are $\sim 37,729$ modes below the cut-off frequency $f_c = 60 \text{ GHz}$.

4.2.1.2 Perturbation

We expect to observe several kinds of nonlinearity in this billiard. The first is that the kinetic inductance of the TiN films will be strongly temperature dependent. For TiN film thickness smaller than the magnetic penetration depth λ , the temperature dependent kinetic inductance will scale as $L_k(T) \sim \lambda^2(T)$ and diverge as the transition temperature T_c is approached from below. This will result in a resonant frequency shift downwards since each resonant mode has a resonant frequency $f_0(T) \sim 1/\sqrt{L_k(T)}$. All of the modes of the TiN resonator will shift considerably with temperature, and this will constitute a global and fairly uniform perturbation to the system. The second source of nonlinearity is that the kinetic inductance is also a function of rf current flowing in the TiN. When rf signals are excited in the billiard, in places where the currents are high, the surface reactance will change considerably, whereas in places where the rf current is low there will be almost no change in reactance. This nonlinearity will be different for each mode. This is a very inhomogeneous and non-uniform perturbation. Lastly, we can create a scanned laser probe that locally heats the TiN to elevated temperatures closer to T_c . This will create a “bubble” of enhanced kinetic inductance and therefore also enhanced surface reactance, with minimal change in resistance. We can scan this hot-spot to perturb many modes of the TiN wafer resonator.

To get statistical results from the chaotic cavity experiment, proper perturbation is required to create ensemble realizations. “Proper” means that among realizations, the detailed configuration has been changed but the volume of the bil-

billiard remains the same (to maintain the same mean mode spacing). Since the Si wafer is a solid medium, we can not put perturbers inside the billiard in the conventional way. We have come up with two possible methods: the laser scanning perturbation or the mechanical deformation perturbation. The experiments will be done in the pulsed tube refrigerator (base $T \sim 5$ K) or the dilution refrigerator (base $T \sim 30$ mK). Since we are interested in the nonlinear properties of the billiard, the ensemble of data will be taken at different excitation powers. We have upgraded the Keysight Vector Network Analyzer N5242A with the high power option which enables power output up to $\sim +40$ dBm. Then the RCM approach will be applied to analyze the statistics at different excitation powers. We hope to uncover either universal or nonuniversal statistical features of this nonlinear wave chaotic system and compare with other nonlinear wave chaotic systems as well. The simulation results and detailed experimental procedures for each perturbation method are discussed below.

A. Laser Shining Perturbation

One way to do the perturbation is to shine a laser spot on the TiN films. This 638 nm laser beam will cause de-pairing and locally heat the sample. We already have the setup to do laser scanning microscopy (LSM) experiments in the dilution refrigerator. The adaptation to the Si wafer will be relatively straightforward. The laser spot size can be controlled from 20 μm diameter to several mm or above. The power can be controlled from 20 μW to 5 mW. A circular region on the wafer will be heated by the laser and thus the TiN surface impedance will be changed locally. It may be possible to briefly make a region of the film become normal. Since the

TiN films have a strongly nonlinear reactance, we have simulated the S-parameters for different reactance values of a circular spot on the TiN surface.

Here is a rough estimate of the reactance change caused by the laser heating. Mattis Bardeen theory gives $L_k(0) = \frac{\hbar R_n}{\pi \Delta}$ for a wire with normal state resistance R_n and superconducting gap parameter Δ , whose transverse dimensions are small enough so that the current distribution is approximately uniform. Such conditions can be achieved when the film width and thickness are less than the magnetic penetration depth, which can be in the range of 10s of μm . The kinetic inductance of such a wire is a function of current I flowing through the wire, $L_k(I) = L_k(0)[1 + (I/I_*)^2]$ for $I/I_* \ll 1$, where I_* is on the order of the critical current of the wire. Note that $I_*^2 \sim 1/R_n$. The magnitude of the Kerr effect (i.e. the nonlinearity) is enhanced in films with high normal state resistivity ρ_n owing both to large kinetic inductance fraction α and small I_* . This implies that the maximum nonlinear inductance will be achieved with films that have the highest normal state resistivity.

The TiN films have thicknesses t ranging from 20 nm to 100 nm and T_c values ranging from 0.7 K and 4.5 K. The normal state resistivity of the film is typically $\rho_n = 100 \mu\Omega - cm$, and a positive residual resistance ratio (RRR), $\frac{\rho_n(300K)}{\rho_n(4K)} \approx 1.1$. Assuming $t=20$ nm, $R_n = \rho_n/t = 50 \Omega/sq$. One has $L_k(0) = \frac{\hbar R_n}{\pi \Delta} = 11.35$ pH/sq with $\Delta = 2k_B T_c$. We estimate the reactance change $\delta X = 2\pi f \delta L_k = 0.43 \Omega/sq$ at $f = 5$ GHz, and it will be larger at higher frequencies. Fig. 4.17 shows that due the reactance change from 0.1 Ohm/sq to 10 Ohm/sq, there is a substantial frequency shift of the peaks in S_{12} . We require frequency shift on the order of the mean spacing between modes. This demonstrates that the laser perturbation is a

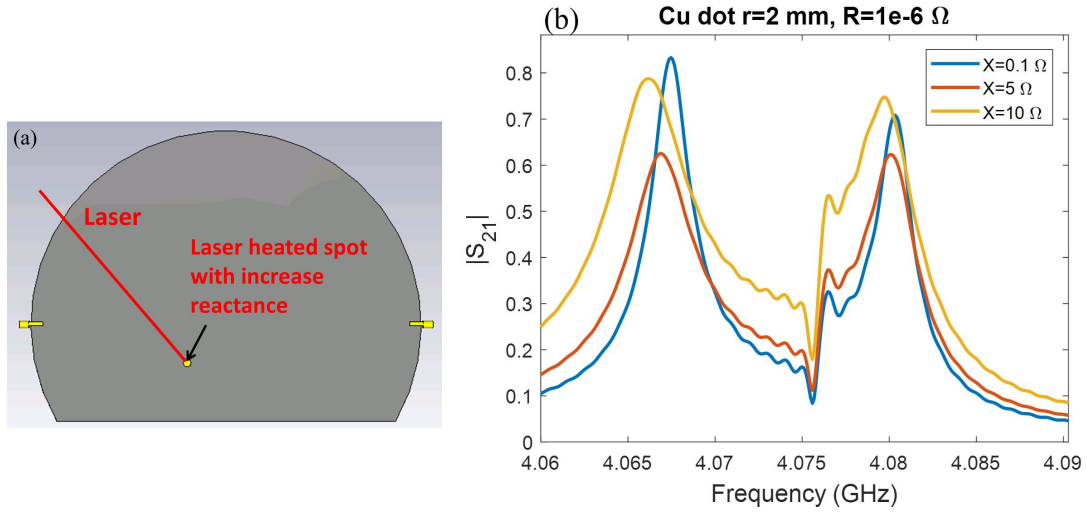


Figure 4.17: (a) Schematic illustration of a laser perturbation on the PEC film with a spot radius of 2 mm. The effect of the laser heating is modeled as changing the reactance of the spot region. (b) Simulated S-parameters as the result of the reactance change. An Ohmic sheet impedance of $Z = R + i * X$ (Ω/sq) is assumed for the spot. The X values are listed in the legend.

promising approach to create ensemble statistics.

B. Mechanical Perturbation

Another way to create a perturbation of the cut-circle eigenmodes is to mechanically deform the Si wafer shape. To do this, we are thinking of attaching a piezo-electric piston to distort the Si wafer. By applying voltage to the piezo, different amounts of force can be applied to the Si wafer to make a mechanical deformation. Fig. 4.18(a) and 4.18(b) shows the deformation of the Si wafer due to a force intensity of 0.2 MPa on a 1 cm diameter circular region. This is equivalent to a 1.6 kg mass on the circular region. The perimeter of the Si wafer is fixed in position. The pictorial view of the displacement in Fig. 4.18(a) has been magnified by a factor of 10 to see the deformation. The actual maximum displacement is ~ 0.5 mm.

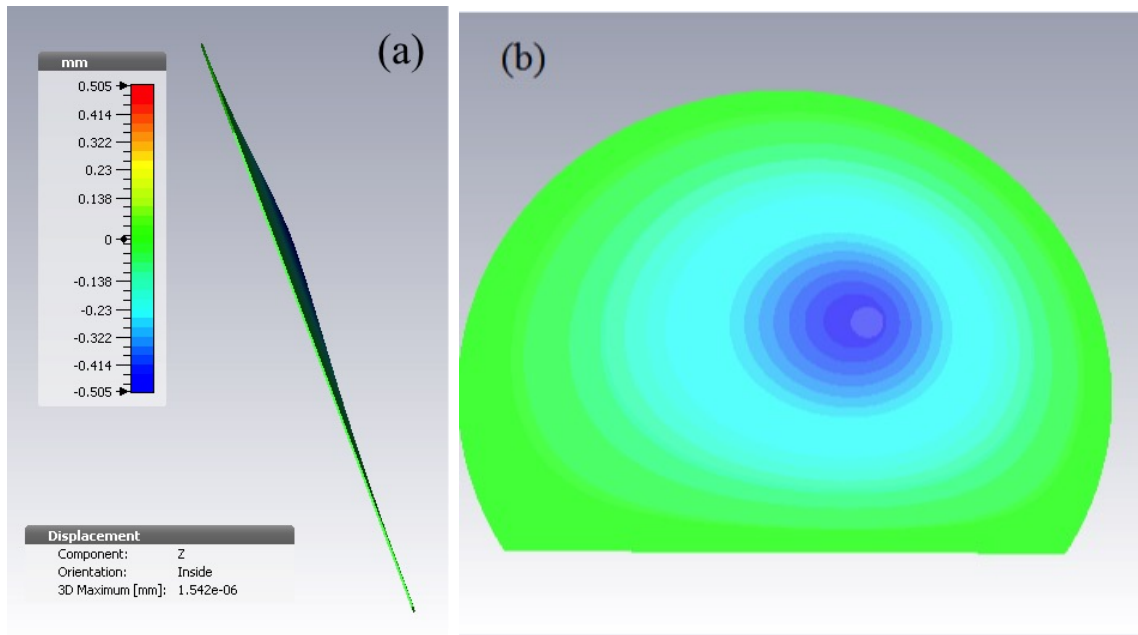


Figure 4.18: Mechanical perturbation (a) cross-section view of the displacement created by a pressure of 0.2 MPa on a circular area of diameter $D = 1$ cm, at the (1,1) inch position from the circular center. The displacement view has been magnified by a factor of 10 to see the deformation. The legend shows the actual displacement. (b) Displacement overview of the deformed wafer.

The largest stress the Si wafer experiences is 0.0439 GPa. Since CST cannot determine whether the material breaks or not, we need to estimate this ourselves. The ultimate tensile strength (or “failure stress”) of a material is the amount of stress that a material can take before breaking. The “yield strength” of a material is the amount of stress that a material can take before it becomes plastically deformed. For silicon, it is assumed that the single crystalline Silicon does not yield until fracture occurs. The fracture strength of silicon given in [99] is 7000 MPa. More practically, the failure stresses are estimated to be in the order of 300 MPa by experience with anisotropically etched diaphragms. Either way, the 43.9 MPa maximum stress on the Si wafer estimated by CST should not break it.

The goal of the mechanical perturbation is to change the eigen modes of the Si wafer. There are two ways to do the simulation of the change in eigenmodes. In CST, the displacement fields from the Mechanical Solver can be imported in to the Eigenmode Solver. A sensitivity analysis will give the change in eigen mode frequency. The sensitivity analysis calculates a local derivative of the eigen modes for small displacements, assuming that the field distribution to be the same between the deformed and undeformed wafer. For the deformation given in Fig. 4.18, the change in mode frequency is on the order of $10^{-3} \sim 10^{-4}$ MHz, while the mode spacing for the eigen modes is ~ 15 MHz. If the force intensity is increased by a factor of 10, the displacements, stress distribution, changes in frequency are all increased by a factor of 10, correspondingly. This appears to be too small to us. Another way to calculate the mode frequency changes due to the deformation is to export the mesh of the deformed shape and solve for the new eigen modes directly.

However, it turns out that there is a bug in CST in that the mesh is not imported with the accuracy necessary for this kind of problem. CST is currently addressing this bug. They have replied that since the deformation is much less than the wavelength, the minute change in the eigenmodes makes sense. The only time the eigenmode would have a significant difference is if the deformation is probably around 20% or so of the wavelength. For a 0.5 mm deformation of the wafer, we would need to measure modes at 35 GHz and higher. Therefore the current hypothesis is either to measure the S-parameters in a higher frequency range or to increase the magnitude of the mechanical deformation. This requires experimental verification.

4.2.2 Preliminary Results on the TiN Cut-circle Billiard

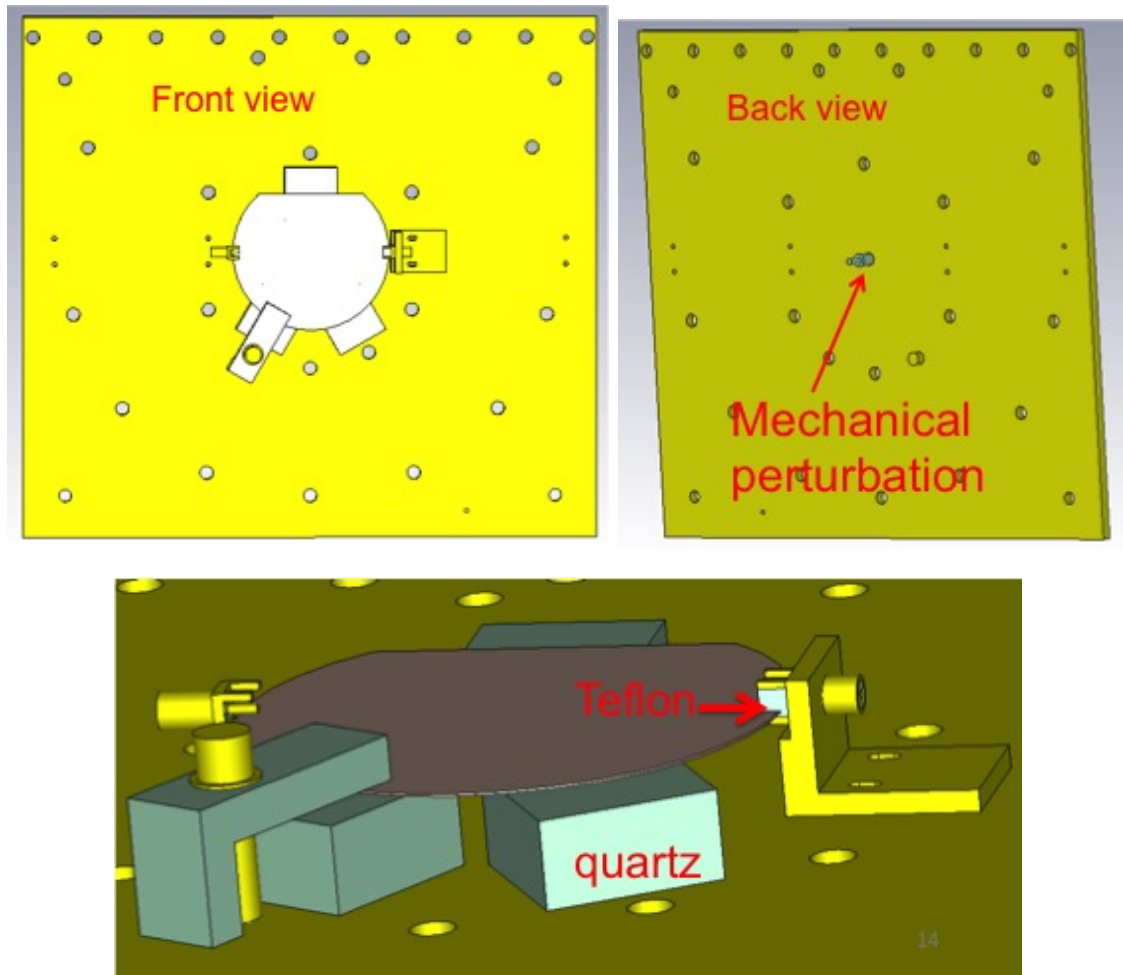


Figure 4.19: (a) Top view of the experiment setup, the Cu plate is made to support different sizes of Si wafer. (b) Back view, a screw made of Teflon or other plastic material is used for mechanical perturbation. (c) Detailed view of the setup, the quartz block is used for mechanical support and thermal conduction. The Teflon block in the SMA connector is used to provide electrical isolation between the wafer and the connector as well as mechanical support to the wafer.

We have designed the experimental setup shown in Fig. 4.19. The design allows for experiments on both 3-in wafers and 7-in wafers. It also allows for both mechanical and laser shining perturbation. The single crystal quartz blocks are used

for mechanical support and thermal coupling. We started testing using Nb on 3-in Si wafers which we can make ourselves. Fig. 4.20 shows the actual experimental setup in the pulsed tube refrigerator. The thermometer is placed on a separate quartz block so that it experiences the same conditions as the wafer.

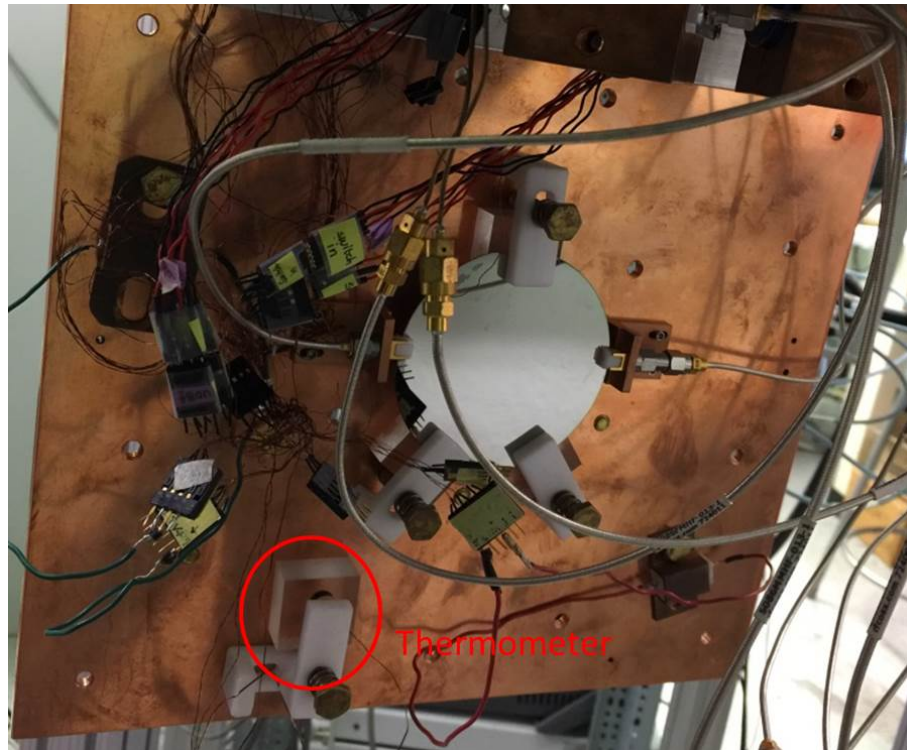


Figure 4.20: Experimental setup in pulsed tube fridge. A test sample of Nb on 3-in Si wafer is used.

We found that the coupling between the antenna and the wafer is poor. So we have tried several approaches to improve the coupling. Firstly, there are a lot of resonances coming from the environment, since the inner can itself is made of metal and can served a 3D chaotic system. To suppress the coupling to the environment, microwave absorbers are covered on the inner can as well as around the launch SMA connector, shown in Fig. 4.21(a) and 4.21(b). Fig. 4.21(c) shows the measured raw

transmission S-parameters S_{12} at room temperature where the resonances from the environment are effectively suppressed. Essentially there is no resonance from the wafer when it is measured at room temperature.

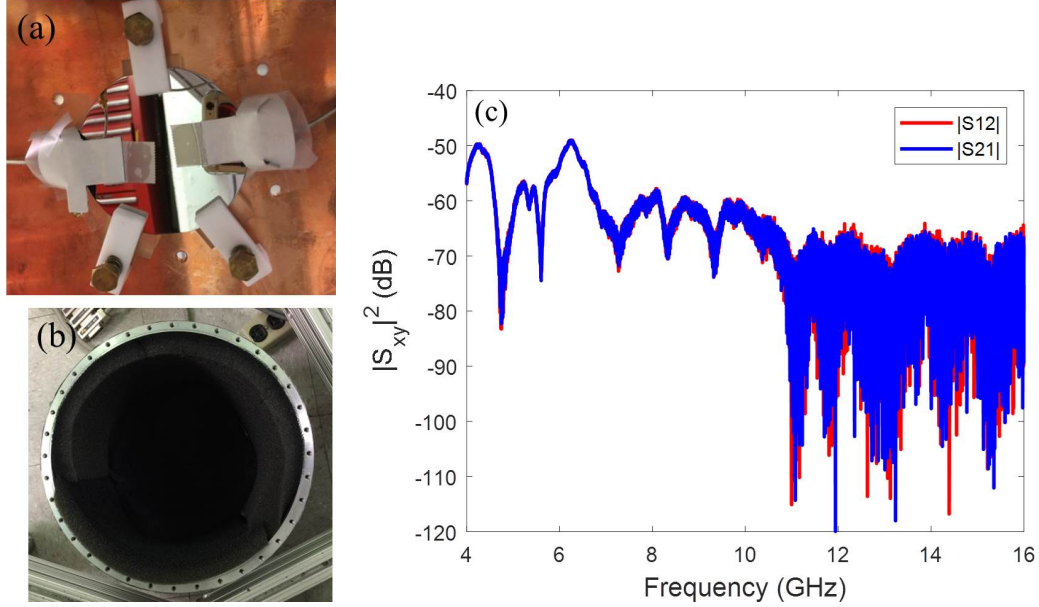


Figure 4.21: (a) Microwave absorbers are covered over the SMA launch connectors. Microwave absorbers are also attached to the copper plate below the wafer. (b) Interior of the can is also covered with microwave absorbers. (c) S_{12} measured at room temperature with microwave absorbers used in (a) and (b).

Good thermal coupling of the wafer is achieved as the base temperature measured on top of the quartz block is 5.8 K. Since we measure S_{12} at different temperatures, shown in Fig. 4.22(a), the change in S_{12} indicates the normal to superconducting transition. We find that the regular set of resonances seen in $S_{12}(f)$ have a period of around $\Delta f = 0.6$ GHz. Equivalently, the length of the (apparently one-dimensional) resonator is $c/(\Delta f \sqrt{\epsilon(Si)}) \sim 16$ cm which is the diameter of the 3 in wafer. It is found the quality factor Q of these resonances is around 70 (the 3 dB bandwidth calculation at 10 GHz gives $Q \sim 67$; and FFT of $|S_{12}(f)|$ gives

$Q \sim 83$), indicating this is a high loss system. We conclude that only the shortest orbits going directly between the excitation and receiving ports through the Si wafer are observed. The Si wafer is undoped and it is reported that the dielectric loss of Si at low temperature is in the order of $\tan\delta \sim 10^{-3}$ [100]. Since the Q values are much less than 10^3 , the experiment shows that the wafer we used is much more lossy. Our next step is to utilize a truly low loss substrate such as sapphire.

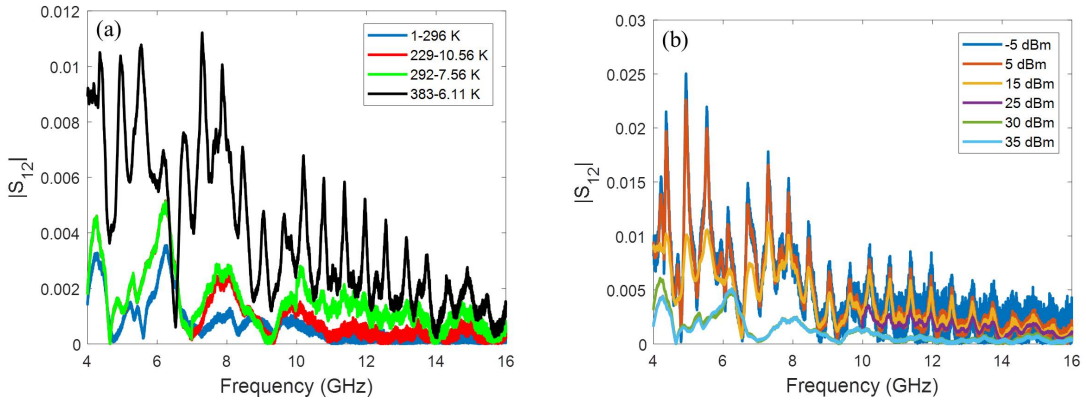


Figure 4.22: Plots of transmission amplitude $|S_{12}|$ vs. frequency. (a) $|S_{12}|$ at different temperatures shows Nb is superconducting at $T = 6.1$ K. (b) $|S_{12}|$ of the Nb two-side coated Si wafer for different input powers at $T = 6.1$ K mainly shows nonlinear resistivity of the Nb.

Fig. 4.22(b) shows the $|S_{12}|$ for different input powers at temperatures below T_c . The results show nonlinear resistance from the Nb films on Si. For this run, to improve the coupling, the SMA connectors are soldered directly to the wafer. Though the contact is not very good due to the difficulty in soldering to the wafer, there is still partial contact, and this creates strong coupling. For high input power, the heating apparently drives Nb to the normal state and S_{12} appears to be the same as that measured in the normal state. To avoid this, the coupling does not need to

be that strong, and the use of the Teflon block in the original design is suggested. The mechanical perturbation is also tested and judged to work.

We received a 30 nm thick TiN film sample on Si wafer from a commercial source. With Chirs Eckberg in Prof. Johnpierre Paglione's group, its superconducting temperature was measured to be 3.7 K in the Physical Property Measurement System (PPMS). This source of TiN looks promising for creating a nonlinear reactive cut-circle resonator. We now need to find the best coupling conditions to observe the thousands of expected modes in this resonator, and to drive them into the nonlinear reactive regime.

4.2.3 Future Work

A list of planned tests on the Nb billiard include:

1. apply our in-situ TRL calibration;
2. measure the loss parameter of the billiard, in the linear response regime;
3. check that the mechanical perturbation achieves a sufficiently strong perturbation. This may require the use of piezo materials;
4. check the effects of laser perturbation when the wafer is cooled in the dilfridge.

When the above prodedures are confirmed, for the TiN billiard, we propose the following measurements and data analysis procedures:

1. Put the billiard into the dilution refrigerator. Measure the transition temperature T_c . It can be found from the sudden change of the S-parameters as a

function of frequency.

2. For $T < T_c$, measure the low power S-parameters. Find the eigen spectrum of the billiard and compare with the Weyl formula.
3. For $T < T_c$, measure the S-parameters at different powers, see how the S-parameters change with power.
4. Measure the S-parameters at different temperatures with low power, both above and below T_c . See how the S-parameters change with temperature.
 - If temperature perturbation is good enough, i.e. frequency shift is comparable with the mean mode spacing, then ensemble statistics can be created by changing the temperature. Such ensembles will also be collected for high rf powers.
5. For laser shining perturbation, gradually increase the laser intensity to see how the S-parameters (for low excitation power) change with laser intensity. Find a laser power that is large enough for the required perturbation.
 - Create ensemble statistics by changing the laser spot position. The ensemble will also be collected for high rf powers.
6. To test the mechanical *fracture stress* at $T < T_c$, several dummy samples are needed. The *fracture stress* might depend on the force position and how the billiard is mounted.

7. For $T < T_c$, gradually increase the mechanical stress. See how the S-parameters (at low excitation power) change.
8. If the mechanical perturbation is good enough, vary the force positions and strength to create the ensemble statistics. The ensemble will also be collected for high rf powers.
9. Once the ensemble data is collected, apply the RCM technique to analyze the data for each power, respectively.
 - First test whether the RCM works for the low power case. Based on the simulation, it should. If not, find the reason and correct it.
 - Apply the RCM to the high power statistics, and see whether and how the statistics change with power: this is our objective with respect to nonlinear statistics! We wish to observe statistical changes with power and explain why they change.
 - We will also simulate the microwave properties of the real device once the TiN film parameters are known.

Chapter 5: Corbino Reflection Technique to Measure Material Microwave Properties

5.1 Experiment Setup

The Corbino reflection technique is a broadband non-resonant experiment at microwave frequencies (from DC - 50 GHz) that measures the reflection of a microwave signal incident on the sample [101–105]. The measurement has a special geometry in which the thin film forms a short circuit between the inner and outer conductors of a coaxial cable as a thin disk (Fig. 5.1), called a Corbino disk [101,102]. It has the advantage that the currents in the film flow in the radial direction, and the magnetic fields produced only exist in the azimuthal direction, thus the edge effects are minimized. This technique is very useful to study the motion of magnetic vortices in superconducting materials where edge contributions are significant [106–109]. It has also been used to measure the shielding effectiveness of carbon nanotube films [77,78]. Under this geometry, the calibrated complex reflection coefficient S_{11} is then measured for the sample. By applying standard transmission line theory, the surface impedance Z_S of the sample can be extracted. We utilize this technique to characterize the room temperature microwave properties of various film materials,

including the reflectivity R_F , transmittance T_F and absorptivity A_F .

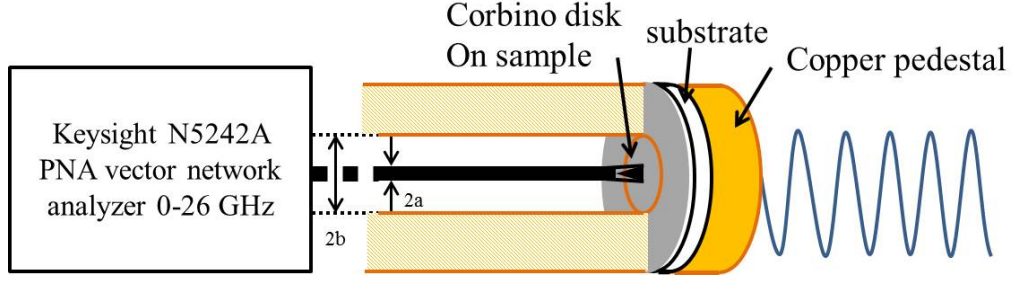


Figure 5.1: Schematic sketch of the Corbino measurement setup. The coaxial cable inner radius is $a = 0.254$ mm; the outer radius $b = 0.84$ mm.

The calibration procedure and data analysis are addressed in Refs. [103, 104].

The measured reflection coefficient S_{11} is related to the load impedance Z_L presented by the sample as:

$$S_{11} = \frac{Z_L - Z_0}{Z_L + Z_0} \quad (5.1)$$

where Z_0 is the characteristic impedance of the coaxial transmission line, typically $Z_0 = 50 \Omega$. The load impedance Z_L is the ratio of the total voltage across the Corbino disk to the total current flowing through the disk. It depends on the geometry of the Corbino disk as well as the properties of the sample. In our experiment, the coaxial cable has an inner radius $a = 0.254$ mm and an outer radius $b = 0.84$ mm. The load impedance Z_L is related to the surface impedance of the thin film Z_S through:

$$Z_L = \Gamma Z_S^{eff}, \quad \Gamma = \frac{1}{2\pi} \ln\left(\frac{b}{a}\right) \quad (5.2)$$

This measured surface impedance is the effective surface impedance of a thin film

on a substrate [4]:

$$Z_S^{eff} = Z_{bulk} \frac{Z_{sub} + Z_{bulk} \tanh(-i\hat{q}t_0)}{Z_{bulk} + Z_{sub} \tanh(-i\hat{q}t_0)} \quad (B.4) \quad (5.3)$$

where $\hat{q} = \frac{\omega}{c} \sqrt{\hat{\epsilon}}$ is the value of the wavevector of the bulk material.

$$\hat{q} = \frac{\omega}{c} \hat{N} = \frac{\omega}{c} \sqrt{\epsilon \mu_1 / \epsilon_0 \mu_0} = \omega \sqrt{\epsilon \mu_1} \quad (5.4)$$

In SI units, Eq. 5.3 should reduce to (if $q = ik$, need to check for i , also check for Eq. (5) in [110]):

$$Z_S^{eff} = Z_{bulk} \frac{Z_{sub} + Z_{bulk} \tanh(kt_0)}{Z_{bulk} + Z_{sub} \tanh(kt_0)} \quad (5.5)$$

where

$$Z_{bulk} = \sqrt{\frac{\mu}{\epsilon}}, \quad k = \omega \sqrt{\mu \epsilon} \quad (5.6)$$

In the case $|kt_0| \gg 1$, then $\tanh(kt_0) \sim 1$, $Z_S^{eff} = Z_{bulk}$. While if $|kt_0| \ll 1$, $\tanh(kt_0) \sim kt_0$,

$$Z_S^{eff} = \frac{(\omega \sqrt{\mu \epsilon} t_0)^{-1} + \frac{\sqrt{\mu/\epsilon}}{Z_{sub}}}{\sqrt{\frac{\epsilon}{\mu}} + \frac{(\omega \sqrt{\mu \epsilon} t_0)^{-1}}{Z_{sub}}} = \frac{1/(kt_0) + Z_{bulk}/Z_{sub}}{1/Z_{bulk} + \frac{1/(kt_0)}{Z_{sub}}} \quad (5.7)$$

in the case of $|Z_{bulk}| \ll |Z_{sub}|$, we can further simplify to

$$Z_S^{eff} \approx \frac{1/(kt_0)}{1/Z_{bulk} + \frac{1/(kt_0)}{Z_{sub}}} = \frac{1}{\omega \epsilon t_0 + \frac{1}{Z_{sub}}} \quad (5.8)$$

5.2 Derivation of R_F , T_F , A_F

1. Obtain ϵ from Z_S^{eff} . For $|kt_0| \gg 1$, $Z_{bulk} = Z_S^{eff} = \sqrt{\frac{\mu}{\epsilon}}$, thus $\epsilon = \mu / (Z_S^{eff})^2$.

For $|kt_0| \ll 1$, from Eq. 5.8:

$$\epsilon \approx \left(\frac{1}{Z_S^{eff}} - \frac{1}{Z_{sub}} \right) / \omega t_0 \quad (5.9)$$

2. Obtain $\sigma = \sigma_1 + i\sigma_2$ from $\varepsilon = \varepsilon_1 + i\varepsilon_2$, refer to Fig. 5.2, and converted to SI units:

$$\sigma_1 = -\omega\varepsilon_2, \quad \sigma_2 = \omega(\varepsilon_1 - \varepsilon_0) \quad (5.10)$$

where $\varepsilon_0 = 8.854 \times 10^{-12} F/m$. Note there is a sign change for σ in Gruner's book, which is not correct for SI units.

3. Get the complex refractive index $N = n + i\kappa$ from ε , similarly, refer to Fig. 5.2. Note that to distinguish $Im\{N\}$ from the complex propagation constant k , differing from Gruner's book, we have used κ to denote the extinction coefficient here.

$$n = \left\{ \frac{\mu_1}{2\mu_0} \left[\left(\frac{\varepsilon_1}{\varepsilon_0} \right)^2 + \left(\frac{\varepsilon_2}{\varepsilon_0} \right)^2 \right]^{1/2} + \frac{\varepsilon_1 \mu_1}{2\varepsilon_0 \mu_0} \right\}^{1/2} \quad (5.11)$$

$$\kappa = \left\{ \frac{\mu_1}{2\mu_0} \left[\left(\frac{\varepsilon_1}{\varepsilon_0} \right)^2 + \left(\frac{\varepsilon_2}{\varepsilon_0} \right)^2 \right]^{1/2} - \frac{\varepsilon_1 \mu_1}{2\varepsilon_0 \mu_0} \right\}^{1/2} \quad (5.12)$$

where $\mu = \mu_1 + i\mu_2$ is the permeability of the material and $\mu_0 = 4\pi \times 10^{-7} \text{ H/m}$.

4. Obtain α (power absorption coefficient with units of m^{-1}), β (an angle indicating the phase change on once passing through the medium of thickness t_0 and refractive index n), ϕ_r (phase shift: the phase difference between the phases of the reflected and the incident waves) from n, κ :

$$\alpha = \frac{2\kappa\omega}{c} = \frac{4\pi\kappa}{\lambda_0} = \frac{4\pi\kappa f}{c} = \frac{\mu_1}{\mu_0} \frac{\sigma_1}{n\varepsilon_0 c} \quad (2.3.18 - 19), \quad (5.13)$$

$$\phi_r = \text{atan}\left(\frac{-2\kappa}{1 - n^2 - \kappa^2}\right) \quad (2.4.14, \text{pg.37}), \quad (5.14)$$

$$\beta = \frac{2\pi n t_0}{\lambda_0} \quad (B.11) \quad (5.15)$$

Here λ_0 is the wavelength in vacuum, $\lambda_0 f = c$, and we have used a result from Fig. 5.2, namely $2n\kappa = \mu_1 \varepsilon_2$ to find that $\kappa = \frac{\mu_1}{\mu_0} \frac{\sigma_1}{2n\omega\varepsilon_0}$ in the last step for the expression of α .

5. Obtain R_F , T_F , A_F from α , β , ϕ_r . For a material with finite thickness t_0 , the reflectivity R_F , transmission T_F and absorptivity A_F of a free-standing film (i.e. no substrate effects included) are as follows.

$$R_F = R \frac{(1 - \exp(-\alpha t_0))^2 + 4\exp(-\alpha t_0)\sin^2\beta}{[1 - R\exp(-\alpha t_0)]^2 + 4R\exp(-\alpha t_0)\sin^2(\beta + \phi_r)} \quad (B.9) \quad (5.16)$$

$$R = \frac{(1 - n)^2 + \kappa^2}{(1 + n)^2 + \kappa^2} \quad (B.10a) \quad (5.17)$$

$$T_F = \frac{[(1 - R)^2 + 4R\sin^2\phi_r]\exp(-\alpha t_0)}{[1 - R\exp(-\alpha t_0)]^2 + 4R\exp(-\alpha t_0)\sin^2(\beta + \phi_r)} \quad (B.12a) \quad (5.18)$$

$$A_F \approx \frac{8\varepsilon_2\pi t_0/\lambda_0}{4 + 8\varepsilon_2\pi/\lambda_0 + (\varepsilon_1^2 + \varepsilon_2^2)4\pi^2 t_0^2/\lambda_0^2} \quad (B.18) \quad (5.19)$$

This is valid for arbitrary thickness t_0 . We should have $R_F + T_F + A_F = 1$. As $t_0 \rightarrow \infty$, $R_F \rightarrow R$. Note Eq. (B.18) for A_F only holds for thin metallic film, which satisfies $\varepsilon_1^2 \ll \varepsilon_2^2$ and $nt_0 \ll \lambda_0$. Otherwise, we can use $A_F = 1 - R_F - T_F$ to get the absorptivity. The shielding effectiveness as a function of frequency for different film thicknesses is calculated through $SE_{tot} = -10\log T$, T is the electromagnetic radiation transmittance, which depends on the complex index of refraction $N = n + i\kappa$ and the bulk reflectivity R . This formula is applicable when the film thickness is much less than the wavelength [77].

On the other hand, for electrically conductive materials, theoretically, the electromagnetic interference shielding effectiveness (EMI SE) can be calculated from the Simon formalism [111],

$$SE(dB) = 50 + 10\log\left(\frac{\sigma}{f}\right) + 1.7t\sqrt{\sigma f} \quad (5.20)$$

where σ [S·cm⁻¹] is the electrical conductivity, f [MHz] is the frequency and t [cm] is the thickness of the shield. Experimentally, EMI SE is measured in decibels [dB]

and defined as the logarithmic ratio of incoming power P_I to transmitted power P_T as $SE(dB) = 10\log(P_I/P_T)$. And the EMI shielding efficiency SE (%) can be converted from the EMI shielding effectiveness (dB) using the equation:

$$SE(\%) = (1 - 10^{-\frac{SE(dB)}{10}}) \times 100 \quad (5.21)$$

The EMI shielding efficiency SE (%) represents the ability of a material to block waves in terms of percentage, which is essentially the complementary of transmittance $1 - T$ in our calculation. We'll compare our approach [5.18](#) with the Simon formalism [5.20](#) for calculation of the shielding effectiveness of conductive materials.

Table 2.1. Relationships between the material parameters and optical constants $\hat{\epsilon}$, $\hat{\sigma}$, and \hat{N} .

The negative sign in the time dependence of the traveling wave $\exp\{-i\omega t\}$ was chosen (cf. Eqs (2.2.14)).

	Dielectric constant $\hat{\epsilon}$	Conductivity $\hat{\sigma}$	Refractive index \hat{N}
$\hat{\epsilon}$	$\hat{\epsilon} = \epsilon_1 + i\epsilon_2$	$\epsilon_1 = 1 - \frac{4\pi\sigma_2}{\omega}$ $\epsilon_2 = \frac{4\pi\sigma_1}{\omega}$	$\epsilon_1 = \frac{n^2 - k^2}{\mu_1}$ $\epsilon_2 = \frac{2nk}{\mu_1}$
$\hat{\sigma}$	$\sigma_1 = \frac{\omega\epsilon_2}{4\pi}$ $\sigma_2 = (1 - \epsilon_1)\frac{\omega}{4\pi}$	$\hat{\sigma} = \sigma_1 + i\sigma_2$	$\sigma_1 = \frac{nk\omega}{2\pi\mu_1}$ $\sigma_2 = \left(1 - \frac{n^2 - k^2}{\mu_1}\right)\frac{\omega}{4\pi}$
\hat{N}	$n = \left\{ \frac{\mu_1}{2} [\epsilon_1^2 + \epsilon_2^2]^{1/2} + \frac{\epsilon_1\mu_1}{2} \right\}^{1/2}$ $k = \left\{ \frac{\mu_1}{2} [\epsilon_1^2 + \epsilon_2^2]^{1/2} - \frac{\epsilon_1\mu_1}{2} \right\}^{1/2}$	$n = \left\{ \frac{\mu_1}{2} \left[\left(1 - \frac{4\pi\sigma_2}{\omega}\right)^2 + \left(\frac{4\pi\sigma_1}{\omega}\right)^2 \right]^{1/2} + \frac{\mu_1}{2} - \frac{2\pi\mu_1\sigma_2}{\omega} \right\}^{1/2}$ $k = \left\{ \frac{\mu_1}{2} \left[\left(1 - \frac{4\pi\sigma_2}{\omega}\right)^2 + \left(\frac{4\pi\sigma_1}{\omega}\right)^2 \right]^{1/2} - \frac{\mu_1}{2} + \frac{2\pi\mu_1\sigma_2}{\omega} \right\}^{1/2}$	$\hat{N} = n + ik$

Figure 5.2: Table 2.1 from ref. [4], note that we have used κ instead of k for the extinction coefficient.

Table G.1. *Conversion table.*

In order to convert the equations in cgs units into those in the SI system, the relevant symbols have to be replaced by the corresponding one on the right hand side of the table.

Quantity	Gaussian (cgs) systems	SI (mks) system
Speed of light	c	$c = \frac{1}{(\epsilon_0 \mu_0)^{1/2}}$
Electric field	\mathbf{E}	$(4\pi \epsilon_0)^{1/2} \mathbf{E}$
Electric displacement	\mathbf{D}	$\left(\frac{4\pi}{\epsilon_0}\right)^{1/2} \mathbf{D}$
Scalar potential	ϕ	$(4\pi \epsilon_0)^{1/2} \phi$
Charge density	ρ	$\frac{1}{(4\pi \epsilon_0)^{1/2}} \rho$
Electric polarization	\mathbf{P}	$\frac{1}{(4\pi \epsilon_0)^{1/2}} \mathbf{P}$
Current density	\mathbf{J}	$\frac{1}{(4\pi \epsilon_0)^{1/2}} \mathbf{J}$
Dielectric constant	$\hat{\epsilon}$	$\frac{\hat{\epsilon}}{\epsilon_0}$
Conductivity	$\hat{\sigma}$	$\frac{\hat{\sigma}}{4\pi \epsilon_0}$
Magnetic field	\mathbf{H}	$(4\pi \mu_0)^{1/2} \mathbf{H}$
Magnetic induction	\mathbf{B}	$\left(\frac{4\pi}{\mu_0}\right)^{1/2} \mathbf{B}$
Vector potential	\mathbf{A}	$\left(\frac{4\pi}{\mu_0}\right)^{1/2} \mathbf{A}$
Magnetization	\mathbf{M}	$\left(\frac{4\pi}{\mu_0}\right)^{1/2} \mathbf{M}$
Permeability	$\hat{\mu}$	$\frac{\hat{\mu}}{\mu_0}$
Impedance	\hat{Z}	$4\pi \epsilon_0 \hat{Z}$
Poynting vector	\mathbf{S}	$\frac{c}{4\pi} \mathbf{S}$
Energy density	u	$4\pi u$

Note: In the case of the electric field \mathbf{E} we must remember to replace $1/4\pi$ by ϵ_0 .

Figure 5.3: Table G.1 from ref. [4].

5.3 Results

We first present the data analysis for good metals whose material properties we are familiar with, then three groups of new materials are measured. Their preliminary properties are given in Table. 5.1, 5.2, and 5.3, respectively.

Table 5.1: Preliminary Examination on Wentao's Samples

No.	property	DC R (Ω)	Thickness (mm)	d/m	$ kt_0 $ vs. 1
1	like fresh wood	>10M	2.61	d	<
2	like carbonized wood	452	2.43	m	<
3	like carbonized wood	320k/-137k	0.8	m	<

Note: 1. DC resistance R is the measured resistance between the inner and outer conductor of the coaxial cable shown in Fig. 5.1; 2. d/m: whether a material is dielectric-like or metal-like is determined by whether it blocks the resonant peak of the substrate or not; 3. $|kt_0|$ vs. 1: compare $|kt_0|$ vs. 1. Since there are different approaches for $|kt_0| \gg 1$ and $|kt_0| \ll 1$, each assumption is taken respectively to begin with, if the final results are consistent with the assumption, $|kt_0|$ vs. 1 relationship is determined.

Table 5.2: Preliminary Examination on Geng's Samples

No.	property	DC R (Ω)	Thickness (mm)	d/m	$ kt_0 $ vs. 1
1	500_2h	1.26M	1.58	d	<
2	600_2h	440k	1.63	d	<
3	700_2h	84	1.81	m	<
4	800_2h	5	1.17	m	\sim
5	1000_2h	3	0.5	not d	>
6	2000_2min	5	0.49	not d	>
7	2000_4min	3	0.69	not d	>
8	2000_6min	4	0.47	not d	>
9	superwood_700_2h	50	1.1	m	<
10	WC_NiO	42	2.88	m	<
11	WC_CoxO	60	2.8	m	<

Table 5.3: Preliminary Examination on Yubing's Samples

No.	property	DC R (Ω)	Thickness (μm)	d/m	$ kt_0 $ vs. 1
1	10%		129	d	<
2	30%		80	d	<
3	50%		110	d	<
4	70%		220	m	\sim
5	90%		384	m	\sim

5.3.1 Ideal measurements for good metal

We first derive the theoretical quantities we expect for good metal, $|\varepsilon_1| \ll |\varepsilon_2|$, $|\sigma_1| \gg |\sigma_2|$, assuming $\sigma = 1/\rho$ are real,

$$Z_{bulk} \sim \sqrt{\frac{i\mu\omega}{\sigma_1}} = \frac{i\mu\omega}{k} = \frac{1+i}{\sigma_1\delta}, \quad k = \sqrt{\frac{i\mu\omega}{\rho}} = \frac{1+i}{\delta} = \sqrt{i\omega\mu_0\sigma_1}, \quad \delta = \sqrt{\frac{2}{\mu\omega\sigma_1}} \quad (5.22)$$

Note that σ and ρ are complex in general. However the expression for the skin depth δ often assumes that σ and ρ are real. So if we consider a copper film with thickness $t_0 = 0.015$ mm, $\rho = 1.68 \times 10^{-8}(\Omega \cdot m)$, $\sigma = 5.96 \times 10^7(S/m)$. We can get Z_{bulk} from Eq. 5.22, and $Z_S^{eff} = Z_{bulk}$ for a good metal. From Eq. 5.2 we can get Z_L and from Eq. 5.1 we can get the expected measured S-parameters.

Then from Z_S^{eff} we can follow the procedures to obtain ε, N and other quantities. Fig. 5.4 and Fig. 5.5 shows the results. We have $|S| \sim 1$ with phase=180° which is like a short circuit. Impedance $Re(Z_S^{eff}) = Im(Z_S^{eff})$ as expected from Eq. 5.22. Conductivity $|\sigma_1| \gg |\sigma_2|$, dielectric constant $|\varepsilon_1| \ll |\varepsilon_2|$, refractive index $n = \kappa$, bulk reflectivity $R \sim 1$ and skin depth $\delta \sim 1 \mu\text{m}$. That all agrees what we are familiar with. And the shielding effectiveness SE calculated from both approaches agrees in general.

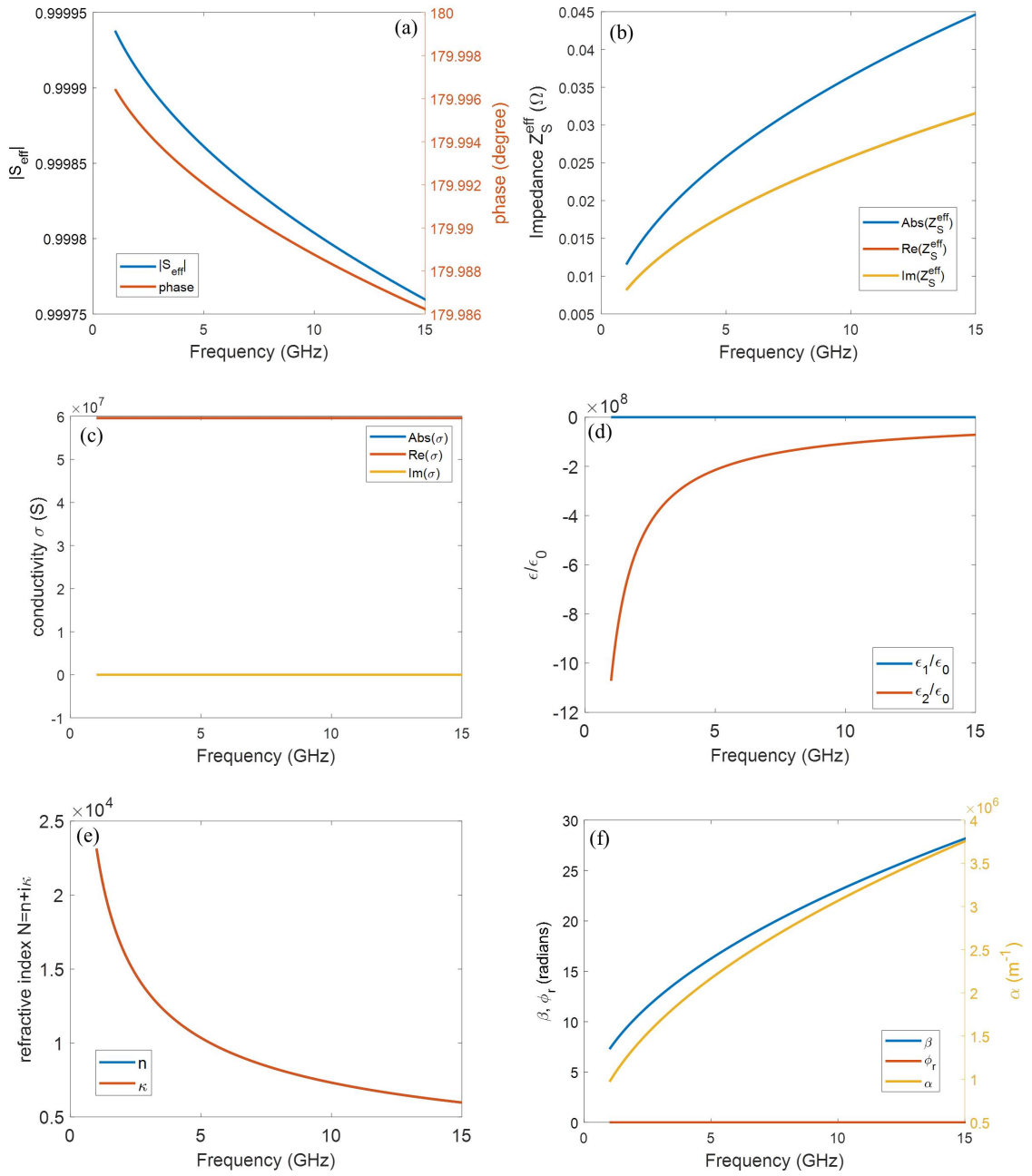


Figure 5.4: Expected measured quantities for a copper film with thickness $t=0.45$ mm $\gg \delta$. (a) S-parameter; (b) Effective impedance Z_S^{eff} ; (c) Complex conductivity σ ; (d) Complex dielectric constant ϵ ; (e) Complex refractive index $N = n + i\kappa$; (f) α, β, ϕ_r .

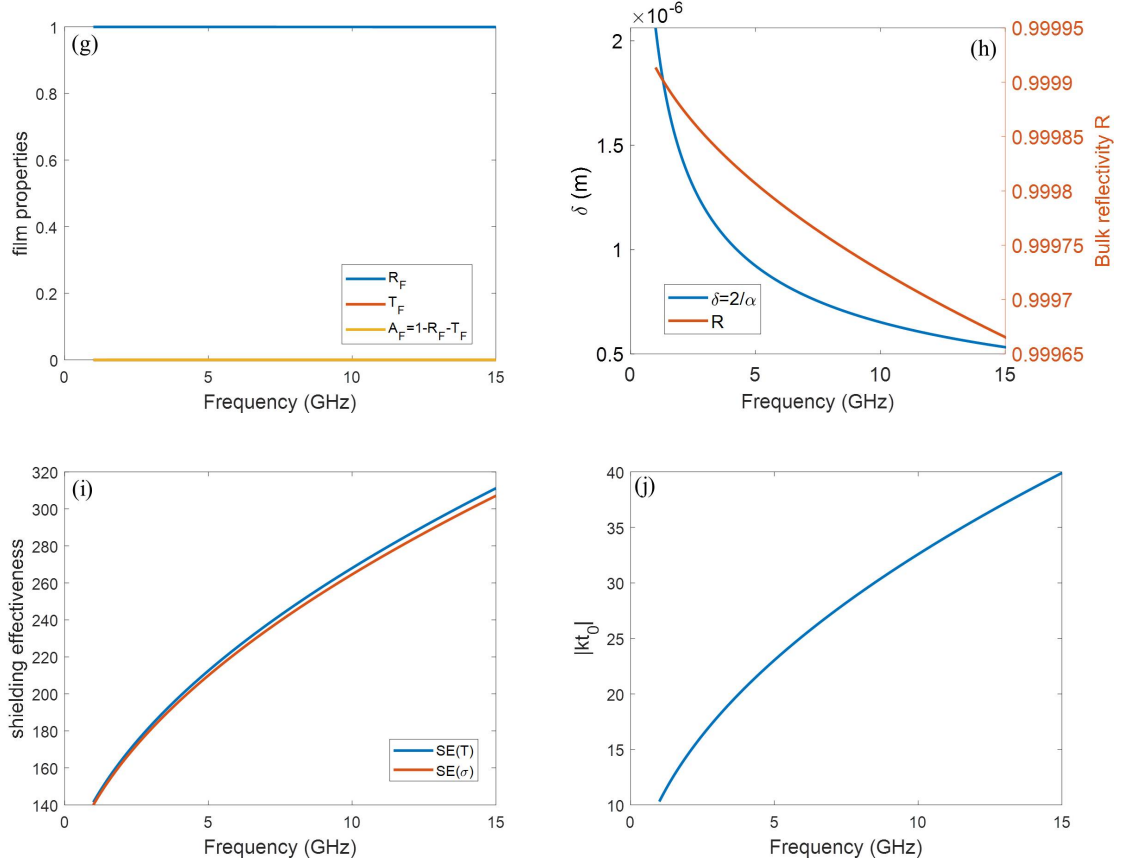


Figure 5.5: Expected measured quantities for a copper film with thickness $t=0.45$ mm $\gg \delta$. (g) R_F, T_F, A_F ; (h) skin depth δ , bulk reflectivity R ; (i) compare shielding effectiveness $SE = \log(T)$ with Simon's formula Eq. 5.20; (j) $|kt_0| \gg 1$, the substrate effect can be neglected.

5.3.2 Measured Al foil

We have measured Al foil on Rohacell substrate, with thickness $t_0 = 0.015$ mm. Though it is good metal, the term $|kt_0| \gg 1$ is not valid, we need to consider the substrate effect, following the procedures in section II. Here we have used Z_{sub} as the the measured impedance directly on the substrate. As will be discussed in the

next section, that is not valid if the sample under study is dielectric-like material. While since $|Z_{bulk}| \ll |Z_{sub}|$, the inaccuracy in Z_{sub} does not affect the qualitative conclusions here. Comparing with the ideal measurement for good metal, the skin depth in Fig. 5.7(b) is much larger than expected. While for a 15 μm thickness Al film, it shouldn't have to consider the substrate effect. The reason is that the S-parameter shown in Fig. 5.6(a) is not close enough to 1, i.e. it is limited by the accuracy of the setup. One of our future efforts is to increase the accuracy of the measurements.

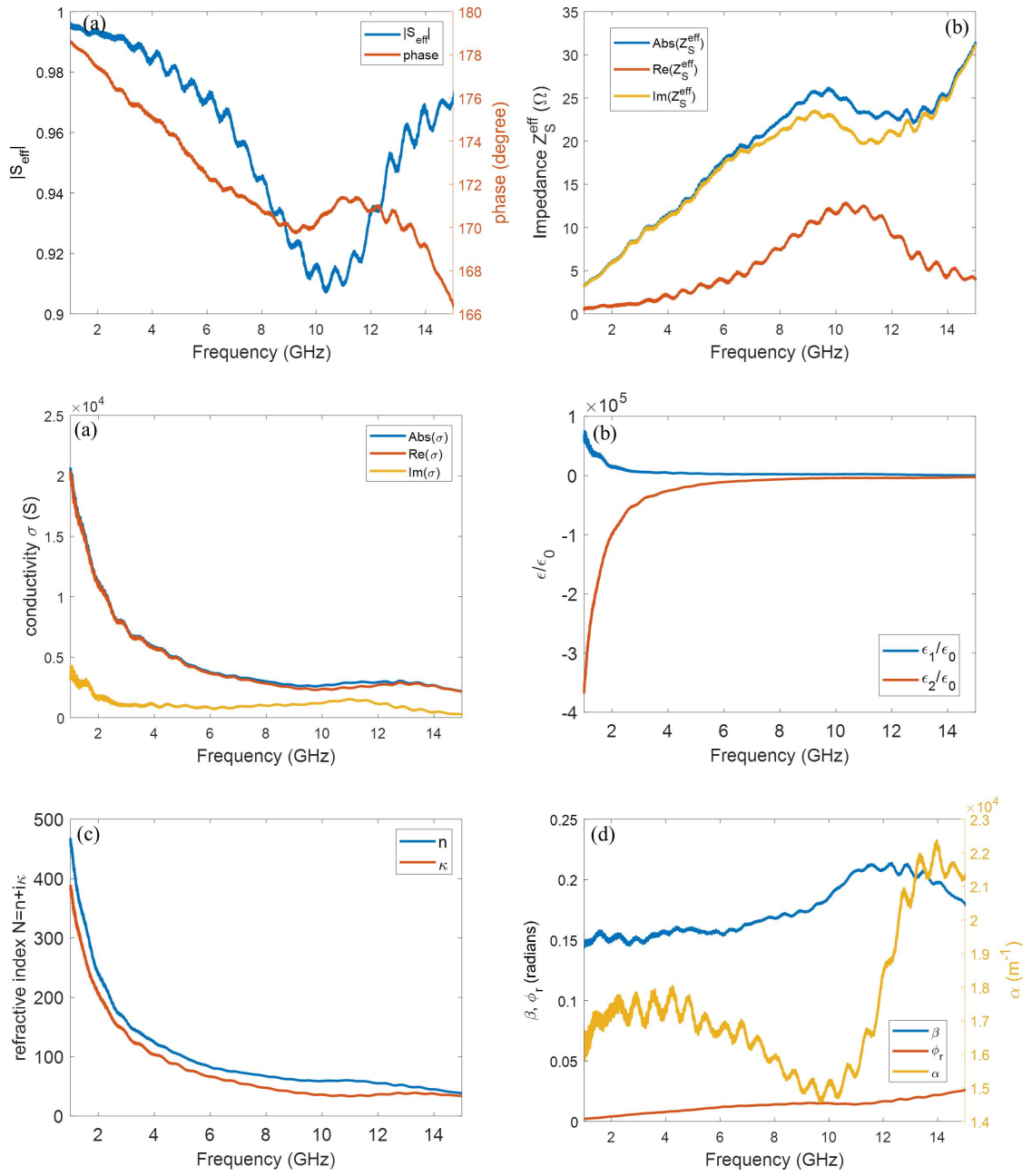


Figure 5.6: Measured quantities for a Al foil with thickness $t=0.015$ mm $< \delta$. (a) S-parameter; (b) Effective impedance Z_S^{eff} ; (c) Complex conductivity σ ; (d) Complex dielectric constant ϵ ; (e) Complex refractive index $N = n + i\kappa$; (f) α, β, ϕ_r .

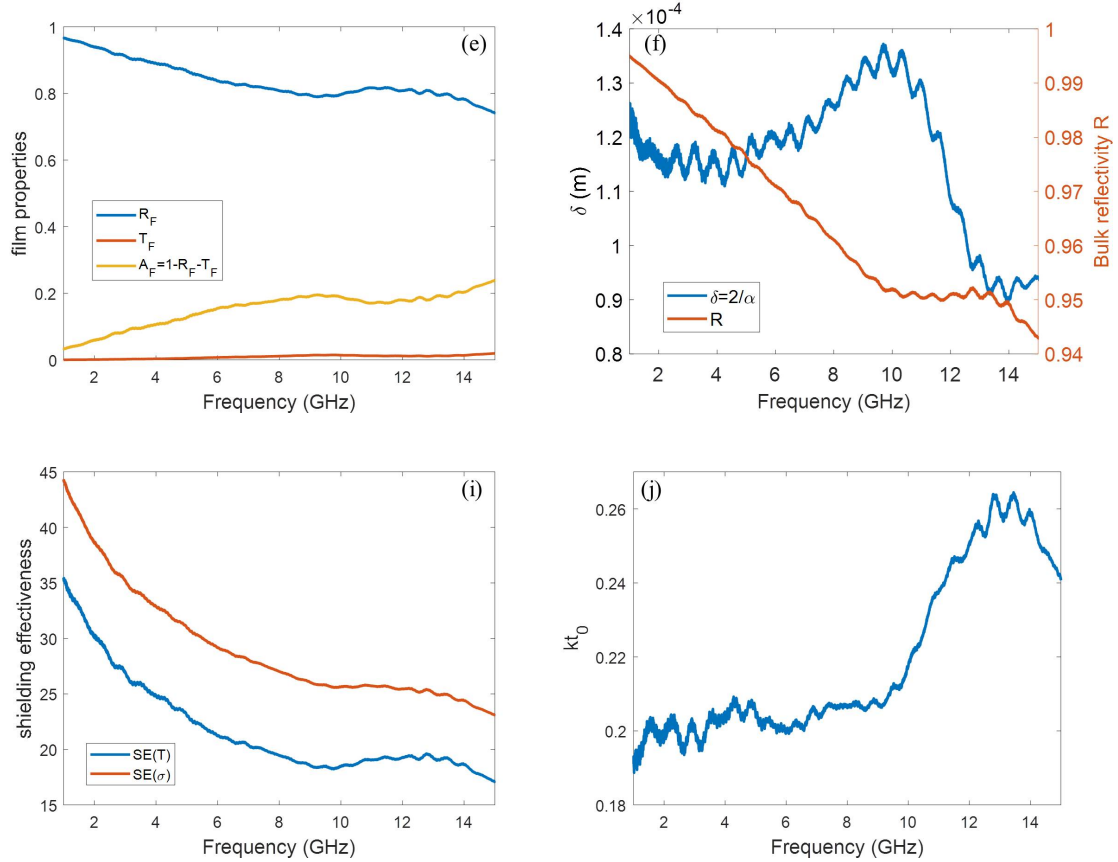


Figure 5.7: Measured quantities for a Al foil with thickness $t=0.015$ mm $< \delta$. (g) R_F, T_F, A_F ; (h) skin depth δ , bulk reflectivity R ; (i) compare shielding effectiveness $SE = \log(T)$ with Simon's formula Eq. 5.20; (j) Compare $|kt_0|$ vs. 1, $|kt_0| \ll 1$, so the substrate effect needs to be considered.

5.4 Future work

Our goal is to develop a general procedure to characterize the microwave properties of materials. Currently the procedures for good metals is verified, or if the condition $|Z_S^{eff}| \ll |Z_{sub}|$ holds. In the case that the substrate is a dielectric-like material, we have to find the impedance of the dielectric-like material. We find the

Corbino methods to deal with dielectric-like materials need further development. The Corbino method measures the electrical impedance and relates it to the wave impedance of the sample under study. Therefore in order to use the Corbino method, it requires that the sample have some degree of metallic response. In general the sample will display a metallic response through a physical current $J = \sigma E$ along with a dielectric response through a parallel displacement current $J_d = \epsilon dE/dt$. Since the Corbino method uses an open circuit as a standard, if the sample has only a dielectric response, a bare substrate will act essentially like an open circuit. And the measured impedance won't reflect the wave impedance of the material. Hence for dielectric materials, one must use a totally different approach to do calibration and data analysis. There are some approaches for characterization of dielectrics using a similar configuration [112–118]. We'll refer to those methods and try to develop a procedure to get the impedance of the dielectric-like materials.

Chapter 6: Conclusions and Future Work

6.1 Conclusions

In this work, we have studied several nonlinear systems applying the Random Coupling Model to each case. Circuit elements mainly exhibit nonlinear IV curves, perhaps together with nonlinear capacitance and inductance. They are point-like nonlinearities added to the wave chaotic systems. They can be associated with the sources to create nonlinear ports, or can be located anywhere in the system to create a nonlinear environment. The billiard made of superconducting materials has nonlinear surface impedance. They represent wave chaotic systems with nonlinear boundaries. We have studied the harmonic statistics as well as power dependent statistics of the S-parameters. For the circuit elements added to generate harmonics or a nonlinear port, we are able to characterize their nonlinear properties. The billiard itself is still linear and the RCM can be applied in principle. For the Pb cut circle, the loss parameter changes because the quality factor changes, which is a result of the nonlinear surface resistance. It will be interesting to see how the statistics change due to the nonlinear reactance like the TiN on Si wafer cut-circle billiard.

We are also interested to see the nonlinear statistics in the system where the

waves lack the property of linear superposition. For example, a system with a continuous medium with nonlinear properties. We tried to put diodes randomly in the bowtie billiard, and to look for nonlinear dielectric or magnetic materials, etc. For diodes located in the billiard, simulations in CST (Computer Simulation Technology) indicates a trend for the power dependent statistics. The higher the input pulse amplitude, the larger the fitted loss parameter, one reason for this might be that the input signal is converted into harmonics and lost at the driving frequency. Meanwhile experimentally, we haven't been able to observe the nonlinearity due to the fact that the signal is too low when it reaches the diodes. Similarly for the nonlinear dielectric or magnetic materials, we haven't been able to find very nonlinear materials or the signal is too low to drive the materials into the highly nonlinear regime. Some preliminary simulations of nonlinear media are explored in CST showing strong nonlinearity but also nonphysical features. Therefore no solid conclusions can be drawn from it yet. The results of these simulations are detailed in Appendix B.

Table 6.1: Summary of various kinds of nonlinearity studied

Nonlinear sources	Mechanism	Type of Nonlinearity
diode	$I - V$ curve, capacitance C	point like
dielectrics/ferrites	$\vec{D}(\vec{E})$ or $\vec{B}(\vec{H})$	continuum media
superconducting billiard	impedance $Z = R + iX$	boundary

Table 6.1 summarizes various kinds of nonlinearity we have considered. We hope to cover as many different mechanisms of nonlinearity as we can. By examining

various nonlinear wave chaotic systems, and applying the RCM analysis, the universal or non-universal properties of these nonlinear wave chaotic systems are analyzed. The nonlinear circuits and impedance have covered a wide range of nonlinearities in real life. Though the study is not complete, this is an important step in the ongoing effort to create the science of nonlinear wave chaos. Furthermore, in acoustics, there are corresponding definitions for the impedance and scattering matrix. The RCM has been verified to work in over-moded acoustic enclosures as well [45]. Thus from the study of the properties in those nonlinear microwave chaotic systems, it is promising to generalize or predict the properties of nonlinear systems to a broader range of nonlinearities and other wave chaotic systems as well.

6.2 Future Work

As seen from the dissertation, the nonlinear systems are mainly studied in the 2D microwave billiards. This is because the 2D billiards have been deeply studied to verify the RCM, and also the signals propagating in the 2D billiard are stronger, thus easier to drive devices and materials into the nonlinear regime. We have not been very successful in creating a continuous nonlinear medium, either because the signal is too small or the lack of strong nonlinear sources. Therefore the solution could be either to have larger signals or to look for more extreme nonlinear sources. We have started to apply the RCM to quantum graphs which are considered to be 1D microwave chaotic systems. The signals in 1D systems can be more concentrated and stronger compared with 2D systems. If the RCM

can be applied to the 1D graph, it will be easier to observe nonlinearities. To find strong nonlinear sources, we can employ active circuit elements. Alternatively our group studied rf SQUID metamaterials which are highly nonlinear. We recently started applying machine learning techniques to study wave chaotic systems. Adding nonlinearity would benefit the fields of both machine learning and wave chaos. The interest in nonlinear systems is growing. Making use of X-parameters in statistical analysis of fields might be a direction to more quantitatively study nonlinear systems.

Appendix A: Procedure for RCM Data Analysis

Here we outline the process to collect and analyze data from microwave billiards and attempt to identify the universal fluctuations of impedance embedded in the data. This is the procedure of using the Random Coupling Model (RCM) to remove the system-specific information from ensemble data and to recover the universal fluctuations.

Take the one-port 1/4 bowtie billiard (Fig. A.1(a)) as an example to show the procedure for RCM data analysis. The 1/4 bowtie billiard has an area $A = 0.115 \text{ m}^2$, height $h = 7.9 \text{ mm}$ with cut-off frequency for higher-order modes $f_c = c/2h = 19 \text{ GHz}$, and fundamental resonant frequency $f_1 = c/(2\sqrt{A}) = 0.42 \text{ GHz}$ [12]. The mean mode spacing in a 2D billiard is $\Delta k_n^2 = 4\pi/A$, $\Delta f_{2D} = c^2/\omega A$. For a 3D cavity, the mean mode spacing is $\Delta k_n^2 = 2\pi^2/kV$, $\Delta f_{3D} = \pi c^3/2\omega^2V$.

A.1 Gather ensemble data for the cavity scattering parameter \bar{S}_{cav}

The perturbers as shown in Fig. A.1(a) are moved to different positions for each realization. The port location is typically several wavelengths away from the billiard boundary and the perturbers. The perturbers should not alter the near-field structure of the port(s), as we assume that the radiation impedance of the port(s) is

the same in all realizations of the ensemble. It is also good to use perturbations that keep the area (or volume) of the billiard fixed, thus preserving the same mean-mode spacing in every realization.

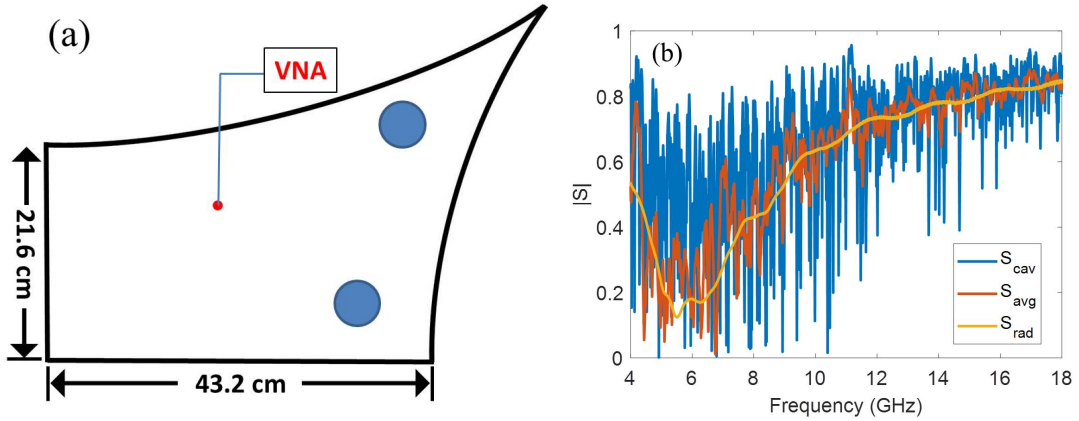


Figure A.1: (a) One-port measurements of 1/4-bowtie billiard with two cylindrical perturbers (the two blue solid circles). (b) Typical results for S_{cav} . Single realization of the bowtie billiard with perturbers (blue). S_{avg} Average over 120 realizations (red). S_{rad} Radiation S-parameters where the billiard boundaries are covered with microwave absorbers, and no perturbers are present (yellow).

To obtain good statistics, a certain number of randomized ensemble realizations need to be collected. For the bowtie, around 90 realizations can be obtained by randomly moving the perturbers, visiting all the space available, and this is a good ensemble. A good perturbation should be able to shift the resonant frequency on the order of the mean mode spacing. The Pearson correlation coefficient of the S-parameter, defined as $\rho(S_1, S_2) = \frac{cov(S_1, S_2)}{\sigma(S_1)\sigma(S_2)}$ should be used to check the statistical independence of the realizations [37]. Here the covariance $cov(S_1, S_2)$ is taken over the entire frequency range of the data, typically many GHz wide and encompassing hundreds of modes. $\sigma(S_1)$ and $\sigma(S_2)$ are the standard deviation of S_1 and S_2 , respectively. Fig. A.2 shows an example of the correlation coefficients calculated for

different realizations of a two-port bow-tie experiment, $\rho(S^1, S^k)$ and $\rho(S^1, S^{k+1})$ for S_{11} and S_{12} respectively, where k runs from 1 to the number of realizations in the ensemble.

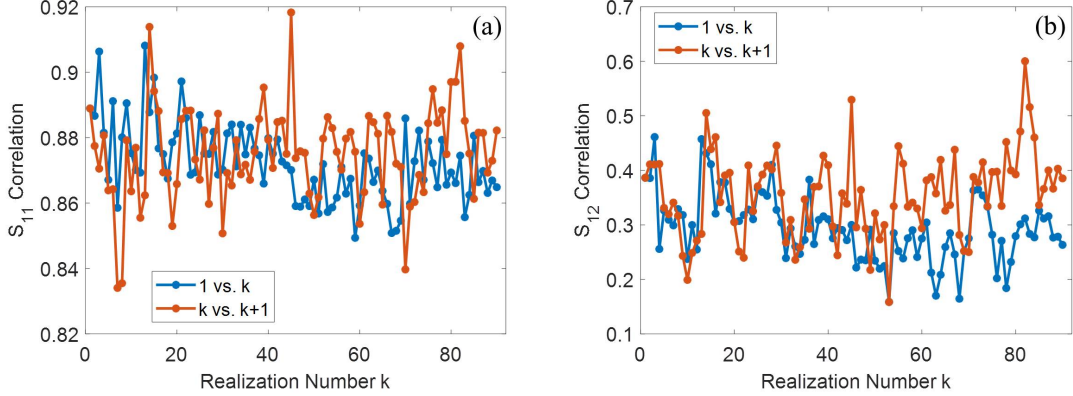


Figure A.2: For a two port bowtie experiment, with 91 realizations. (a) Correlation coefficient $\rho(S_{11}^{(1)}, S_{11}^{(k)})$ and $\rho(S_{11}^{(k)}, S_{11}^{(k+1)})$. (b) Correlation coefficient $\rho(S_{12}^{(1)}, S_{12}^{(k)})$ and $\rho(S_{12}^{(k)}, S_{12}^{(k+1)})$. The correlation coefficient of S_{12} is much smaller compared with that of S_{11} .

Other measures of statistical quality include evaluation of the ratio Λ of the maximum transmitted power to the minimum transmitted power at each frequency [38]. One can also look at the uniformity of the angular distribution of the S-matrix values in the complex S-plane [20].

A.2 Calculate the ensemble-averaged impedance $\bar{\bar{Z}}_{avg}$

The RCM is developed in the impedance domain. After getting a good ensemble of S-parameters, first convert the S-parameters to Z-parameters.

$$\bar{\bar{Z}} = \bar{\bar{Z}}_0^{1/2} (\bar{\bar{1}}_N + \bar{\bar{S}}) (\bar{\bar{1}}_N - \bar{\bar{S}})^{-1} \bar{\bar{Z}}_0^{1/2} \quad (\text{A.1})$$

where $\bar{\bar{Z}}_0$ is a real diagonal matrix whose elements are the characteristic impedances of the waveguide (or transmission line) input channels at the N driving ports, which are typically 50Ω . In addition $\bar{\bar{I}}_N$ is an $N \times N$ unit matrix. RCM states that the statistical properties of the cavity impedance Z_{cav} are described by a universally fluctuating impedance $\bar{x}i$ that is dressed by system specific properties captured by the ensemble average impedance Z_{avg} as:

$$\bar{\bar{Z}}_{cav} = i \cdot Im(\bar{\bar{Z}}_{avg}) + [Re(\bar{\bar{Z}}_{avg})]^{1/2} \cdot \bar{\bar{\xi}} \cdot [Re(\bar{\bar{Z}}_{avg})]^{1/2} \quad (\text{A.2})$$

where $\bar{\bar{Z}}_{avg}$ is an average of impedance over an ensemble of cavity realizations and (or) frequencies. $\bar{\bar{Z}}_{avg}$ contains the system specific features including the radiation impedance of the ports and short orbits that survive the ensemble averages [28, 29]. The “radiation impedance” represents the impedance measured at the ports of the scattering enclosure in the case that the waves are allowed to enter the enclosure through the port but not return, as if they were absorbed in the enclosure or radiated to infinity. Experimentally, it can be measured with the empty bowtie billiard whose boundary is covered with perfect microwave absorbers. A “short orbit” is a ray trajectory that leaves a port and soon returns to it, or another port, instead of ergodically sampling the system. It is the result of the port-wall and port-port interactions that introduce deterministic field components which can remain fixed throughout part or all of the ensemble. $\bar{\bar{Z}}_{avg}$ can also be estimated if the radiation impedance of the ports and the port locations and cavity shape are known. $\bar{\bar{Z}}_{avg}$ can be approximately obtained by appropriately frequency averaging $\bar{\bar{Z}}_{cav}$; and $\bar{\bar{Z}}_{rad}$ can be approximately obtained by appropriately frequency averaging $\bar{\bar{Z}}_{avg}$. Fig. A.3

shows the data from Fig. A.1 for the bow-tie billiard in terms of the three impedance quantities defined above.

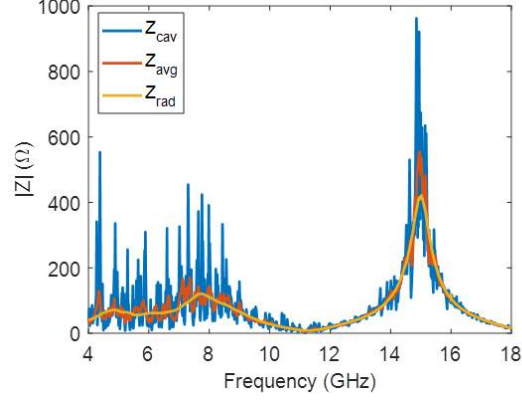


Figure A.3: Results shown in Fig. A.1(b) presented in the impedance domain. \bar{Z}_{cav} - Single realization of the bowtie billiard with perturbors (blue). \bar{Z}_{avg} - Average over 120 realizations (red). \bar{Z}_{rad} - Radiation impedance where the billiard boundaries are covered with microwave absorbers, and no perturbors are present (yellow).

A.3 Extract the fluctuating normalized impedance $\bar{\xi}$ from the data

By inverting Eq. A.2 and subtracting the non-universal features from \bar{Z}_{cav} in each realization, one can uncover a statistically fluctuating quantity $\bar{\xi}_{data}$ that is embedded in the data, through Eq. A.3. Under some circumstance this fluctuating quantity corresponds to the complex $\bar{\xi}$ that is predicted by Random Matrix Theory.

$$\bar{\xi}_{data} = [Re(\bar{Z}_{avg})]^{-1/2} \cdot [\bar{Z}_{cav} - i \cdot Im(\bar{Z}_{avg})] \cdot [Re(\bar{Z}_{avg})]^{-1/2} \quad (\text{A.3})$$

It has been hypothesized that all sufficiently complex wave chaotic systems have universal impedance fluctuations described by the Random Matrix Theory (RMT).

According to the theory [72, 73], for a two port system:

$$\bar{\xi}_{rmt,a,b} = -\frac{i}{\pi} \sum_{m=1}^M \frac{W_{am} W_{bm}}{\lambda_m^{rmt} - i\alpha} \quad (\text{A.4})$$

The element $\bar{\xi}_{rmt,a,b}$ is the impedance between port a and port b, and the sum is over the M eigenmodes of the closed wave scattering enclosure, W_{am} (or W_{bm}) represents the coupling between the port a (or the port b) and the m^{th} eigenmode. Based on the assumption of the random plane wave hypothesis (the Berry hypothesis), for a wave-chaotic cavity enclosure filled with reciprocal media (i.e., that has wave propagation properties that are time-reversal invariant), W_{am} and W_{bm} are independent Gaussian random variables of zero mean and unit variance. λ_m^{rmt} is the m^{th} eigenvalue of a large random matrix. The statistics of these eigenvalues are based on RMT, and they are found from a large random matrix selected from the GOE (Gaussian Orthogonal Ensemble) for the time-reversal-invariant case. The Matlab code for generating the universal impedance statistics for a given loss parameter should be found in the Anlage group drive.

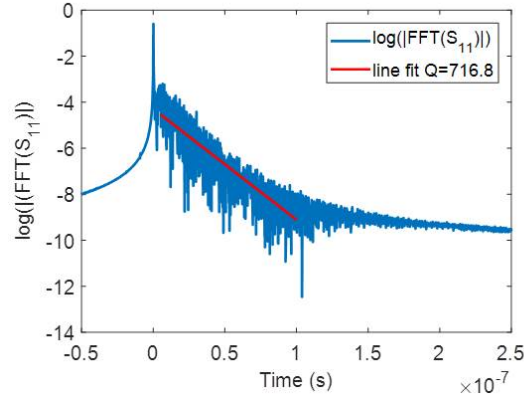


Figure A.4: Line fit $\log(\text{abs}(\text{IFFT}(S_{11})))$ to estimate the average quality factor $Q = -\omega_0/(2 * \text{slope})$, where ω_0 is the center frequency of the frequency band utilized

The loss parameter α is the only parameter determining the statistics of the universal fluctuations. In the case of a two-dimensional billiard the loss parameter is

given by $\alpha = k^2/(\Delta k^2 Q) = k^2 A/(4\pi Q)$ (3D is $k^3 V/(2\pi^2 Q)$); and can be interpreted as the ratio of the typical 3-dB bandwidth of the resonant modes to the mean spacing in frequency between the modes. $k = 2\pi f/c$ is the wave number of frequency f . The area of the billiard is A , and Q is the typical loaded quality factor of the enclosure under the assumption that losses are uniform. The quality factor is measured from the energy decay time constant (τ) for the enclosure from which $Q = \omega\tau$. The energy decay time constant is obtained by inverse Fourier transforming the measured reflection coefficient ($S_{11}(\omega)$) to the time domain, then squaring the result. The squared result is referred to as the power decay profile. The slope is computed by smoothing the average of the power decay profile. The slope ($-v$ [dB/s]) is then used to compute the time constant quantity factor $\tau = 4.34/v$. An example is given in Fig. A.4.

A.4 Lowest Usable Frequency (LUF) of the RCM

The RCM only applies to the highly over-moded regime of an enclosure. Several characteristic lengths can be used to determine the lowest usable frequency of the RCM. The characteristic length of the mode stirrer is defined as $L_{stir} = \sqrt{A_{stir}}$, where A_{stir} is the circular area that the mode stirrer sweeps as it rotates, for 2D billiards. Similarly, the characteristic length of the 2D bowtie billiard is defined as $L_{cav} = \sqrt{A_{cav}}$, where A_{cav} is the area of the billiard. For a metallic mode-stirrer, the physical area of the mode stirrer is subtracted in calculating the area of the billiard. The ratio of the characteristic lengths $R = L_{stir}/L_{cav}$ can be used to determine the

necessary size of the mode stirrers in different shape cavities. The ratio R should be large enough to have a frequency change on the order of the mean mode spacing. From various metrics to determine the lowest usable frequency, it is determined to be $\lambda/L_{cav} = 0.2 \sim 0.35$, where λ is the wavelength of the lowest usable frequency [119].

A.5 Determine the Loss Parameter α by fitting the statistics of $\bar{\xi}$

The algorithm for generating $\bar{\xi}_{rmt,a,b}$ can be developed based on Eq. A.4. By varying α , the universal statistics of $\bar{\xi}$ for systems with varying losses can be numerically generated. Starting with a statistical ensemble data set and going the other way around, one can fit the experimentally extracted $\bar{\xi}_{data}$ to $\bar{\xi}_{rmt}(\alpha)$, and the best matching distributions will give an estimate of the loss parameter of the experimental system. Note that when examining data, for a two port system, $\bar{\xi}_{data}$ will produce 8 histograms, i.e., real and imaginary part for each element $\bar{\xi}_{a,b}$. However due to the reciprocity of the system, $\xi_{12} = \xi_{21}$, and ξ_{11} should have the same statistics as ξ_{22} according to Eq. A.4. This is in fact a consistency check on the data. As a result there are 4 unique histograms that are simultaneously fit using a single loss parameter α . This is a very stringent constraint placed on the data PDFs. Figure 5 shows a comparison of fits to $Re(\xi_{11})$ and $Im(\xi_{11})$ PDFs from the one-port bow-tie cavity. They have been independently fit and similar α values are obtained. Alternatively one could fit both PDFs simultaneously with a single value of α . Another important check on the data is that for each distribution created one should have mean values of $\langle Re(\xi_{11}) \rangle = 1$ and $\langle Im(\xi_{11}) \rangle = 0$. For the off-

diagonal components of multi-dimensional impedance matrices one finds that both the real and imaginary $\bar{\xi}$ impedance matrix element PDFs should have mean values of 0.

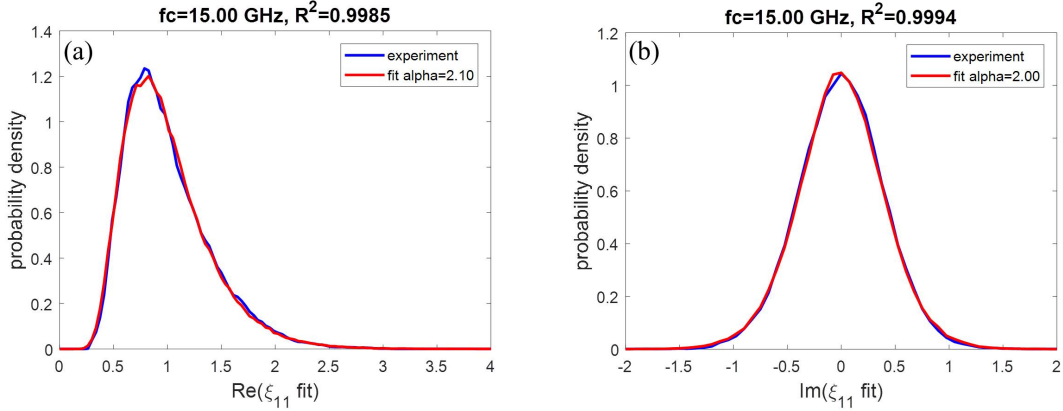


Figure A.5: (a) Experimentally obtained $Re(\xi_{11})$ statistics from one-port bowtie measurement, over 120 realizations in the frequency range 14.5 - 15 GHz. The best fit PDF ($R^2 = 0.9985$) gives $\alpha=2.1$. For the $Re(\xi_{11})$ statistics, one finds that $\langle Re(\xi_{11}) \rangle = 1$. (b) $Im(\xi_{11})$ statistics obtained in a similar way. The best fit PDF gives $\alpha=2.0$, which is almost the same as the fitting from the $Re(\xi_{11})$. Its PDF has a mean of $\langle Im(\xi_{11}) \rangle = 0$.

Fig. A.6 shows the ξ_{rmt} statistics predicted by Random Matrix Theory for various loss parameters α in a time-reversal symmetric (GOE) system [38, 79]. For very high loss $\alpha \sim 10$, the $Re(\xi)$ and $Im(\xi)$ statistics approach a Gaussian distribution centered at 1 and 0, respectively. For extremely low loss $\alpha \sim 0$, the $Im(\xi)$ distribution goes to a Lorentzian $1/\pi(1+x^2)$, while the $Re(\xi)$ distribution approaches a “one-sided delta function” that always has a mean value of 1.

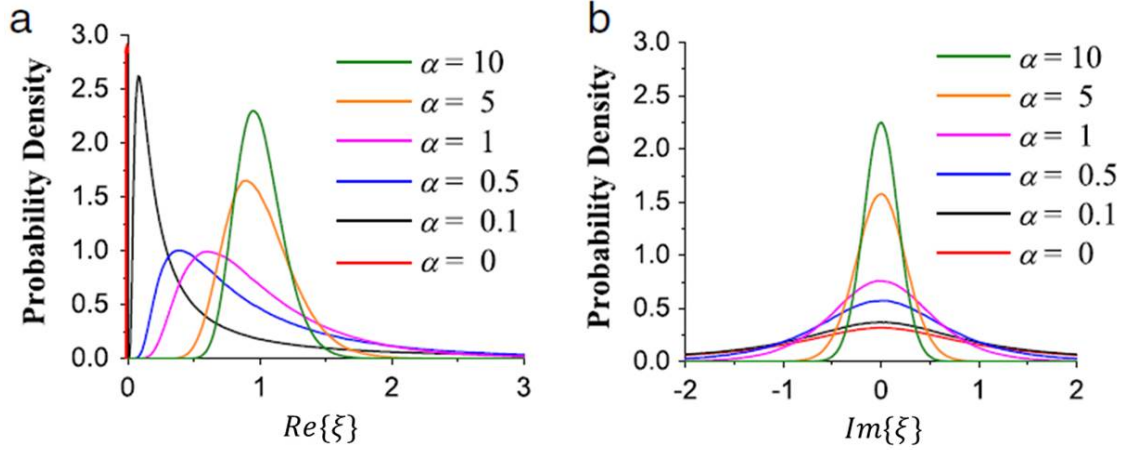


Figure A.6: Random Matrix Theory predictions for the PDF of normalized impedance for various loss parameters α in a time-reversal symmetric system, i.e. GOE (Gaussian Orthogonal Ensemble) statistics. (a) $Re(\xi_{11})$ statistics; (b) $Im(\xi_{11})$ statistics.

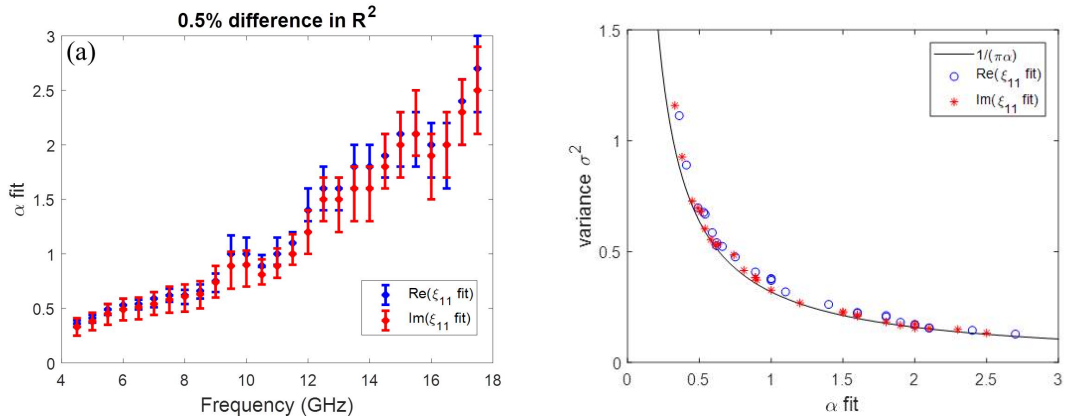


Figure A.7: (a) The consistency of fitted α from $Re(\xi)_{11}$ and $Im(\xi)_{11}$ experimental PDFs. (b) The variance of $Re(\xi)_{11}$ and $Im(\xi)_{11}$ PDFs are predicted to be $a/\pi\alpha$ for $\alpha \gg 1$.

Fig. A.7(a) shows the comparison of fit α values for fits to the $Re(\xi)_{11}$ and $Im(\xi)_{11}$ PDFs in a range of frequencies from 4 to 18 GHz in the bow-tie billiard. The fits are performed on PDFs constructed in 1 GHz wide frequency windows from an ensemble of 120 realizations of the 2D bow-tie. The error bars on the

α values from the two PDFs are estimated by a 0.005 difference compared to the best R^2 . Note that the fit values are consistent with each other within the error bars. Fig. A.7(b) shows that the variance of the PDFs is a good predictor of the loss parameter [32]. For diagonal elements of the normalized impedance matrix, $\sigma^2(\text{Re}(\xi_{11})) = \sigma^2(\text{Im}(\xi_{11})) = 1/\pi\alpha$; and for off-diagonal components, $\sigma^2(\text{Re}(\xi_{12})) = \sigma^2(\text{Im}(\xi_{12})) = 1/2\pi\alpha$; when $\alpha \gg 1$ [32].

A.6 Some reasons why RCM statistics may NOT be seen in experimental data

1. The ensemble is not of sufficiently high statistical quality. Perform the statistical tests noted in section A.1 above to make sure that the quality of the data is good.
2. The RCM is simply not applicable to your data because one or more of the basic assumptions of the model are not satisfied. For example, the loss may be too inhomogeneous (e.g. there is a large hole in one side of the billiard [120]), the random plane wave hypothesis may not be valid (for example in a graph), the system may be a mixture of regular and chaotic classical phase space (e.g. mushroom billiard) [46], or the ports may be lossy [48, 119].
3. You may be trying to utilize the RCM in a low frequency regime below the lowest usable frequency, as noted in section A.4 above [119].

A.7 Weyl’s formula

For a two-dimensional billiard, the cumulative level density of states $N(E)$ which is the number of “energy levels” with energy less than E ($E \sim k^2 = (2\pi f)^2/c^2$), where f is the cavity resonant frequency) is given by [121]

$$N(E) = C_1 E + C_2 E^{1/2} + O(E^0) \tag{A.5}$$

In the case of the empty cavity without ferrite (GOE case), $C_1 = A/4\pi$ where A is the cross-sectional area of the cavity, C_2 depends on the cavity boundary conditions, $C_2 = L/4\pi$ for Neumann boundary conditions and $C_2 = -L/4\pi$ for Dirichlet boundary conditions, where L is the perimeter of the cavity. In the semi-classical regime ($N(E) \gg 1$), and note that the first term, $C_1 E$, is large compared to the second term. Thus, for large E , $N(E)$ is approximately linear in E .

A.8 Short Orbit Correction

A “short orbit” (or a “short ray trajectory”) means one ray trajectory whose length is not much longer than several times the characteristic size of the scattering enclosure, and the trajectory enters the scattering enclosure from a port, bounces (perhaps several times) within the scattering region, and then returns to a port. A “port” is the region in which there is a connection from the billiard/scatterer to the outside world.

Hart et al [27, 29]. extended the RCM by considered a port and its nearby walls as a generalized port. This method takes the information of the geometry

of the system to compute the short-orbit contribution to the radiation impedance. More specifically, the generalized system-specific impedance matrix (the short-orbit corrected radiation impedance matrix) is written as

$$\bar{\bar{Z}}_{SOC} = \bar{\bar{Z}}_{rad} + \bar{\bar{R}}_{rad}^{1/2} \cdot \bar{\bar{\zeta}} \cdot \bar{\bar{R}}_{rad}^{1/2} \quad (\text{A.6})$$

where $\bar{\bar{Z}}_{rad}$ is the diagonal radiation impedance matrix representing the features of the ports, $\bar{\bar{R}}_{rad}$ is the real part of $\bar{\bar{Z}}_{rad}$, and $\bar{\bar{\zeta}} = \bar{\bar{\rho}} + i\bar{\bar{\chi}}$ is the short-orbit correction matrix. For the system with N ports, the (n, m) element of the $N \times N$ matrix $\bar{\bar{\zeta}}$ is:

$$\zeta_{n,m} = \sum_{b(n,m)} [-p_{b(n,m)} \sqrt{D_{b(n,m)}} \exp[-(ik + \kappa)L_{b(n,m)} - ikL_{port(n,m)} - i\beta_{b(n,m)}\pi]] \quad (\text{A.7})$$

where $b(n, m)$ is an index over all classical trajectories which leave the n^{th} port, bounce $\beta_{b(n,m)}$ times, and return to the m^{th} port. Note that for the off-diagonal term ($n \neq m$), $\zeta_{(n,m)}$ includes the direct orbit from the n^{th} port to the m^{th} port without bouncing on the walls ($\beta = 0$). $L_{b(n,m)}$ is the length of the trajectory $b(n, m)$. The effective attenuation parameter, $\kappa = k/2Q = \alpha\Delta k$, takes account of loss, where Q is the quality factor, α is the loss parameter, k denotes the wave number of a plane wave, and Δk is the average spacing between resonant wave numbers. $L_{port(n,m)}$ is the port dependent constant length between the n^{th} port and the m^{th} port, and it is a correction term for the orbit length required to explain the experimental results. $D_{b(n,m)}$ is the orbit stability factor which is a geometrical factor of the trajectory, and it measures how the energy spreads out along the orbit path. $p_{b(n,m)}$ is the survival probability of the trajectory due to the position of the perturbing objects in the ensemble.

A.9 Determine Z_{rad} using the Time Gating Method (TGM)

Time-gating is a method by which a frequency domain measurement is effectively averaged over a sliding window in the frequency domain [48, 119]. The method applies the Fourier transform of the measured complex reflection coefficient to the time domain, gating it in time, and Fourier transforming back to the frequency domain. If T_G is the duration of gating, then T_G^{-1} is the effective width of the frequency window. The purpose of the time gating is the determination of the radiation impedance of the port including the effect of nearby reflections and excluding the effect of multiple far field reflections. It assumes the port is lossless or very low loss.

The TGM is implemented in some modern vector network analyzers (VNA). In a VNA, the reflection coefficient is measured in the frequency domain using a swept CW source and a receiver that tracks the amplitude and the phase of the received signal. The complex reflection coefficient $\bar{S}(f)$ is transformed to the time domain using an inverse fast Fourier transform (IFFT), $s(t) = F^{-1}\{\bar{S}(f)\}$. This time domain signal $s(t)$ is multiplied by a gating window function $g(t)$ to select the duration of the time window of interest and suppress the rest. The gated time domain signal is Fourier transformed back to the frequency domain to arrive at the desired result $\bar{S}_g(f)$, $\bar{S}_g(f) = F\{s(t)g(t)\}$.

Another way to implement the TGM is to use the fact that multiplication in the time domain is equivalent to a convolution in the frequency domain. The time domain gating window is transformed to the frequency domain using a fast Fourier

transform (FFT) and convolved with the raw frequency domain measurement. The result is the gated reflection coefficient. This can be expressed as,

$$\bar{S}_g(f) = \bar{S}(f) \otimes \bar{G}(f) \quad (\text{A.8})$$

where $\bar{S}_g(f)$ is the unprocessed frequency domain S-parameter measurement, $g(t)$ is the gating function in time and $\bar{G}(f)$ is its Fourier transform, and \otimes is the convolution operator.

A.10 RCM for ports with highly localized loss

The radiation impedance of the port(s) can be measured by lining the walls with absorbers, or by using the TGM method which does not require physical access to the interior of the enclosure walls. However, when this is significant localized loss at the port, the measured impedance at the terminal will not characterize the amount of power that enters the cavity. The antenna must be considered as a T - or π -network of impedances. For the general case where the enclosure is a high loss system ($\alpha > 5$), the equation for the impedance of a lossy antenna attached to a complex enclosure is

$$Z_{in} = Z_{ant} + \eta Re[Z_{ant}] \delta\xi \quad (\text{A.9})$$

where η is the radiation efficiency of the antenna. $\delta\xi = \xi - 1$ where ξ is the fluctuating normalized impedance. Z_{ant} is the input impedance of the lossy antenna radiating in free space. The radiation efficiency is defined as the ratio of the power radiated to the power delivered to the antenna.

Appendix B: Nonlinear Simulation

This part discusses some of the nonlinear simulations we have tried, mostly in CST, as well as an introduction to X-parameters. In CST, we have tried simulation with materials with nonlinear dielectric/magnetic models, built-in diode models, and a nonlinear SPICE model. This is not an exhaustive treatment because there could be other nonlinearity sources, such as nonlinear surface models, or nonlinear simulations in other simulation tools.

B.1 Nonlinear Materials in CST

CST offers various models of materials for simulation, including conducting materials, dispersive materials, nonlinear materials, surface impedance models, etc. The details are given in the corresponding help page in the program. Here we summarize the simulation we have done with the nonlinear materials.

Dielectrics or ferrites with nonlinear response are a class of nonlinearity sources with continuum nonlinearity. To have a realistic modelling of these nonlinear materials, a general representation of the nonlinear response of the electric flux density

$\vec{D}(\vec{r}, t)$ to the electric field $\vec{E}(\vec{r}, t)$ could be

$$\vec{D}(\vec{r}, t) = \varepsilon_0 \varepsilon_L \vec{E}(\vec{r}, t) + \varepsilon_0 \chi^{(2)} \vec{E}(\vec{r}, t) \vec{E}(\vec{r}, t) + \varepsilon_0 \chi^{(3)} \vec{E}(\vec{r}, t) \vec{E}(\vec{r}, t) \vec{E}(\vec{r}, t) + \vec{P}_{NL}(\vec{r}, t) \quad (\text{B.1})$$

where ε_L represents the linear contribution to the polarization, whereas $\chi^{(2)}$ and $\chi^{(3)}$ correspond to the second and third order susceptibility, respectively. In general, they are real second and third order tensors and therefore described by 9 and 27 real values, respectively. In CST simulation, it is simplified to consider an anisotropic but diagonal case where only 3 diagonal coefficients are needed, For the isotropic case, further simplification can be made to consider only one real coefficient. The tensors are then determined by one real coefficient times an identity matrix. $\vec{P}_{NL}(\vec{r}, t)$ is noted to include other sources of nonlinearity, eventually of order higher than 3. Similar representation also applies to the magnetic flux density $\vec{B}(\vec{r}, t)$ and the magnetic field $\vec{H}(\vec{r}, t)$. Since Eq. B.1 is represented in the time domain, and there is no easy Fourier transform of these equation, to include the nonlinear materials into simulation, only the transient solver can be used.

In the simulation, the nonlinear model Eq. B.1 can be simplified to consider only one term, for example, only consider the 2nd or 3rd order response. We can write the nonlinear dependence of the field as a space-time variant material permittivity and permeability,

$$\vec{D}(\vec{r}, t) = \varepsilon_0 \varepsilon_L \vec{E}(\vec{r}, t) + \varepsilon_0 \Delta \varepsilon_{NL} \vec{E}(\vec{r}, t) \quad (\text{B.2})$$

then for the 2nd order nonlinearity $\chi^{(2)}$, we have $\Delta \varepsilon_{NL} = \chi^{(2)} \vec{E}(\vec{r}, t)$ which may produce both a positive and negative variation of the permittivity. As noted in the

help page, the negative values of $\Delta\epsilon_{NL}$ might cause the simulation to be unstable and requires one to decrease the time step to enforce stability. As a result, the total simulation time will be increased. While for the 3rd order nonlinearity $\chi^{(3)}$, $\Delta\epsilon_{NL} = \chi^{(2)}\vec{E}(\vec{r}, t)^2$ will always be positive, hence there is no issues of stability. Therefore we mainly studied models with the 3rd nonlinearity.

For the higher order term $\vec{P}_{NL}(\vec{r}, t)$, CST offers two default models to consider the effect of the finite response time of the material. The dispersive Kerr effect considers that the medium changes its properties with time showing a relaxation behavior. Alternatively the dispersive Raman effect considers the material showing resonance effects. The details of the models are given on the CST help page. For the purpose of our simulation, there are not big differences among these models.

Fig. B.1 shows the CST model that a 1/4 bowtie billiard with perturbers resembling the real experimental setup we have. The billiard is filled with a nonlinear material. And we will try various nonlinear models.

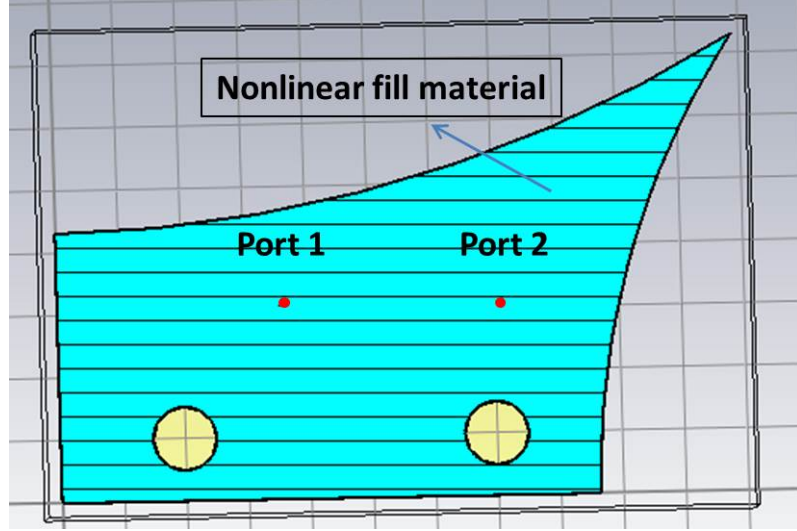


Figure B.1: The CST model where the bowtie billiard is filled with a 3^{rd} nonlinear dielectric material $\vec{D}(\vec{r}, t) = \epsilon_0 \epsilon_L \vec{E}(\vec{r}, t) + \epsilon_0 \chi^{(3)} \vec{E}(\vec{r}, t)^3$. The two yellow circles are perturbors.

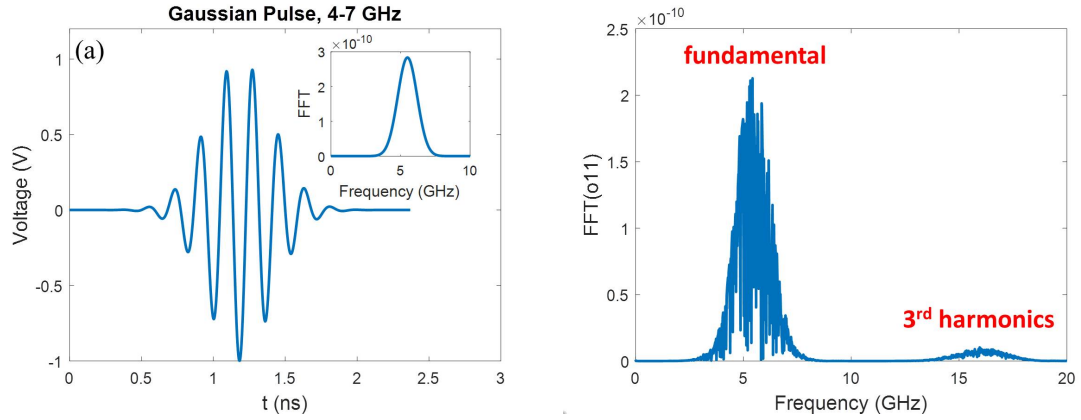


Figure B.2: For the filled material with a nonlinear Kerr model, where $\chi_{\infty}^{(3)} = 10^{-9}$ [m/V]², $\chi_S^{(3)} = 10^{-8}$ [m/V]², and $\tau = 10^{-9}$. (a) Input Gaussian signal in the frequency range 4-7 GHz at port 1 in the time domain; inset shows the Fourier Transform of the signal in the frequency domain. (b) Fourier Transform of the output signal at port 1 shows there is 3^{rd} harmonic response.

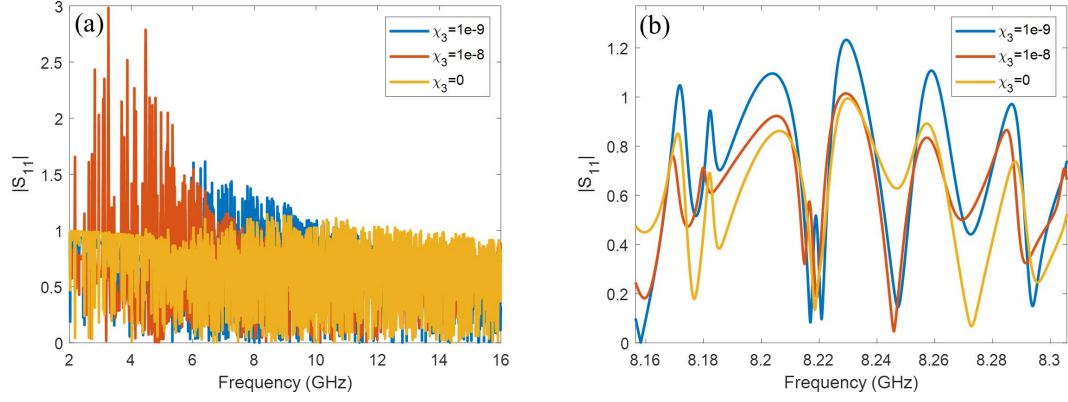


Figure B.3: For the filled material with a nonlinear 3^{rd} order model, where $\chi^{(3)}(\vec{B}) = 0.001 \text{ [m/A]}^2$. (a) $|S_{11}|$ for different $\chi^{(3)}(\vec{E})$ in the frequency range of 2-16 GHz. (b) Detailed view of the nonlinear response at several resonances.

For the material with a nonlinear Kerr model, Fig. B.2 shows that for an input Gaussian pulse in the frequency range of 4-7 GHz at port 1 (see Fig. B.2(a) and inset for its Fourier Transform), the Fourier Transform of the output signal at port 1 shown in Fig. B.2(b) presents the 3^{rd} order harmonic generation. This demonstrates the nonlinear property of the material, and now we are interested to see the S-parameters.

Fig. B.3 shows the S-parameters with nonlinear 3^{rd} order model, including both electrical and magnetic nonlinearity. By changing $\chi^{(3)}$, the degree of nonlinearity is tuned. Fig. B.3(a) shows the S_{11} for several choices of $\chi^{(3)}(\vec{E})$ and Fig. B.3(b) is a detail view of several resonances. The S-parameters clearly change with the parameter $\chi^{(3)}(\vec{E})$, both in magnitude and position of the resonant frequency. However, with the nonlinear term, the magnitude of the S-parameters become larger than 1, which is nonphysical for a passive system. The situation gets worse as the

material is made more nonlinear.

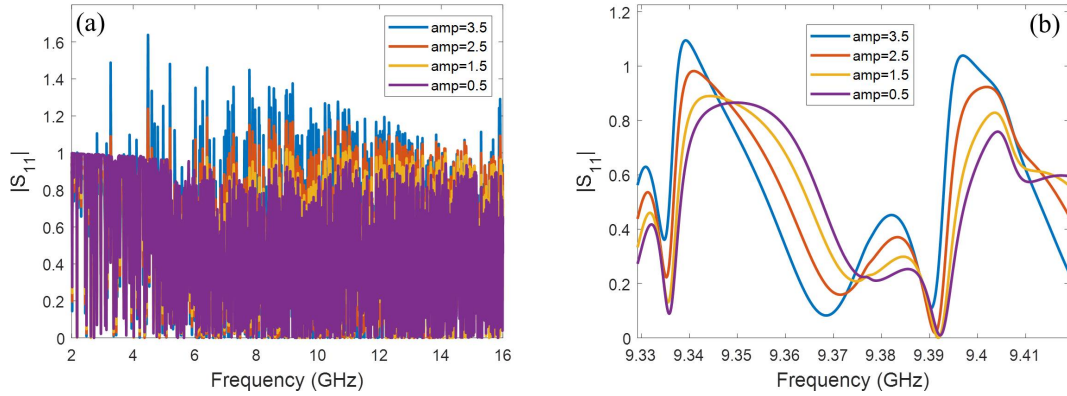


Figure B.4: For the filled material with a nonlinear 3^{rd} order model, where $\chi^{(3)}(\vec{B}) = 0.001 \text{ [m/A]}^2$, $\chi^{(3)}(\vec{E}) = 0 \text{ [m/V]}^2$. (a) $|S_{11}|$ for different input amplitudes in the frequency range of 2-16 GHz. (b) Detail view of the nonlinear response at several resonances.

Another feature of nonlinear system is that the responses are amplitude dependent. Therefore we expect the S-parameters will change for different input amplitudes. Fig. B.4 shows an example of S_{11} vs. input amplitude for a 3^{rd} order nonlinear material. We observe very good nonlinearity. As the amplitude increased, it has a similar effect of increasing the nonlinearity of the system. And similarly, it has the issue of $|S_{11}| > 1$.

For the problem of $|S_{11}| > 1$, we got some feedback from CST support. First, finite difference time domain (FDTD) based code often struggles with cavity simulations. For the resonant billiard we study, the energy gets into the billiard at resonant frequencies. While at some frequencies, the input signal get prompt reflection. When the energy gets into the billiard is lower than the noise floor, it could cause inaccuracy in S-parameters results. The energy should converge in order to

get correct S-parameters. “The resonances are quite broadband so it means the frequency conversion could happen all over the spectrum. Even though Many spikes occurs over unity at many frequencies, there are also many dips (the total energy could still converge).” We have tried to increase the total simulation time, increase the accuracy level (-80 dB), but the issue is not solved. And we’ve tried to make the material with various loss tangent to converge faster. The problem is that it can suppress the magnitude, but also the fluctuations, hence making the S-parameters not that interesting.

B.2 Diode Simulation in CST

CST offers built-in models of lumped network elements to represent simple electronic components, including RLC serial, RLC parallel, diode and general circuit. Diode and general circuit can be used for nonlinear simulation. A general circuit is defined by importing a SPICE file. The next section will show an example with details to include SPICE model in simulation. For the built-in diode model, it is defined by a simple exponential I-V characteristic, shown in Fig. B.5 (see help page). Section 3.3.2 showed some results including the diode and observed the nonlinear S-parameters with different input amplitudes. Similar to the nonlinear materials discussed above, higher order harmonics are also generated by adding a diode. One thing we find in the diode simulation is that the calculation becomes unstable if the input amplitude is too large. An approach to improve the simulation is to decrease the time step in simulation settings. But as a result, the total simulation time will

also increase.

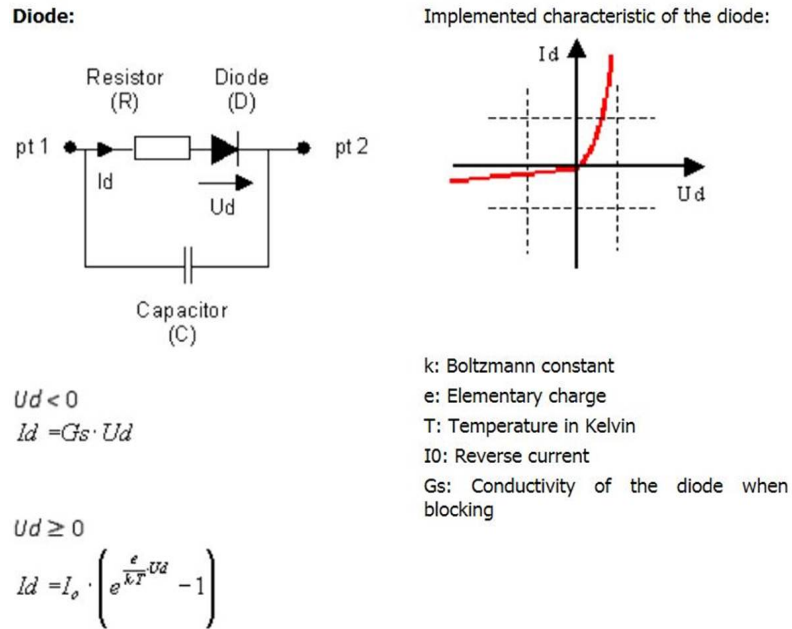


Figure B.5: Built-in diode model in CST lumped network element.

B.3 Incorporating a SPICE model in CST

SPICE models provide more freedom to define the circuit we want to simulate, and we can incorporate it with 3D models in CST. Section 3.2.5 presented the nonlinear port results including the SPICE model of the diode and package. It is very promising as the simulation radiation S-parameters and power results reproduced the key features we observed in experiment. Here I add more details of the procedure.

To begin with, one should know about the syntax to make a SPICE file. CST accepts SPICE source file that ends with *.cir*. Here are some example tutorials for SPICE source files: https://www.seas.upenn.edu/~jan/spice/spice_overview.html and <https://www.cpp.edu/~prnelson/courses/ece220/220-spice-notes>.

pdf. For example, a SPICE model is constructed in section 3.2.5 with two diodes and parasitic properties of the package. Since only two pins are used, it is imported as a diode with two connections.

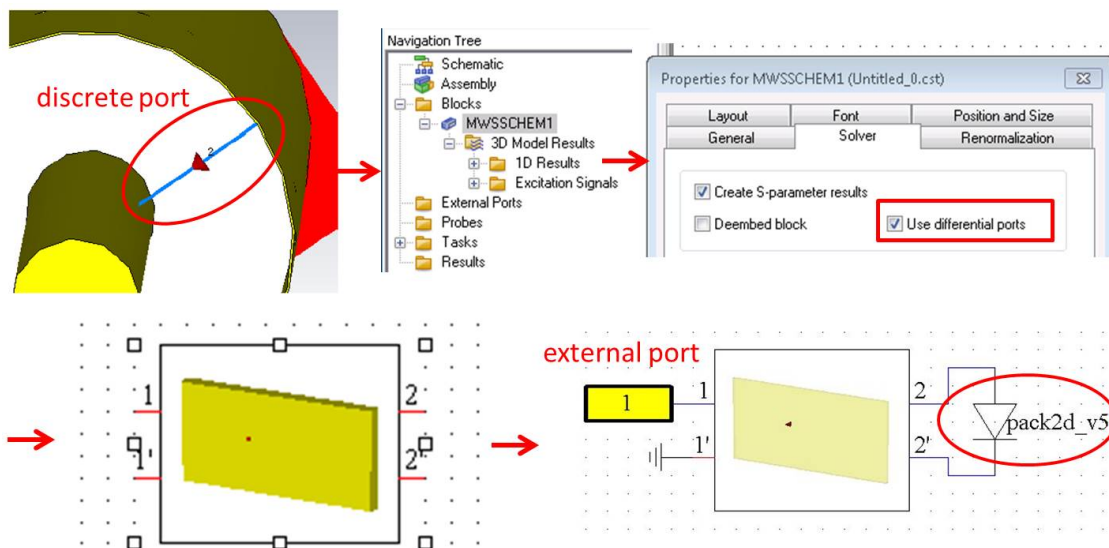


Figure B.6: Procedures to add a SPICE circuit with a 3D model. 1. Add a discrete port in 3D window; 2. Set the ports to be differential ports; 3. Set external port and connect with the imported SPICE circuit.

To simulate the SPICE circuit model with a 3D model, the procedures are shown in Fig. B.6. First in the 3D window, a discrete edge port representing the physical position where the diode will be connected is added. Then go to the schematic window, two numbers indicating the ports will be shown. One is a waveguide port which is defined on the cross section of the transmission lines where the excitation signal comes in. Another is the discrete port that will connect to the SPICE model. Setting the ports to differential allows the voltage signal to be measured between the differential pins instead of referring to the “ideal circuit ground”. For the port with excitation signal, an external pin (the yellow box) is connected

with respect to ground. And the imported SPICE model, named “pack2d_v5”, is connected to the discrete port.

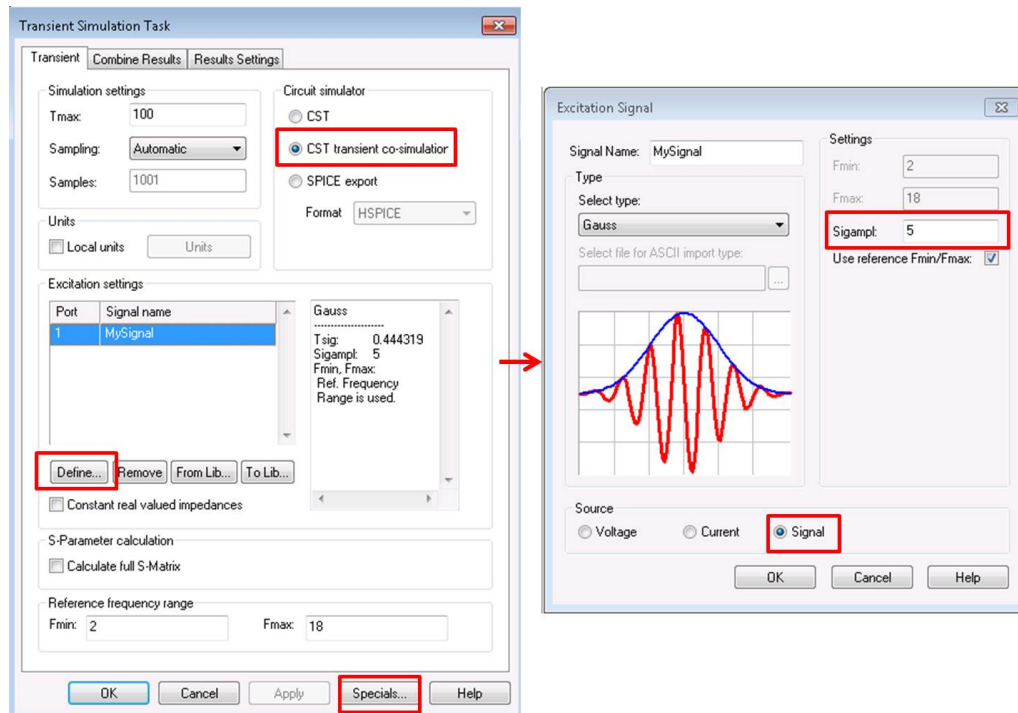


Figure B.7: Set up a transient task with different amplitude excitation signals.

Next, the simulation task can be setup. Go to “task”, select “transient task”. The dialog box for transient task is shown in Fig. B.7. Select “CST transient co-simulation”; for dialog box for “Special...”, in “Maximum Frequency”, choose “Manual Fmax” and then enter the “Max. resolved frequency”; for dialog box “Define...”, here is where the amplitude of the excitation signal is determined, remember to select “Signal” for “Source” to ensure the correct S-parameters will be simulated.

In the simulation presented in section 3.2.5, the total power on several faces are also simulated. That is achieved by firstly defining the face planes to be evaluated. One way to define a face is with the assistance of defining a waveguide port and

then deleting that port. Then place power flow field monitors for simulation. After the simulation is done, the power flow integral over the face can be evaluated in the results template. The short tutorials for this power evaluation and setting up transient co-simulation from CST are available in the Anlage Group Wikipage.

B.4 X-parameters

X-parameters were developed and introduced by Agilent Technologies as functionality included in the N5242A Nonlinear Vector Network Analyzer, and the W2200 Advanced Design System in 2008. Their website provides a lot of information about X-parameters at <https://www.keysight.com/main/editorial.jsp?cc=US&lc=eng&ckey=1619575&nid=-32996.775208.02&id=1619575> X-parameters are applicable to both large-signal and small-signal conditions, for linear and nonlinear components. They are an extension of S-parameters. X-parameters reduce to S-parameters in the small-signal limit, but they also include rich nonlinear component information including harmonic and inter-modulation distortion, compression characteristics with power, and more at the fundamental and all the harmonics [5]. Just like S-parameters, X-parameters also allow for cascading of components that are highly mismatched.

Different from the small signal S-Parameters which are ratios of the input and output power waves, X-parameters measure the absolute amplitudes and all the phases relative to the calibrated phase reference. Then the full waveforms are constructed from that. The nonlinear VNA deals with X-parameters in the Poly-

Harmonic Distortion (PHD) framework. And the simulation with X-parameters can be done in its Advanced Design System (ADS). Here we give a basic introduction to X-parameters and a circuit we have measured in collaboration with Prof. Sameer Hemmady at the University of New Mexico. For more detailed study about X-parameters, we refer to two books [94, 95].

Fig. B.8 shows a spectral analysis of a two-port nonlinear circuit. A_{ef} , B_{ef} denotes the input and output power waves, respectively. e is the port index and f is the harmonic (or carrier) index. Then B_{1k} and B_{2k} will be a function of the input harmonics.

$$B_{1k} = F_{1k}(DC, A_{11}, A_{12}, \dots, A_{21}, A_{22}, \dots) \quad (\text{B.3})$$

$$B_{2k} = F_{2k}(DC, A_{11}, A_{12}, \dots, A_{21}, A_{22}, \dots) \quad (\text{B.4})$$

For a simple case there is one large input complex phasors A_{11} . Then the spectral map of complex large input phasors to large complex output phasors for B_{ef} can be written in terms of X-parameters:

$$B_{e,f} = X_{ef}^{(F)}(|A_{11}|)P^f + \sum_{g,h} X_{ef,gh}^{(S)}(|A_{11}|)P^{f-h} \cdot A_{gh} + \sum_{g,h} X_{ef,gh}^{(T)}(|A_{11}|)P^{f+h} \cdot A_{gh}^* \quad (\text{B.5})$$

where the upper index (F) indicates the simpler nonlinear mapping, (S) and (T) mean the linear non-analytic mapping. A_{gh}^* is the complex conjugates of A_{gh} . P denotes the phase of the harmonics.

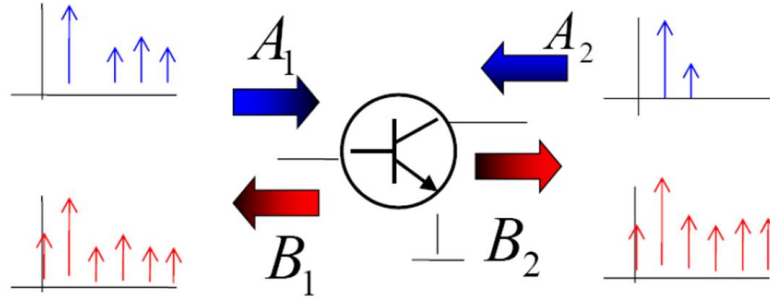


Figure B.8: Spectral analysis of nonlinear components, from [5].

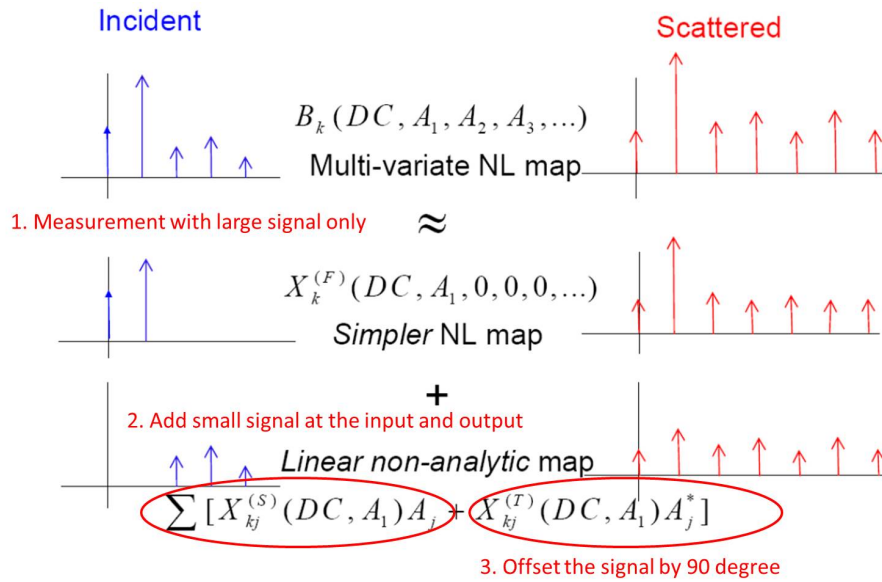


Figure B.9: Procedures to measure the X-parameters, from [5].

Fig. B.9 presents the procedures to measure X-parameters. It provides a better understanding of those terms in Eq. B.5. Firstly, the measurement is done with only one input large signal, say A_1 . By recording the harmonics at all the ports, $X^{(F)}$ terms are determined, which are the simplest nonlinear mapping. Then a second source with a small signal is added, and the output harmonics are measured simultaneously. This will give the $X^{(S)}$ terms. The third step is to offset the phase

on the second driving signal by 90 degrees and measure the output harmonics again. Then $X^{(T)}$ terms can then be extracted. From the measurement process, we know the X-parameters are defined under the large signal condition. And it reduces to S-parameter in the small signal limit, i.e. as A_{11} thinks.

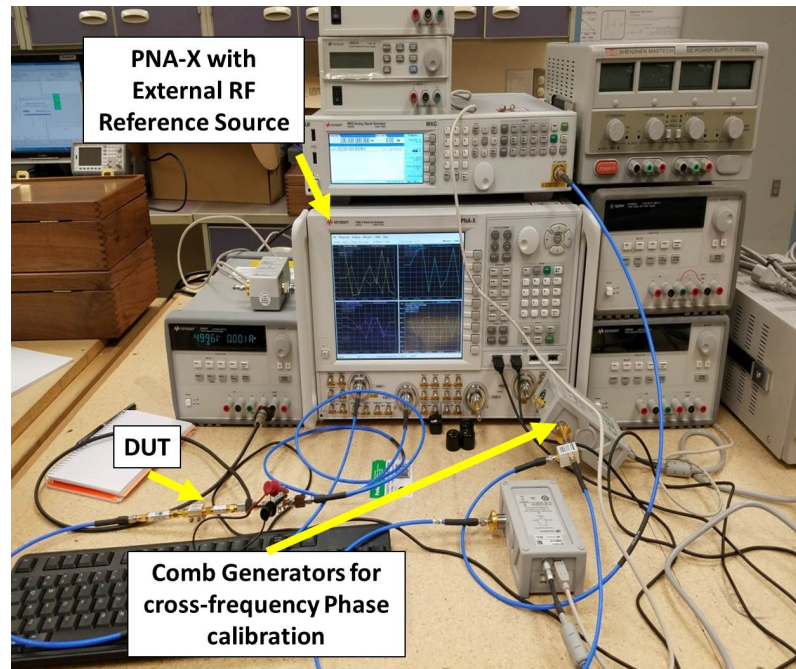


Figure B.10: Experimental setup at UNM for measuring the X-parameters of the 2nd harmonic circuit.

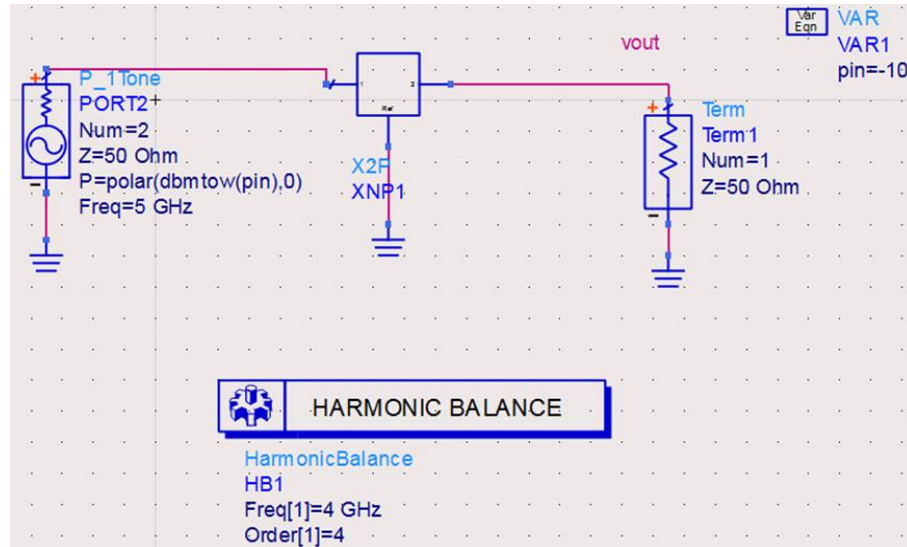


Figure B.11: Simulation circuit in ADS. The “XNP1” is the measured X-parameters file of the 2nd harmonics circuit.

We have collaborated with Prof. Sameer Hemmady at the University of New Mexico to measure X-parameters of the active 2nd harmonic generator as described in Chapter 2. Fig. B.10 shows the experimental setup to measure the circuit. The VNA has a second external RF reference source. The comb generators are used for cross-frequency phase calibration.

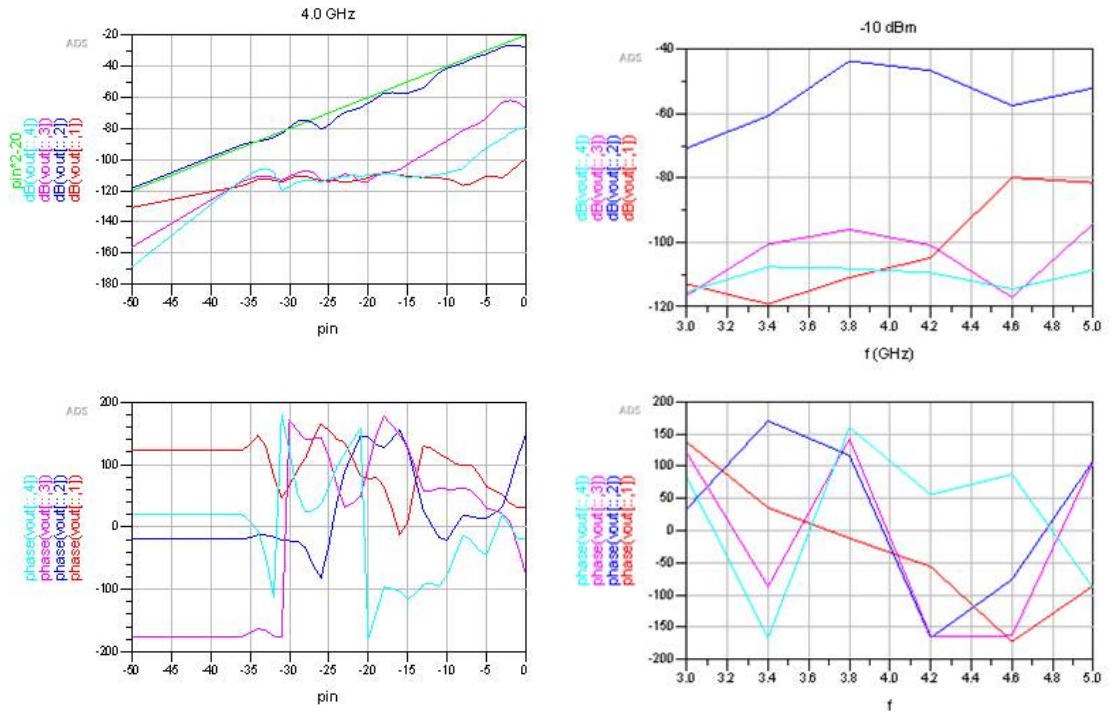


Figure B.12: ADS simulation with measured circuit X-parameters. (a) Power sweep at 4 GHz, spectral analysis from the 1st to the 4th order harmonics. Upper: Power magnitude of the harmonics, the green line is a straight line with slope of 2; Lower: Phases of the harmonics. (b) Frequency sweep for input power -10 dBm. Spectral analysis from the 1st to the 4th order harmonics. Upper: Power magnitude; Lower: Phases.

The measured X-parameters can be readily used for circuit design and simulation in the ADS program. As shown in Fig. B.11, X-parameter files work in Harmonic Balance and Envelope simulation. The figure shows a circuit sketch to analyze the measured file “XNP1”. Fig. B.12 are some simulation results of the harmonics. As we know from Chapter 2, the circuit generates 2nd harmonics in the frequency range of 3.5-4.5 GHz. The output power of the 2nd harmonic vs. the input power 1st order fundamental curve has a slope of 2 and saturates when the input power is close to 0 dBm. Fig. B.12(a) is the result of the harmonic response

up to the 4th order as a function of the input power at 4 GHz, both in magnitude and phase. It shows that the 2nd harmonics have the largest magnitude. And a green line with slope of 2 agrees quite well with the 2nd harmonic curve. Fig. B.12(b) shows the frequency dependence for input power -10 dBm in 3-5 GHz. It shows that 3.5-4.5 GHz is the range which has the largest 2nd order response. For the phase plot, we have not found any interesting results from it yet.

Appendix C: VNA High Power Option

C.1 Overview

The Agilent N5242A option H85 is a special configuration of the PNA-X network analyzers, configured for high-power measurements. The bias tees between the source attenuators and the test port couplers limit the maximum test port input power to +30 dBm. So to meet the requirements of high power measurements, option H85 has been created to supply extended power range attenuators without bias tees. Under this configuration, it is able to make high power network measurements at RF levels up to 20 Watts (+43 dBm) from 10 MHz to 26.5 GHz.

The option H85 does not increase the output power of the N5242A analyzer. It is designed to permit insertion of high power amplifiers and other signal conditioning equipment to make high power measurements. The users need to supply their own amplifiers and external components such as high power couplers, isolator and attenuators, etc. When configuring these components, the users need to consider the DUT requirements and protect the PNA from damage. This document is a summary of the configuration we have built, ref. [6] is a very helpful document including many details and guidelines.

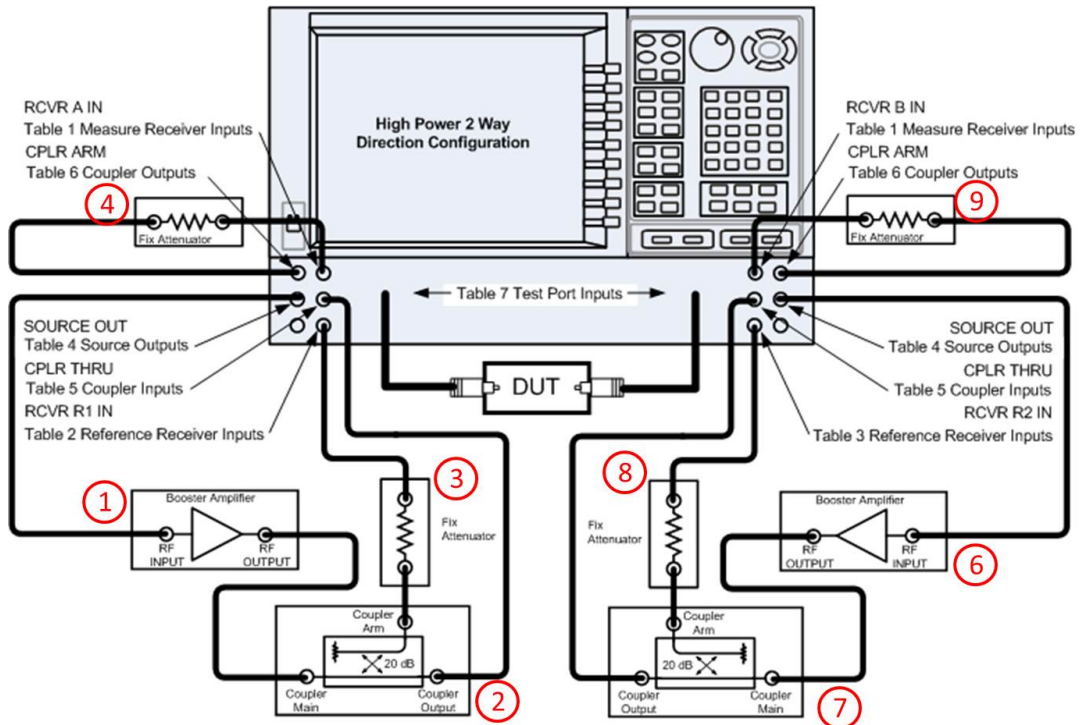
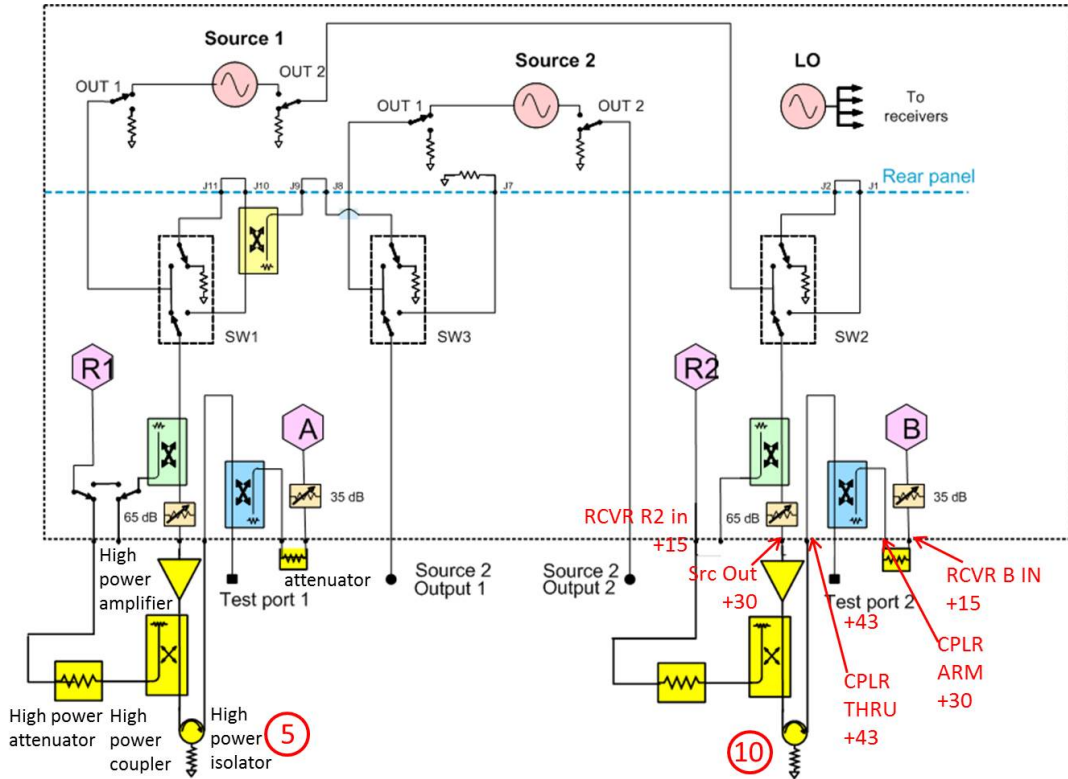


Figure C.1: 2-port two way high power configuration, Fig. 7 in ref. [6]. Damage power levels and external components are labelled.

C.2 Configuration

In our case, we want to make 2-port two-way high power calibrated S-parameter measurements, in the frequency range of at least 2-18 GHz. The configuration including the required components are shown in Fig. C.1, which is Fig. 7 in ref. [6]. When choosing these components, we also need to consider the damage levels of the PNA. The damage levels of the affected components of the PNA are given in Table 1-7 in ref. [6] and are summarized in Table. C.1. It is recommended that those components are operated at less than 3 dB and preferably 6 dB below the maximum power levels.

The components used are:

- RF-Lambda amplifier RFLUPA0218G5 (labelled No. 1, 6 in Fig. C.1) [122], 5W wide Band power amplifier 2-18 GHz
- AIRCOOLINGSYS1 (Integrated air cooling system with heatsink and fan for PN: RFLUPA0218G5, power at +24 VDC)
- RF-Lambda directional coupler RFDC2G18G20 (labelled No. 2, 7 in Fig. C.1) [123], 50W 20dB Directional Coupler 2-18 GHz
- Keithley 2231A-30-3 195W Triple Channel DC Power Supply [124], 30V/3A (2x) and 5V/3A. It is used to supply two channels of 24 V dc power to the two amplifiers.
- Mini-Circuits Attenuators (labelled No. 3, 4, 8, 9 in Fig. C.1)

- BW-S6-2W263+ [125], 50 Ω , 2 W, 6 dB, DC-26 GHz
- BW-S10-2W263+ [126], 50 Ω , 2 W, 10 dB, DC-26 GHz
- Fairview Microwave isolators (labelled No. 5, 10 in Fig. C.1)
 - SFI0418 [127] (Isolator SMA Female With 15 dB Isolation From 4 GHz to 18 GHz Rated to 10 Watts)
 - SFI0206S [128] (Isolator SMA Female With 13 dB Isolation From 2 GHz to 6 GHz Rated to 20 Watts)

The highest output power of the system is +35 dBm, and the frequency range is 2-18 GHz, both limited by the high power amplifier. Depending on the isolator used, measurements can either be done in the 4-18 GHz range or the 2-6 GHz range. Table C.1 shows the power levels at several components of the PNA, when operating at low power (-5 dBm), high power (+35 dBm) and maximum power (+43 dBm, which can't be achieved using current components). The high power attenuator and RCVR attenuator can be decreased to improve the accuracy for low power measurements, for example 6 dB for the high power attenuator and 12 dB for the RCVR attenuator.

Table C.1: Operating power levels of different components of the PNA, operating for 12 dB high power attenuator and 16 dB RCVR attenuator. Typical power levels are shown for 3.2-20 GHz. All in dBm units.

Component	typical	damage	op. low	op. high	op. max
RCVR A IN	-2~-2.5	15	-36	4	12
RCVR R1 IN	-2~-6	15	-37	3	11
Source Out	10~14	30	-40	0	8
CPLR THRU	-1.25~-2.2	43	-5	35	43
CPLR ARM	-2	30	-20	20	28
TEST PORT	-2	43	-5	35	43

C.3 Making High Power Measurements

The details and procedures to make high power measurements are described in [6]. A simplified version for making 2-port two-way high power measurement under our configuration is as follows:

- Connect the DC power supply to the high power amplifier and the integrated air cooling system. Both of them are powered at +24 VDC, so they can be connected to the same power supply. The current of amplifier is 1.9 A max. Setting the output current of the power supply to make sure there is enough current to the fan, normally 2A is enough. Turn the power supply off until the PNA is set-up.
- Connect the high power amplifier, directional coupler, isolators and attenua-

tors as shown in Fig. C.1 and C.2.

- Enable User Preset as directed in Fig. 14 of ref. [6]. We can create customized preset settings where the PNA will return when the preset button is pressed. Otherwise, the PNA will be back the factory default settings (including power levels, internal attenuator settings, etc.), where some components may get damaged under high power conditions.
- Set up a User Preset configuration. Set source output power level as -40 dBm (the lowest power we'll use), receiver attenuators 10 dB (this is a setting for the our highest power 0 dBm), change hardware setup so that the port 1 reference mixer is switched to be external, see procedures 15-18 in Page 26-28 [6]. Save this setting as the User Preset.
- Perform a mechanical calibration using the Maury Microwave 8050S 3.5mm Calibration Kit [129]. The reason to use mechanical calibration is that the Ecal can only calibrate up to 10 dBm. Press "Preset" to above User Preset settings, turn on the power for the high power amplifiers, and set the appropriate receiver attenuators. For example, if a 12 dB high power attenuator and 16 dB RCVR attenuator are used, the receiver attenuators can be set to 0 dB for source input powers up to -10 dBm, 5 dB for -5 dBm input and 10 dB for 0 dBm input. Go to "Cal" - > "start Cal", and choose "2 PortSolt", select "8050S boardband 3.5 mm" calibration Kit to start the mechanical calibration. Proceed to attach the corresponding calibration standards to finish and save the calibration. For different input power, the internal attenuator settings will

change accordingly, hence calibration at one power may not be applicable for other power settings. It is recommended to do the calibration at each power setting, respectively.

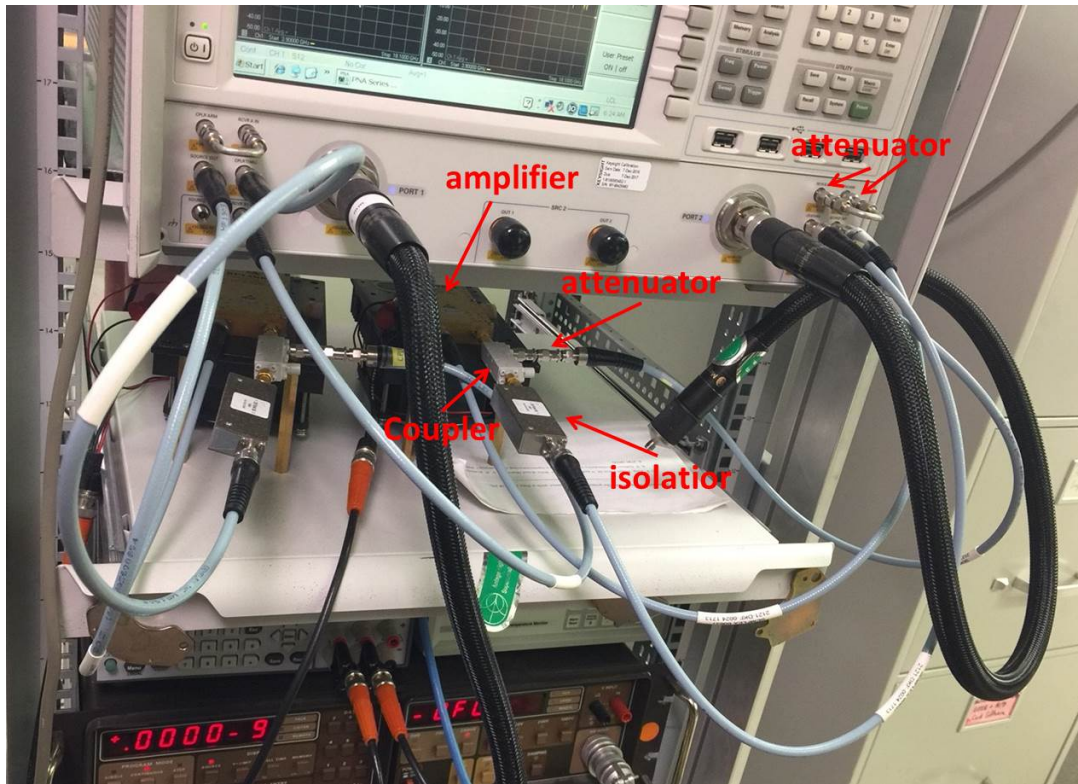


Figure C.2: Experimental setup of the high power 2-port two-way measurement

C.4 Noise Analysis

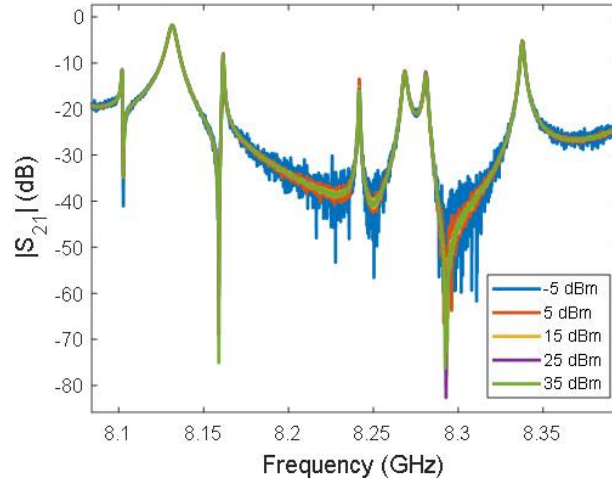


Figure C.3: Comparing $|S_{21}|$ for different output power levels, the signal-to-noise (SNR) for low power measurement is small. The DUT is a Pb-coated cut-circle microwave cavity in a dilution refrigerator at $T=740$ mK where there is around 20 dB around-trip attenuation along the transmission lines.

As given in the PNA N5242A datasheet, table 1 in ref. [130], the test port (A/B) noise floor is around -110 dBm. For the operating setting as shown in Table C.1, at low source input power -40 dBm, receiver A in is operating at -36 dBm max when the test ports are connected directly in a through configuration. This means that the dynamic range for the measurement has been decreased to $110-36=74$ dB. When the PNA is connect to the cryogenic system, there are long transmission lines going from the top to the bottom of the fridge where the device is located. For a typical 20 dB attenuation because of the transmission lines, it further decreases the dynamic range to around 50 dB. For the chaotic cavity we study, its S-parameters have a relatively wide dynamic range. We observe the S-parameters in the low power

settings are affected by the noise floor, see Fig. C.3. As the output power increases, the SNR of the measurement is improved. Hence, with the advantage that option H85 allows for high power measurements, it sacrifices the dynamic range or accuracy. In addition, by removing the bias tee, it can not make DC-bias measurements.

Bibliography

- [1] Edward Ott. *Chaos in Dynamical Systems*. Cambridge University Press, 2 edition, 2002.
- [2] Min Zhou, Edward Ott, Thomas M. Antonsen, and Steven M. Anlage. Non-linear wave chaos: statistics of second harmonic fields. *Chaos*, 27(10):103114, 2017.
- [3] Jen-Hao Yeh and Steven M. Anlage. In situ broadband cryogenic calibration for two-port superconducting microwave resonators. *Rev. Sci. Instrum.*, 84(3):034706, 2013.
- [4] M. Dressel and G. Gruner. *Electrodynamics of Solids: Optical Properties of Electrons in Matter*. Cambridge University Press, 2002.
- [5] *X-parameters in ADS*. Available at https://www.keysight.com/upload/cmc_upload/All/1_NVNA_and_X-parameters_in_ADS.pdf.
- [6] *Agilent Technologies N5242A Option H85 Users and Service Guide*, 2008. Available at <http://literature.cdn.keysight.com/litweb/pdf/N5242-90008.pdf>.
- [7] Y. Alhassid. The statistical theory of quantum dots. *Rev. Mod. Phys.*, 72(4):895–968, 2000.
- [8] P. W. Brouwer and C. W. J. Beenakker. Voltage-probe and imaginary-potential models for dephasing in a chaotic quantum dot. *Phys. Rev. B*, 55(7):4695–4702, 1997.
- [9] R. U. Haq, A. Pandey, and O. Bohigas. Fluctuation properties of nuclear energy levels: Do theory and experiment agree? *Phys. Rev. Lett.*, 48(16):1086–1089, 1982.
- [10] Roger G. Newton. *Scattering Theory of Waves and Particles*. McGraw-Hill, 1966.

- [11] E. Doron, U. Smilansky, and A. Frenkel. Experimental demonstration of chaotic scattering of microwaves. *Phys. Rev. Lett.*, 65(25):3072–3075, 1990.
- [12] Paul So, Steven M. Anlage, Edward Ott, and Robert N. Oerter. Wave chaos experiments with and without time reversal symmetry: GUE and GOE statistics. *Phys. Rev. Lett.*, 74(14):2662–2665, 1995.
- [13] U. Kuhl, M. Martínez-Mares, R. A. Méndez-Sánchez, and H.-J. Stöckmann. Direct processes in chaotic microwave cavities in the presence of absorption. *Phys. Rev. Lett.*, 94(14):144101, 2005.
- [14] R. L. Weaver. Spectral statistics in elastodynamics. *The Journal of the Acoustical Society of America*, 85(3):1005–1013, 1989.
- [15] C. Ellegaard, T. Guhr, K. Lindemann, H. Q. Lorensen, J. Nygård, and M. Oxborrow. Spectral statistics of acoustic resonances in aluminum blocks. *Phys. Rev. Lett.*, 75(8):1546–1549, 1995.
- [16] Biniyam Tesfaye Taddese, Gabriele Gradoni, Franco Moglie, Thomas M. Antonsen, Edward Ott, and Steven M. Anlage. Quantifying volume changing perturbations in a wave chaotic system. *New J. Phys.*, 15(2):023025, 2013.
- [17] G. Casati, F. Valz-Gris, and I. Guarneri. On the connection between quantization of nonintegrable systems and statistical theory of spectra. *Lett. Nuovo Cimento*, 28(8):279–282, 1980.
- [18] O. Bohigas, M. J. Giannoni, and C. Schmit. Characterization of chaotic quantum spectra and universality of level fluctuation laws. *Phys. Rev. Lett.*, 52(1):1–4, 1984.
- [19] H. J. Stöckmann. *Quantum Chaos: An Introduction*. (Cambridge) University Press, Cambridge, 1999.
- [20] Sameer Hemmady, Xing Zheng, Thomas M. Antonsen, Edward Ott, and Steven M. Anlage. Universal statistics of the scattering coefficient of chaotic microwave cavities. *Phys. Rev. E*, 71(5):056215, 2005.
- [21] Jinho Baik Gernot Akemann and Philippe Di Francesco. *The Oxford Handbook of Random Matrix Theory*. Oxford University Press, 2010.
- [22] Y. V. Fyodorov, D. V. Savin, and H.-J. Sommers. Scattering, reflection and impedance of waves in chaotic and disordered systems with absorption. *J. Phys. A: Math. Gen.*, 38(49):10731, 2005.
- [23] B. Dietz and A. Richter. Quantum and wave dynamical chaos in superconducting microwave billiards. *Chaos*, 25(9):097601, 2015.

- [24] Dong Ho Wu, Jesse S. A. Bridgewater, Ali Gokirmak, and Steven M. Anlage. Probability amplitude fluctuations in experimental wave chaotic eigenmodes with and without time-reversal symmetry. *Phys. Rev. Lett.*, 81(14):2890–2893, 1998.
- [25] Seok-Hwan Chung, Ali Gokirmak, Dong-Ho Wu, J. S. A. Bridgewater, E. Ott, T. M. Antonsen, and Steven M. Anlage. Measurement of wave chaotic eigenfunctions in the time-reversal symmetry-breaking crossover regime. *Phys. Rev. Lett.*, 85(12):2482–2485, 2000.
- [26] Xing Zheng, Sameer Hemmady, Thomas M. Antonsen, Steven M. Anlage, and Edward Ott. Characterization of fluctuations of impedance and scattering matrices in wave chaotic scattering. *Phys. Rev. E*, 73(4):046208, 2006.
- [27] J. A. Hart, T. M. Antonsen, and E. Ott. Effect of short ray trajectories on the scattering statistics of wave chaotic systems. *Phys. Rev. E*, 80(4):041109, 2009.
- [28] Jen-Hao Yeh, James A. Hart, Elliott Bradshaw, Thomas M. Antonsen, Edward Ott, and Steven M. Anlage. Universal and nonuniversal properties of wave-chaotic scattering systems. *Phys. Rev. E*, 81(2):025201, 2010.
- [29] Jen-Hao Yeh, James A. Hart, Elliott Bradshaw, Thomas M. Antonsen, Edward Ott, and Steven M. Anlage. Experimental examination of the effect of short ray trajectories in two-port wave-chaotic scattering systems. *Phys. Rev. E*, 82(4):041114, 2010.
- [30] F. Beck, C. Dembowski, A. Heine, and A. Richter. *R*-matrix theory of driven electromagnetic cavities. *Phys. Rev. E*, 67(6):066208, 2003.
- [31] Oleh Hul, Szymon Bauch, Prot Pakoski, Nazar Savytsky, Karol yczkowski, and Leszek Sirko. Experimental simulation of quantum graphs by microwave networks. *Phys. Rev. E*, 69(5):056205, 2004.
- [32] Sameer Hemmady, Xing Zheng, Edward Ott, Thomas M. Antonsen, and Steven M. Anlage. Universal impedance fluctuations in wave chaotic systems. *Phys. Rev. Lett.*, 94(1):014102, 2005.
- [33] Z. B. Drikas, J. Gil Gil, S. K. Hong, T. D. Andreadis, J. Yeh, B. T. Taddese, and S. M. Anlage. Application of the random coupling model to electromagnetic statistics in complex enclosures. *IEEE Trans. Electromagn. Compat.*, 56(6):1480–1487, 2014.
- [34] S. Hemmady, X. Zheng, T.M Antonsen, E. Ott, and S.M Anlage. Aspects of the Scattering and Impedance Properties of Chaotic Microwave Cavities. *Acta Physica Polonica A*, 109(1):65–71, January 2006.

- [35] Sameer Hemmady, James Hart, Xing Zheng, Thomas M. Antonsen, Edward Ott, and Steven M. Anlage. Experimental test of universal conductance fluctuations by means of wave-chaotic microwave cavities. *Phys. Rev. B*, 74(19):195326, 2006.
- [36] Bo Xiao, Thomas M. Antonsen, Edward Ott, and Steven M. Anlage. Focusing waves at arbitrary locations in a ray-chaotic enclosure using time-reversed synthetic sonas. *Physical Review E*, 93(5):052205, May 2016.
- [37] Sameer Hemmady, Xing Zheng, James Hart, Thomas M. Antonsen, Edward Ott, and Steven M. Anlage. Universal properties of two-port scattering, impedance, and admittance matrices of wave-chaotic systems. *Phys. Rev. E*, 74(3):036213, 2006.
- [38] S. Hemmady, T. M. Antonsen, E. Ott, and S. M. Anlage. Statistical prediction and measurement of induced voltages on components within complicated enclosures: A wave-chaotic approach. *IEEE Trans. Electromagn. Compat*, 54(4):758–771, 2012.
- [39] C. Kasmi, O. Maurice, G. Gradoni, T. Antonsen, E. Ott, and S. Anlage. Stochastic Kron’s model inspired from the Random Coupling Model. In *2015 IEEE International Symposium on Electromagnetic Compatibility (EMC)*, pages 935–940, August 2015.
- [40] Gabriele Gradoni, Xiaoming Chen, Thomas M. Antonsen, Steven M. Anlage, and Edward Ott. Random coupling model for wireless communication channels. In *2014 International Symposium on Electromagnetic Compatibility*, pages 878–882, Gothenburg, September 2014. IEEE.
- [41] J.H. Yeh, E. Ott, T.M. Antonsen, and S.M. Anlage. Fading Statistics in Communications - a Random Matrix Approach. *Acta Physica Polonica A*, 120(6A):A–85–A–88, December 2011.
- [42] Jen-Hao Yeh, Thomas M. Antonsen, Edward Ott, and Steven M. Anlage. First-principles model of time-dependent variations in transmission through a fluctuating scattering environment. *Phys. Rev. E*, 85(1):015202, 2012.
- [43] Dmitry V. Savin, Martin Richter, Ulrich Kuhl, Olivier Legrand, and Fabrice Mortessagne. Fluctuations in an established transmission in the presence of a complex environment. *Physical Review E*, 96(3):032221, September 2017.
- [44] G. Gradoni, J. Yeh, T. M. Antonsen, S. Anlage, and E. Ott. Wave chaotic analysis of weakly coupled reverberation chambers. In *2011 IEEE International Symposium on Electromagnetic Compatibility*, pages 202–207, 2011.
- [45] Yves Aurégan and Vincent Pagneux. Acoustic scattering in duct with a chaotic cavity. *Acta Acustica united with Acustica*, 102(5):869–875, 2016.

- [46] Ming-Jer Lee, Thomas M. Antonsen, and Edward Ott. Statistical model of short wavelength transport through cavities with coexisting chaotic and regular ray trajectories. *Phys. Rev. E*, 87(6):062906, 2013.
- [47] Gabriele Gradoni, Thomas M. Antonsen, and Edward Ott. Impedance and power fluctuations in linear chains of coupled wave chaotic cavities. *Phys. Rev. E*, 86(4):046204, 2012.
- [48] B. D. Addissie, J. C. Rodgers, and T. M. Antonsen. Application of the random coupling model to lossy ports in complex enclosures. In *2015 IEEE Metrology for Aerospace (MetroAeroSpace)*, pages 214–219, 2015.
- [49] Bisrat Addissie, John Rodgers, and Thomas Antonsen. Extraction of the coupling impedance in overmoded cavities. *Wave Motion*, 2018. DOI:10.1016/j.wavemoti.2018.09.011.
- [50] Bo Xiao, Thomas M. Antonsen, Edward Ott, Zachary B. Drikas, Jesus Gil Gil, and Steven M. Anlage. Revealing underlying universal wave fluctuations in a scaled ray-chaotic cavity with remote injection. *Phys. Rev. E*, 97(6):062220, 2018.
- [51] E. J. Heller, L. Kaplan, and A. Dahlen. Refraction of a gaussian seaway. *Journal of Geophysical Research: Oceans*, 113, 2008.
- [52] R. Höhmann, U. Kuhl, H.-J. Stöckmann, L. Kaplan, and E. J. Heller. Freak waves in the linear regime: A microwave study. *Phys. Rev. Lett.*, 104(9):093901, 2010.
- [53] Kristian Dysthe, Harald E. Krogstad, and Peter Müller. Oceanic rogue waves. *Annu. Rev. Fluid Mech.*, 40(1):287–310, 2008.
- [54] M. Onorato, S. Residori, U. Bortolozzo, A. Montina, and F. T. Arecchi. Rogue waves and their generating mechanisms in different physical contexts. *Physics Reports*, 528(2):47–89, 2013.
- [55] Bart Van Damme, Koen Van Den Abeele, YiFeng Li, and Olivier Bou Matar. Time reversed acoustics techniques for elastic imaging in reverberant and non-reverberant media: An experimental study of the chaotic cavity transducer concept. *Journal of Applied Physics*, 109(10):104910, 2011.
- [56] Robert A. Guyer and Paul A. Johnson. Nonlinear mesoscopic elasticity: Evidence for a new class of materials. *Physics Today*, 52(4):30, 2008.
- [57] Koen E-A. Van Den Abeele, Alexander Sutin, Jan Carmeliet, and Paul A. Johnson. Micro-damage diagnostics using nonlinear elastic wave spectroscopy (NEWS). *NDT & E International*, 34(4):239–248, 2001.

- [58] Geoffroy Lerosey, Julien de Rosny, Arnaud Tourin, and Mathias Fink. Focusing beyond the diffraction limit with far-field time reversal. *Science*, 315(5815):1120–1122, 2007.
- [59] Matthew Frazier, Biniyam Taddese, Thomas Antonsen, and Steven M. Anlage. Nonlinear time reversal in a wave chaotic system. *Phys. Rev. Lett.*, 110(6):063902, 2013.
- [60] Matthew Frazier, Biniyam Taddese, Bo Xiao, Thomas Antonsen, Edward Ott, and Steven M. Anlage. Nonlinear time reversal of classical waves: Experiment and model. *Phys. Rev. E*, 88(6):062910, 2013.
- [61] Frank Cangialosi, Tyler Grover, Patrick Healey, Tim Furman, Andrew Simon, and Steven M. Anlage. Time reversed electromagnetic wave propagation as a novel method of wireless power transfer. In *2016 IEEE Wireless Power Transfer Conference (WPTC)*, pages 1–4. IEEE, 2016.
- [62] Scott Roman, Rahul Gogna, and Steven M. Anlage. Selective collapse of nonlinear time reversed electromagnetic waves. In *2016 IEEE Wireless Power Transfer Conference (WPTC)*, pages 1–4. IEEE, 2016.
- [63] Sven Gnutzmann, Uzy Smilansky, and Stanislav Derevyanko. Stationary scattering from a nonlinear network. *Phys. Rev. A*, 83(3):033831, 2011.
- [64] Seth D. Cohen, Hugo L. D. de S. Cavalcante, and Daniel J. Gauthier. Sub-wavelength position sensing using nonlinear feedback and wave chaos. *Phys. Rev. Lett.*, 107(25):254103, 2011.
- [65] Yann LeCun, Yoshua Bengio, and Geoffrey Hinton. Deep learning. *Nature*, 521(7553):436–444, 2015.
- [66] Guy Satat, Matthew Tancik, Otkrist Gupta, Barmak Heshmat, and Ramesh Raskar. Object classification through scattering media with deep learning on time resolved measurement. *Opt. Express, OE*, 25(15):17466–17479, 2017.
- [67] Jaideep Pathak, Zhixin Lu, Brian R. Hunt, Michelle Girvan, and Edward Ott. Using machine learning to replicate chaotic attractors and calculate Lyapunov exponents from data. *Chaos*, 27(12):121102, 2017.
- [68] Jaideep Pathak, Brian Hunt, Michelle Girvan, Zhixin Lu, and Edward Ott. Model-free prediction of large spatiotemporally chaotic systems from data: A reservoir computing approach. *Phys. Rev. Lett.*, 120(2):024102, 2018.
- [69] Yichen Shen, Nicholas C. Harris, Scott Skirlo, Mihika Prabhu, Tom Baehr-Jones, Michael Hochberg, Xin Sun, Shijie Zhao, Hugo Larochelle, Dirk Englund, and Marin Soljačić. Deep learning with coherent nanophotonic circuits. *Nature Photonics*, 11:441, 2017.

- [70] Stefan Rotter and Sylvain Gigan. Light fields in complex media: Mesoscopic scattering meets wave control. *Rev. Mod. Phys.*, 89(1):015005, 3017.
- [71] Philipp del Hougne, Mathias Fink, and Geoffroy Lerosey. Shaping microwave fields using nonlinear unsolicited feedback: Application to enhance energy harvesting. *Phys. Rev. Applied*, 8(6):061001, 2017.
- [72] Xing Zheng, Thomas M. Antonsen, and Edward Ott. Statistics of impedance and scattering matrices in chaotic microwave cavities: Single channel case. *Electromagnetics*, 26(1):3–35, 2006.
- [73] Xing Zheng, Thomas M. Antonsen, and Edward Ott. Statistics of impedance and scattering matrices of chaotic microwave cavities with multiple ports. *Electromagnetics*, 26(1):37–55, 2006.
- [74] J.-H. Yeh, Z. Drikas, J. Gil Gil, S. Hong, B.T. Taddese, E. Ott, T.M. Antonsen, T. Andreadis, and S.M. Anlage. Impedance and scattering variance ratios of complicated wave scattering systems in the low loss regime. *Acta Physica Polonica A*, 124(6):1045–1052, 2013.
- [75] Min Zhou, Edward Ott, Thomas M. Antonsen, and Steven M. Anlage. Scattering statistics in nonlinear wave chaotic systems. *Chaos*, 29(3):033113, 2019.
- [76] Jonas Zmuidzinas. Superconducting Microresonators: Physics and Applications. *Annual Review of Condensed Matter Physics*, 3(1):169–214, February 2012.
- [77] Hua Xu, Steven M. Anlage, Liangbing Hu, and George Gruner. Microwave shielding of transparent and conducting single-walled carbon nanotube films. *Appl. Phys. Lett.*, 90(18):183119, 2007.
- [78] Hua Xu, Shixong Zhang, Steven M. Anlage, Liangbing Hu, and George Gruner. Frequency- and electric-field-dependent conductivity of single-walled carbon nanotube networks of varying density. *Phys. Rev. B*, 77(7):075418, 2006.
- [79] Gabriele Gradoni, Jen-Hao Yeh, Bo Xiao, Thomas M. Antonsen, Steven M. Anlage, and Edward Ott. Predicting the statistics of wave transport through chaotic cavities by the random coupling model: A review and recent progress. *Wave Motion*, 51(4):606–621, 2014.
- [80] Mario Lefebvre. *Applied Probability and Statistics*. Springer-Verlag, New York, 2006.
- [81] I. Flintoft, A. Marvin, and L. Dawson. Statistical response of nonlinear equipment in a reverberation chamber. In *2008 IEEE International Symposium on Electromagnetic Compatibility*, pages 1–6, 2008.

- [82] C. Jiaqi, A. Marvin, I. Flintoft, and J. Dawson. Double-weibull distributions of the re-emission spectra from a non-linear device in a mode stirred chamber. In *2010 IEEE International Symposium on Electromagnetic Compatibility*, pages 541–546, 2010.
- [83] A. C. Marvin, C. Jiaqi, I. D. Flintoft, and J. F. Dawson. A describing function method for evaluating the statistics of the harmonics scattered from a non-linear device in a mode stirred chamber. In *2009 IEEE International Symposium on Electromagnetic Compatibility*, pages 165–170, 2009.
- [84] Laurent Guibert, Patrick Millot, Xavier Ferrières, and Étienne Sicard. An original method for the measurement of the radiated susceptibility of an electronic system using induced electromagnetic nonlinear effects. *Progress In Electromagnetics Research*, 62:83–89, 2016.
- [85] Y. V. Fyodorov and D. V. Savin. Statistics of impedance, local density of states, and reflection in quantum chaotic systems with absorption. *Jetp Lett.*, 80(12):725–729, 2004.
- [86] Ali Gokirmak, Dong-Ho Wu, J. S. A. Bridgewater, and Steven M. Anlage. Scanned perturbation technique for imaging electromagnetic standing wave patterns of microwave cavities. *Rev. Sci. Instrum.*, 69(9):3410–3417, 1998.
- [87] *infineonBAS7004datasheet*. Available at <https://www.infineon.com/cms/en/product/transistor-diode/diode/schottky-diode/high-speed-switching-clipping-and-clamping/bas70-04/>.
- [88] Renato Mariz de Moraes and Steven M. Anlage. Unified model and reverse recovery nonlinearities of the driven diode resonator. *Phys. Rev. E*, 68:026201, Aug 2003.
- [89] R. M. de Moraes and S. M. Anlage. Effects of UHF stimulus and negative feedback on nonlinear circuits. *IEEE Transactions on Circuits and Systems I: Regular Papers*, 51(4):748–754, April 2004.
- [90] Z. Wu and R. W. Ziolkowski. Electromagnetic effects associated with a cavity-backed aperture loaded with nonlinear elements. *Progress In Electromagnetics Research*, 28:1–16, 2000.
- [91] R. V. Garver. *Microwave diode control devices*. Artech House, Inc., Dedham, Mass., 1976.
- [92] Stefano Lepri and Giulio Casati. Asymmetric wave propagation in nonlinear systems. *Phys. Rev. Lett.*, 106(16):164101, 2011.
- [93] Dragos Dancila, Aleksander Eriksson, Vitaliy Goryashko, Linus Haapala, Roger Ruber, Anders Rydberg, Rolf Wedberg, Rutambhara Yogi, and Volker Ziemann. Solid-state amplifier development at FREIA. In *Proceedings of*

- the 5th Int. Particle Accelerator Conf.*, volume IPAC2014, page WEPME012, 2014.
- [94] Patrick Roblin. *Nonlinear RF Circuits and Nonlinear Vector Network Analyzers*. Cambridge University Press, 2011.
- [95] David E. Root, Jan Verspecht, Jason Horn, and Mihai Marcu. *X-Parameters*. Cambridge University Press, 2013.
- [96] Suhan Ree and L. E. Reichl. Classical and quantum chaos in a circular billiard with a straight cut. *Physical Review E*, 60(2):1607–1615, August 1999.
- [97] Claire Michel, Valérie Doya, Sorin Tascu, Wilfried Blanc, Olivier Legrand, and Fabrice Mortessagne. Controlled excitation of scar modes in passive and active multimode chaotic fiber. *Appl. Opt.*, 48(31):G163–G168, Nov 2009.
- [98] Vladimir V. Talanov, Lucia V. Mercaldo, Steven M. Anlage, and John H. Claassen. Measurement of the absolute penetration depth and surface resistance of superconductors and normal metals with the variable spacing parallel plate resonator. *Review of Scientific Instruments*, 71(5):2136–2146, 2000.
- [99] K. E. Petersen. Silicon as a mechanical material. *Proceedings of the IEEE*, 70(5):420–457, May 1982.
- [100] J. Krupka, J. Breeze, A. Centeno, N. Alford, T. Claussen, and L. Jensen. Measurements of Permittivity, Dielectric Loss Tangent, and Resistivity of Float-Zone Silicon at Microwave Frequencies. *IEEE Transactions on Microwave Theory and Techniques*, 54(11):3995–4001, November 2006.
- [101] O. M. Corbino. Azioni elettromagnetiche dovute agli ioni dei metalli deviati dalla traiettoria normale per effetto di un campo. *Il Nuovo Cimento*, 1:397–420, 1911.
- [102] Rudolf Hübener. *Magnetic Flux Structures in Superconductors: Extended Reprint of a Classic Text*. Springer Series in Solid-State Sciences. Springer-Verlag, 2 edition, 2001.
- [103] J. C. Booth, Dong Ho Wu, and Steven M. Anlage. A broadband method for the measurement of the surface impedance of thin films at microwave frequencies. *Review of Scientific Instruments*, 65(6):2082–2090, 1994.
- [104] James Clay Booth. *NOVEL MEASUREMENTS OF THE FREQUENCY DEPENDENT MICROWAVE SURFACE IMPEDANCE OF CUPRATE THIN FILM SUPERCONDUCTORS*. PhD thesis, University of Maryland, College Park, 8 1996.
- [105] E. Silva, N. Pompeo, K. Torokhtii, and S. Sarti. Wideband surface impedance measurements in superconducting films. *IEEE Transactions on Instrumentation and Measurement*, 65(5):1120–1129, 2016.

- [106] James C. Booth, Dong-Ho Wu, and Steven M. Anlage. *Measurements of the Frequency Dependent Microwave Fluctuation Conductivity of Cuprate Thin Film Superconductors*. NATO ASI Series. Springer Netherlands, 1997.
- [107] James C. Booth, Dong-Ho Wu, and Steven M. Anlage. Temperature dependence of the microwave conductivity near T_c in $\text{YBa}_2\text{Cu}_3\text{O}_{7-\delta}$ -thin films. *Czech Journal of Physics*, 46-S3:1399, 1996.
- [108] James C. Booth, Dong Ho Wu, S. B. Qadri, E. F. Skelton, M. S. Osofsky, Alberto Pique, and Steven M. Anlage. Large dynamical fluctuations in the microwave conductivity of $\text{YBa}_2\text{Cu}_3\text{O}_{7-\delta}$ above T_c . *Phys. Rev. Lett.*, 77(21):4438–4441, 1996.
- [109] Dong Ho Wu, J. C. Booth, and Steven M. Anlage. Frequency and field variation of vortex dynamics in $\text{YBa}_2\text{Cu}_3\text{O}_{7-\delta}$. *Phys. Rev. Lett.*, 75(3):525–528, 1995.
- [110] E. Silva, M. Lanucara, and R. Marcon. The effective surface resistance of superconductor/dielectric/metal structures. *Supercond. Sci. Technol.*, 9(11):934–941.
- [111] Faisal Shahzad, Mohamed Alhabeab, Christine B. Hatter, Babak Anasori, Soon Man Hong, Chong Min Koo, and Yury Gogotsi. Electromagnetic interference shielding with 2d transition metal carbides (MXenes). *Science*, 353(6304):1137–1140, 2016.
- [112] M. A. Stuchly and S. S. Stuchly. Coaxial line reflection methods for measuring dielectric properties of biological substances at radio and microwave frequencies—a review. *IEEE Transactions on Instrumentation and Measurement*, 29(3):176–183, 1980.
- [113] R. Bhmer, M. Maglione, P. Lunkenheimer, and A. Loidl. Radiofrequency dielectric measurements at temperatures from 10 to 450 k. *Journal of Applied Physics*, 65(3):901–904, 1989.
- [114] P. De Langhe, K. Blomme, L. Martens, and D. De Zutter. Measurement of low-permittivity materials based on a spectral-domain analysis for the open-ended coaxial probe. *IEEE Transactions on Instrumentation and Measurement*, 42(5):879–886, 1993.
- [115] D. Vincent, L. Jorat, J. Monin, and G. Noyel. Improvement of the transmission/reflection method for dielectric and magnetic measurements on liquids between 0.1 and 20 GHz. *Measurement Science and Technology*, 5(8):990–995, 1994.
- [116] A. J. Becker, P. Polakos, H. Huggins, J. Pastalan, K. Watts, Y. H. Wong, and P. Mankiewich. RF measurement technique for characterizing thin dielectric films. *IEEE Transactions on Electron Devices*, 45(8):1811–1816, 1998.

- [117] H. C. F. Martens, J. A. Reedijk, and H. B. Brom. Measurement of the complex dielectric constant down to helium temperatures. i. reflection method from 1 MHz to 20 GHz using an open ended coaxial line. *Review of Scientific Instruments*, 71(2):473–477, 2000.
- [118] Mingzhong Wu, Xi Yao, and Liangying Zhang. An improved coaxial probe technique for measuring microwave permittivity of thin dielectric materials. *Measurement Science and Technology*, 11(11):1617–1622, 2000.
- [119] Bisrat Demeke Addissie. *METHODS FOR CHARACTERIZING ELECTROMAGNETIC COUPLING STATISTICS IN COMPLEX ENCLOSURES*. PhD thesis, University of Maryland, College Park, 2017. Available at <https://doi.org/10.13016/M2XD0R03Q>.
- [120] J. Gil Gil, Z. B. Drikas, T. D. Andreadis, and S. M. Anlage. Prediction of induced voltages on ports in complex, three-dimensional enclosures with apertures, using the random coupling model. *IEEE Trans. Electromagn. Compat.*, 58(5):1535–1540, 2016.
- [121] Paul Tze-Man So. *Observing and Controlling Chaotic Systems and Wave Chaos Statistics*. PhD thesis, University of Maryland, College Park, 8 2005.
- [122] *RF Lambda power amplifier RFLUPA0218G5 datasheet*, 2018. Available at <http://www.rflambda.com/pdf/poweramplifier/RFLUPA0218G5.pdf>.
- [123] *RF Lambda directional coupler RFDC2G18G20 datasheet*. Available at <http://www.rflambda.com/pdf/directionalcoupler/RFDC2G18G20.pdf>.
- [124] *Keithley 2220/2230/2231 Multiple Output DC Power Supply Datasheet and User’s Manual*, 2013. Available at <https://www.tek.com/tektronix-and-keithley-dc-power-supplies/keithley-2220-2230-2231-series>.
- [125] *Mini-Circuits BW-S6-2W263+ datasheet*, 2018. Available at <https://www.minicircuits.com/WebStore/dashboard.html?model=BW-S6-2W263%2B>.
- [126] *Mini-Circuits BW-S10-2W263+ datasheet*, 2018. Available at <https://www.minicircuits.com/WebStore/dashboard.html?model=BW-S10-2W263%2B>.
- [127] *Fairview Microwave isolator SFI0418 datasheet*, 2016. Available at <https://www.fairviewmicrowave.com/sma-isolator-15-db-isolation-4-18-ghz-10-watts-sfi0418-p.aspx>.
- [128] *Fairview Microwave isolator SFI0206S datasheet*, 2015. Available at <https://www.fairviewmicrowave.com/>

[sma-isolator-14-db-isolation-2-6-ghz-25-watts-sfi0206s-p.aspx](#).

- [129] *Maury Microwave 8050S 3.5mm Calibration Kits information. Available at https://www.maurymw.com/Precision/3.5mm_Cal_Kits.php.*
- [130] *Keysight Technologies N5242A PNA-X Microwave Network Analyzer, 26.5 GHz. Available at <https://www.keysight.com/en/pdx-x202277-pn-N5242A/pna-x-microwave-network-analyzer-265-ghz?nid=-32497.1150434.00&cc=US&lc=eng>.*